universität wien

DISSERTATION / DOCTORAL THESIS

Titel der Dissertation /Title of the Doctoral Thesis

„Cooling and manipulating the ro-translational motion of dielectric particles in high vacuum“

verfasst von / submitted by

Stefan Kuhn, BSc MSc

angestrebter akademischer Grad / in partial fulfilment of the requirements for the degree of

Doktor der Naturwissenschaften (Dr. rer. nat.)

Wien, 2017 / Vienna, 2017

Studienkennzahl lt. Studienblatt / degree programme code as it appears on the student record sheet:	A 796 605 411
Dissertationsgebiet lt. Studienblatt / field of study as it appears on the student record sheet:	Physik
Betreut von / Supervisor:	Univ. Prof. Dr. Markus Arndt

Contents

Abstract

Future matter-wave interferometers, which are targeted at probing the quantum superposition principle with objects of increasing mass and complexity, will require coherent sources of slow and cold particles. In this work I study the possibilities for realizing these experiments with dielectric nanoparticles, by controlling, manipulating, and cooling them in optical dipole potentials and high-finesse optical cavities.

I investigate the requirements for matter-wave interferometry and propose a scheme to resolve interference effects with silicon nanoparticles of up to 10^7 atomic mass units. With this application in mind, I present laser-based launch methods for particles of various sizes and shapes in ultra-high vacuum and the detection and manipulation of nanoparticles in intense cavity fields. Based on this experimental progress, I discuss the prospects of cooling dielectric nanoparticles to realise a coherent source for matter-wave interferometry in dedicated microcavities, whose low mode-volume will enhance the light-matter interaction. I present the implementation of silicon micromirror chips to form open-access cavities with beam waist radii of 12 μm and cavity mode-volumes of 15 pL, allowing for high signal-to-noise detection of 150 nm radius nanoparticles via their strong coupling to the field of a single cavity. In the future, microcavities with better controlled mirror shapes and higher finesse will be capable of cooling particles with masses down to a few 10^6 amu.

The laser-induced launch method also enables novel studies with non-spherical nanoparticles. The free rotation of silicon nanorods can be detected via their scattering in intense optical fields, resolving rotation rates of up to 50 MHz. At millibar gas pressures these particles can be stably levitated for more than 100 days in the standing light wave formed by two focussed counter-propagating laser beams. The nanorods exhibit an orientation dependent polarizability which can be exploited in order to control their rotational motion. When the polarisation of the trapping beams is periodically modulated between linear and circular, the particles can be driven and their rotation locks to an external clock with surprisingly high stability. This experiment paves the way for very precise, local sensing applications and single-particle thermodynamics studies. To enable new quantum experiments in the orientational degrees of freedom and facilitate orientation dependent high-mass matter-wave interferometry, I discuss the prospects of employing a cavity to cool both the rotational and translational motion of non-spherical nanoparticles. Under realistic experimental conditions, cooling to the ro-translational quantum ground-state of a rod or disk is within reach.

Zusammenfassung

Zukünftige Materiewelleninterferometer sollen das Quantensuperpositionsprinzip für Objekte mit mehr als 10^6 atomaren Masseneinheiten testen. Um kohärente Quellen dafür zu entwickeln sind neue Techniken notwendig. In dieser Arbeit untersuche ich Methoden um solche Experimente mit dielektrischen Nanoteilchen zu realisieren, in dem man die Teilchen in optischen Dipol-Potentialen und Resonatorfeldern manipuliert, kontrolliert und kühlt.

Ich schätze die experimentellen Voraussetzungen für zukünftige Interferometrieexperimente im Massenbereich von 10^6-10^7 atomaren Masseneinheiten ab und präsentiere ein Schema um die Interferenz von Teilchen mit 10^7 atomaren Masseineinheiten aufzulösen. Für diese Anwendung stelle ich Methoden vor, die es uns ermöglichen Nanoteilchen verschiedener Größe und Form unter Hochvakuumbedingungen in die Gas-Phase zu bekommen und in intensiven Lichtfeldern optischer Resonatoren zu detektieren und zu manipulieren. Basierend auf dem experimentellen Fortschritt diskutiere ich die Aussichten um Nanoteilchen in optischen Resonatoren mit hoher Güte zu kühlen, um eine kohärente Quelle für Materiewellenexperimente zu realisieren. Dies beinhaltet das Kühlen der Massenmittelpunktsbewegung von Teilchen mit $10^6 - 10^7$ atomaren Masseneinheiten in speziell angefertigten Mikroresonatoren, deren kleines Modenvolumen die Wechselwirkung mit den Teilchen verstärkt. Ich präsentiere den Einsatz von Mikrospiegel auf Silizium-Chips um Resonatoren mit Strahldurchmessern von 24 μm bzw. Modenvolumen von 15 pL zu formen, die es uns erlauben Glas-Nanoteilchen mit 150 nm Radius durch ihre starke Kopplung an das Resonatorfeld mit hohem Signal zu Rausch Verhältnis zu detektieren.

Unsere Nanoteilchenquelle erlaubt es uns auch, erstmals die Rotationsbewegung von elongierten Nanoteilchen zu untersuchen. Wir können die freie Rotation von Siliziumstäbchen durch Streuung von starken Lichtfeldern detektieren und Rotationsraten von bis zu 50 MHz auflösen. Mit Hilfe von Restgas können wir diese Teilchen in einer optischen Stehwelle, die aus zwei gegenläufigen Laserstrahlen geformt wird, stabil für mehr als 100 Tage levitieren. Dabei wird die formbedingte Orientierungsabhängigkeit der Polarisierbarkeit der Teilchen ausgenützt, um die Rotationsfreiheitsgrade der Stäbchen in der Falle zu kontrollieren. Durch Modulation der Polarisation zwischen linear und zirkular können wir die Drehbewegung eines Stäbchens so antreiben, dass sie einer externen Uhr mit hoher Präzision folgt. Mögliche Anwendungen für dieses System sind unter anderem präzise, lokale Messungen von Druck, Gasströmen und Lichtfeldern

oder Studien zur Einzelteilchen Thermodynamik. Um zukünftige Quantenexperimente in den Rotationsfreiheitsgraden zu realisieren und orientierungsabhängige Materiewelleninterferometrie zu ermöglichen, diskutiere ich, wie wir die Rotationsbewegung der Siliziumstäbchen in einem optischen Resonator kühlen können. Dabei stellt sich heraus, dass unter realistischen experimentellen Bedingungen das Erreichen des Grundzustandes der Bewegung von dielektrischen Stäbchen und Scheiben möglich ist.

1 Introduction: Towards high mass matter-wave interferometry

1.1 Matter-wave interferometry with complex (bio-)molecules and clusters

Matter-wave interferometry is founded on Louis de Broglie's hypothesis, that every particle of mass m and velocity v is associated with a wavelength $\lambda_{\mathrm{dB}} = h/mv$ [1]. A plethora of experiments revealed that diffraction and interference, which were previously only known for light, sound and other classical waves, can be observed with massive matter-waves on the single particle level too. The historic achievements have been summarised in the following review articles for electrons [2–4], neutrons [5], and atoms [6–8]. Since then, far-field diffraction experiments with helium clusters [9, 10], Mach-Zehnder interferometry with Sodium molecules [11], Ramsey-Bordé interferometry with SF_6 [12], Iodine [13] and Potassium molecules [14], Poisson spot experiments with Deuterium molecules [15] and quantum reflection of Helium dimers [16] have been realised. Nowadays, atom interferometry has reached a high level of experimental control, enabling quantum superpositions with separations on the half meter scale and precision tests of the equivalence principle [17] or general relativity [18]. Acceleration sensitivities of 10^{-10} g allow for precise measurements of gravitational gradients [19].

Over the last two decades, matter-wave interferometry has been extended to complex objects [20, 21], ranging from C_{60} and C_{70} fullerenes [22, 23] with 720 and 840 atomic mass units (amu), respectively, to biodyes [24], molecular clusters [25, 26], and fluorinated organic molecules with masses up to 10^4 amu [27, 28] in dedicated far-field diffraction machines [29–32] and near-field interferometers such as the *Talbot-Lau Interferometer* (TLI) [33], the *Kapitza-Dirac-Talbot-Lau Interferometer* (KDTLI) [34–36], the *Optical Time Domain Matter-Wave Interferometer* (OTIMA) [25, 37–40], and the *Long Baseline Universal Matter-Wave Interferometer* (LUMI). Recent advances have been made towards showing quantum interference with bio-molecules [41, 42]. By preparing the object in a spatial superposition, such experiments can, in principle, outperform the sensitivity of conventional (classical) methods of measuring gas-phase electrical, magnetic, and optical properties. For instance, interferometry has enabled the measurement of the molecular electronic properties of vitamins [43]. Apart from

quantum-assisted metrology experiments, fundamental questions of quantum theory can be addressed by probing the superposition principle with objects of increasing mass [37, 44, 45].

1.2 The limits of quantum mechanics

1.2.1 The measurement problem

Together with general relativity, quantum physics is the best tested fundamental theory of the twentieth century [46–48] and quantum effects have entered our everyday life through technologies such as transistors, lasers, MRI imagers, and atomic clocks. Yet, both theories are still fundamentally incompatible and quantum mechanics keeps us puzzled at the foundational level. It is still an open question why quantum superpositions, a consequence of the linearity of the Schrödinger equation, are not observed for macroscopic objects in our daily world, if the unitary evolution exists in systems of arbitrary size and complexity. This is the measurement problem [49]. Decoherence theory describes why macroscopic quantum phenomena can become unobservable when a system is coupled to an environment [50, 51]. However, the total system of quantum object plus environment should still evolve unitarily. This leads to entanglement between the quantum state and the environment and the emergence of quantum states of growing complexity, which shifts the measurement problem to larger scales [52]. It opens the way to paradoxes such as the famous Schrödinger cat Gedankenexperiment [53]. The lack of an objective collapse of the wave function in the measurement process has even be interpreted as the creation of new universes, proposed by Everett's many worlds hypothesis [54].

In a pragmatic approach, the Copenhagen interpretation [55, 56] circumvents the measurement problem by postulating a set of rules, which divide the micro- and the macro-world. However, this ultimately does not solve the measurement problem as the fundamental origin of these postulates remains unresolved [57] and the divide between the micro- and macro-world is only vaguely defined [49]. Another approach is taken by Tony Leggett, who introduces a disconnectivity parameter, quantifying how intrinsically different a macrostate is from the microstates of its constituents [58]. A possible, yet radical, way out is to modify the Schrödinger equation by adding stochastic non-linear terms, thereby introducing a collapse mechanism to suppress superpositions for macroscopic systems. A list of proposed modifications and their implication for matter-wave interferometry experiments with massive objects is given in the following section.

1.2.2 Collapse models

A number of collapse models have been proposed in which modifications to the Schrödinger equation lead to a spontaneous, objective and radical size reduction of the wave-function. These modifications must be nonlinear to break the superposition principle at the macroscopic level, stochastic to avoid superluminal communication, and they require an amplification term which keeps the linearity for small systems but suppresses superpositions of macroscopic objects [57]. In principle, all collapse models can be split into two categories: Collapse due to the interaction of the quantum state with a stochastic, non-quantum *measurement field*, which probes a superposition state and eventually suppresses it, or gravity-induced collapse where the gravitational (self-)interaction of a quantum-mechanical object in space-time leads to the loss of coherence [57].

The first of these models was formulated by Ghirardi, Rimini and Weber [60] and later generalised together with Pearle. It is nowadays known as continuous spontaneous localisation (CSL) theory [61, 62]. Later additions to those models have incorporated classical coloured noise [63, 64] and finite temperature noise of the collapse inducing background field [65]. The latter addition has emerged from the side-effect of all previous CSL models where the measurement field causes the system to heat up by continuous momentum kicks, thus violating energy conservation in the quantum system. Up to now, CSL induced heating has not been observed experimentally, however, it has also not yet been completely ruled out either. CSL models are characterised by two parameters, the rate λ_{CSL} at which a collapse occurs and the characteristic length r_{C} which characterizes the spatial resolution of the measurement field. As shown in Figure 1.1, a large area in parameter space has been ruled out using ultracold cantilevers [66], X-ray spectra [67], gravitational wave detectors [59] and matter-wave interferometry experiments [28, 37, 68, 69]. However, most of the parameter space has been explored by constraining the absence of heating rather than direct observation of superposition states. It is still an open debate whether all CSL models can be ruled out non-interferometrically, i.e. without observing quantum superpositions in the first place [69].

While the nature of the classical measurement field proposed by CSL has remained unspecified [45], some theories predict a collapse mechanism induced by gravity [70–72], where either fluctuations in space-time or a gravitational self-interaction between the superposition states are believed to cause a collapse.

In the following, I will discuss an experimental scheme that aims at pushing the bounds previously set by matter-wave interferometry in the KDTLI [28]. It is based on the various matter-wave experiments completed in the Quantum Nanophysics Group at the University of Vienna and theoretical work by the theory group around Klaus Hornberger in Duisburg. It also expands on a recent proposal by James Bateman and

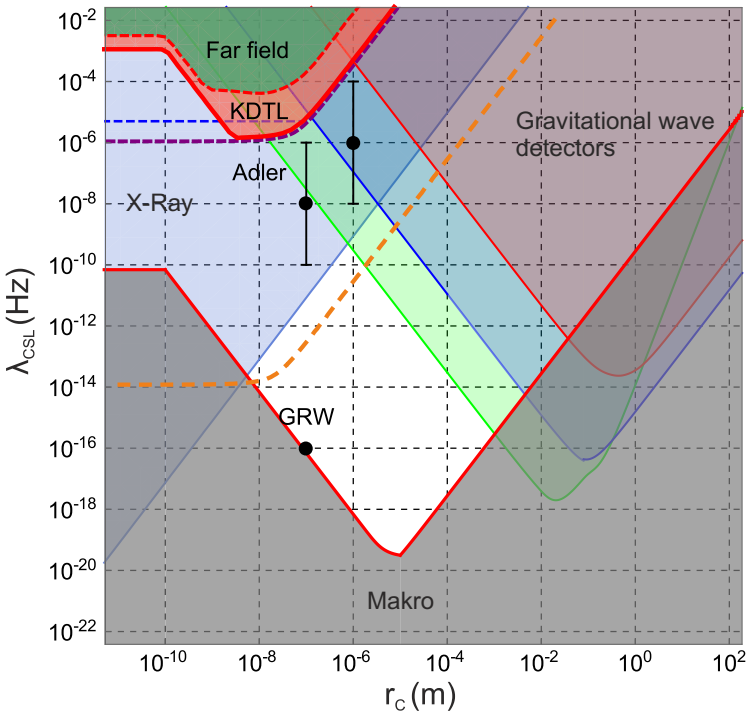

Figure 1.1: Parameter space of the CSL model. The shaded areas indicate the excluded values for the localisation rate λ_{CSL} and the characteristic length r_{C}. The lower bound (red line at the bottom) is given by the requirement that CSL models suppress the superposition of macroscopic objects for known physical and astrophysical processes. The upper bounds are set by matter-wave interferometry in KDTLI [28] and far field diffraction [29]. X-ray experiments (top left blue shaded region) exclude the top left corner of the parameter space, however, only for a subset of CSL models. Gravitational wave detectors exclude the top right corner of the CSL parameters (red,blue, and green shaded areas) [59], but also do not apply to all CSL models. The dashed orange line indicates the excluded area by high-mass matter-wave interferometry with 10^7 amu particles as proposed in Section 1.3.2. Figure adapted from M. Toroš et al., arXiv:1601.03672.

colleagues [73], aiming at pushing their proposed limits by an order of magnitude to particles in the range of 10^7 amu. On Earth, these concepts may be eventually extended to 10^8 amu in a nanoparticle fountain or in high drop tower experiments. The proposed experiment will directly rule out localisation rates of $\lambda_{\mathrm{CSL}} > 10^{-13}$ Hz at $r_{\mathrm{C}} \simeq 10^{-7}$ m (see Figure 1.1 and Section 1.3.3). To test the full CSL parameter space and gravity-induced collapse models, however, superpositions of objects beyond the proposed masses will be necessary, raising the need for alternative experimental approaches which involve experiments in outer space [74] or interferometry with particles levitated in optical [75–77] or magnetic [78, 79] fields.

1.3 Roadmap to interferometry with $10^6 - 10^7$ amu nanoparticles

1.3.1 Interferometric scheme

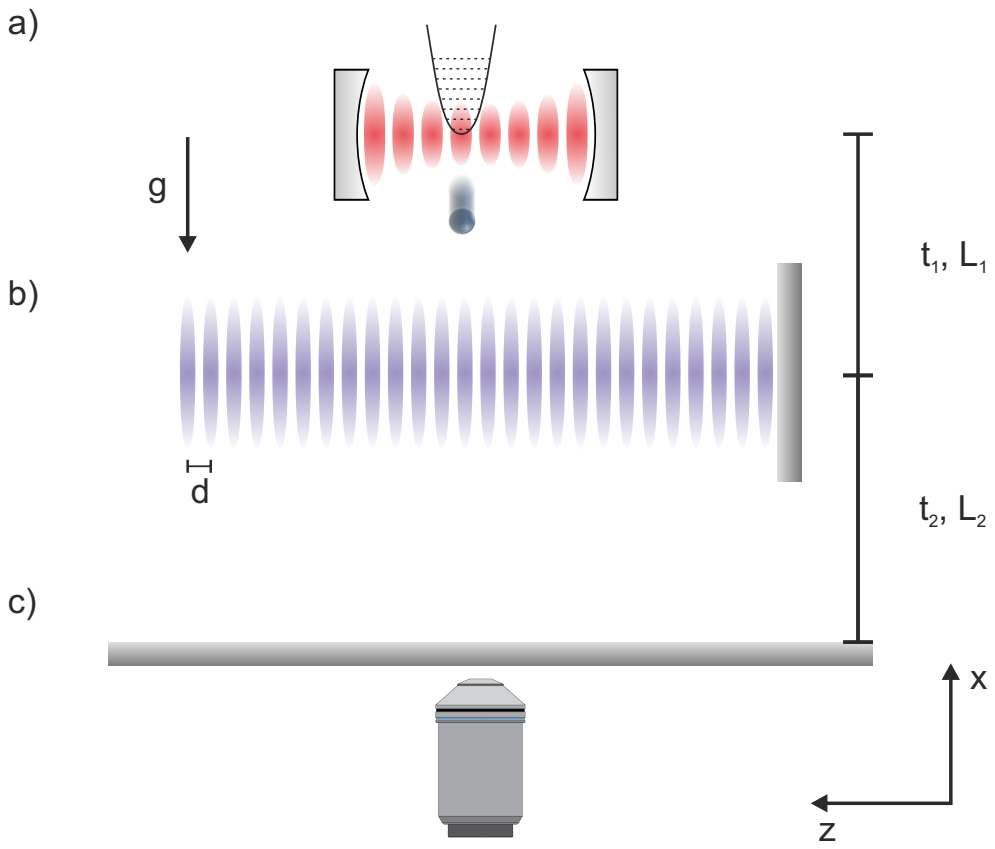

Figure 1.2: Scheme for near-field interferometry with $10^6 - 10^7$ amu nanoparticles in free fall. a) Single nanoparticles are cooled inside an optical cavity while they pass through, or are trapped by the cavity field. In this way, the particles are localized to create sufficiently large spatial coherence and coherently illuminate the grating. b) After a free fall time t_1 the particles are illuminated by a standing light wave formed by a back-reflected laser pulse. It either acts as a phase or ionization + phase grating (depending on the work function of the nanoparticles and the photon energy) with grating period $d = \lambda_{\text{grating}}/2$. After the grating, a near-field interference pattern builds up. c) This fringe pattern with the periodicity $D = d\,(t_1 + t_2)\,/t_1$ [73] can be observed after another free fall time t_2 by collecting the nanoparticles on a sample plate and detecting them either using optical or electron microscopy.

In order to push earth-bound matter-wave interferometry with freely propagating particles to its high-mass limits, we consider a vertical interferometer, as sketched in Figure 1.2. We partially follow the scheme proposed in Reference [73] and the theory

developed in References [20, 68]. Silicon nanoparticles are launched through or dropped from a high finesse optical cavity. During the interaction time with the cavity field the particle's center-of-mass (COM) motion along the cavity axis is cooled and localized to $5-10\,\mathrm{nm}$ within a single anti-node, as described in Chapter 3. Starting from this point-like source the particles drop for a time t_1 and distance L_1 before they are illuminated by a UV laser pulse which forms a standing light wave with grating period $d = \lambda_{\mathrm{grating}}/2$. Depending on the particle's initial localization, the width of the coherence function for their initial Gaussian state spreads over multiple nodes and anti-nodes and the particles coherently illuminate the grating. The photon energy $E_\nu = hc/\lambda_{\mathrm{grating}}$ in comparison to the particle's work function W determines whether the standing light wave either acts as phase- or ionization + phase grating [80].

After the grating pulse, the particles fall for a time t_2 and distance L_2. Then their associated de Broglie waves have emerged into an interference pattern, according to the Talbot effect [81]. H. F. Talbot predicted optical self-imaging of a periodic grating. For coherent light diffracted at the grating, the near-field interference pattern resembles the grating structure at integer multiples n of a characteristic distance, the Talbot length d_{T} or Talbot time t_{T}. The number of coherently illuminated grating slits multiplied by d_{T} defines the depth of this near-field region. For matter-wave interferometry with particles of mass m, t_{T} is given as $t_{\mathrm{T}} = md^2/h$. Under coherent illumination of the grating with a plane wave, the interference pattern at times $t = nt_{\mathrm{T}}$ resembles the periodic grating structure [20, 25, 68, 80]. In case of illumination from a point-like source, the *effective* time $t_1 t_2/\left(t_1 + t_2\right)$ must be an integer multiple of t_{T} to obtain an interference pattern with a geometrically magnified periodicity $D = d\mu$ and magnification factor $\mu = \left(t_1 + t_2\right)/t_1$ [73]. For the parameters discussed in this chapter, $D = 140 - 330\,\mathrm{nm}$. The particles can therefore be collected on a sample plate at a distance L_2 from the grating pulse where their fringe pattern can be detected via optical scattering [82, 83] or electron microscopy of the deposited particles.

1.3.2 Experimental feasibility

In order to keep the de Broglie wavelength on the order of $10^{-12}\,\mathrm{m}$, at which interference patterns can still be resolved, the particles need to be as slow as possible. This comes at the expense of increasing flight times within the interferometer. A free fall experiment, as proposed here, requires an interferometer length of more than 5 m for masses beyond 10^7 amu. To determine the required interferometer length the following considerations must be taken into account:

At first we consider a phase grating which imprints a phase ϕ_0 onto the matter wave associated with particles of radius R and mass m. The maximum value of that phase at an anti-node of the grating depends on the particle's optical polarizability α as well as the laser pulse energy E_{G} and spot area a_{G} via $\phi_0 = 2\mathrm{Re}(\alpha)E_{\mathrm{G}}/\hbar c\varepsilon_0 a_{\mathrm{G}}$. In addition,

each particle may absorb a maximum number of $n_0 = 2\phi_0\beta$ photons when passing through an anti-node of the grating. This number scales with the material parameter $\beta = \mathrm{Im}(\alpha)/\mathrm{Re}(\alpha)$ [68]. A list of values for α, β, and n_0 at all relevant wavelengths is given in Appendix A.

For the proposed interferometer, the expected interference pattern exhibits a sinusoidal modulation. It can be calculated by applying a series of transformations, accounting for free fall, decoherence and the grating interaction, which consists of a coherently accumulated phase and momentum kicks due to absorption. A detailed derivation can be found in References [68, 73]. The sinusoidal fringe visibility V_{vis} of the near-field interference pattern is proportional to the absolute value of the *Talbot* coefficient B_1 as $V_{\mathrm{vis}} \propto 2\,|B_1(\xi)|$. Expressed in terms of Bessel functions, B_1 is given by [68, 73]

$$B_1(\xi) = e^{-\zeta_{\mathrm{abs}}(\xi)} \sqrt{\frac{\zeta_{\mathrm{coh}}(\xi) + \zeta_{\mathrm{abs}}(\xi)}{\zeta_{\mathrm{coh}}(\xi) - \zeta_{\mathrm{abs}}(\xi)}} J_1\left[\mathrm{sgn}\left[\zeta_{\mathrm{coh}}(\xi) - \zeta_{\mathrm{abs}}(\xi)\right] \sqrt{\zeta_{\mathrm{coh}}(\xi)^2 - \zeta_{\mathrm{abs}}(\xi)^2}\right], \tag{1.1}$$

with $\zeta_{\mathrm{coh}}(\xi) = \phi_0 \sin(\pi\xi)$ and $\zeta_{\mathrm{abs}}(\xi) = \beta\phi_0(1 - \cos(\pi\xi))$. For the proposed interferometric scheme, the parameter ξ is given by the times t_1, t_2 and t_{T}, $\xi = t_1 t_2 / t_{\mathrm{T}}(t_1 + t_2)$.

Also the classical ballistic trajectories of the particles result in a periodic density modulation behind the grating due to the strong dipole forces in the standing light wave. To calculate the fringe visibility of the classically expected pattern, $\zeta_{\mathrm{coh}}(\xi)$ in equation 1.1 needs to be replaced with $\phi_0\pi\xi$ [68, 73]. For a grating with $\lambda_{\mathrm{grating}} = 213\,\mathrm{nm}$ and 1×10^7 amu nanoparticles the difference between quantum and classical fringe visibility is shown in Figure 1.3a & b.

For short laser wavelengths the photon energy $E_\nu = hc/\lambda$ can exceed the work function of the nanoparticle. In this case, the absorption of a grating photon ionizes the particle, which can then be removed by an external electric field so as not to contribute to the interference pattern. The grating therefore acts as a mask which imprints a periodic transmission function with period d onto the nanoparticle beam. The Talbot coefficients then read [68]

$$B_{1,\mathrm{ion}}(\xi) = e^{-\phi_0\beta} \sqrt{\frac{\zeta_{\mathrm{coh}}(\xi) - \zeta_{\mathrm{ion}}(\xi)}{\zeta_{\mathrm{coh}}(\xi) + \zeta_{\mathrm{ion}}(\xi)}} J_1\left[\mathrm{sgn}\left[\zeta_{\mathrm{coh}}(\xi) + \zeta_{\mathrm{ion}}(\xi)\right] \sqrt{\zeta_{\mathrm{coh}}(\xi)^2 - \zeta_{\mathrm{ion}}(\xi)^2}\right], \tag{1.2}$$

with $\zeta_{\mathrm{ion}}(\xi) = \phi_0\beta\cos(\pi\xi)$.

Again, the fringe visibility due to ballistic trajectories can be obtained by substituting $\zeta_{\mathrm{coh}}(\xi)$ and $\zeta_{\mathrm{ion}}(\xi)$ by $\phi_0\pi\xi$ and $\phi_0\beta$, respectively. Figure 1.3c & d shows the quantum and classical sinusoidal fringe visibility for $\lambda_{\mathrm{grating}} = 213\,\mathrm{nm}$ and $m = 1 \times 10^7$ amu. In contrast to the phase grating, the density modulation of the nanoparticles shows a high fringe visibility at the position of the grating, due to the mask imprinted by the

ionizing grating.

For silicon, the work function takes values of $4.6 - 4.9\,\mathrm{eV}$ depending on the crystal structure and doping of the material [84]. Therefore, for gratings with $\lambda_{\mathrm{grating}} \lesssim 260\,\mathrm{nm}$ ionization of the particles occurs. Native oxide layers due to the exposure of the particles to air, however, could increase the particles' work function significantly by up to $0.8\,\mathrm{eV}$ per monolayer [85, 86]. For the proposed interferometer, however, the difference in optimal length between phase and ionization gratings is on the level of a few percent.

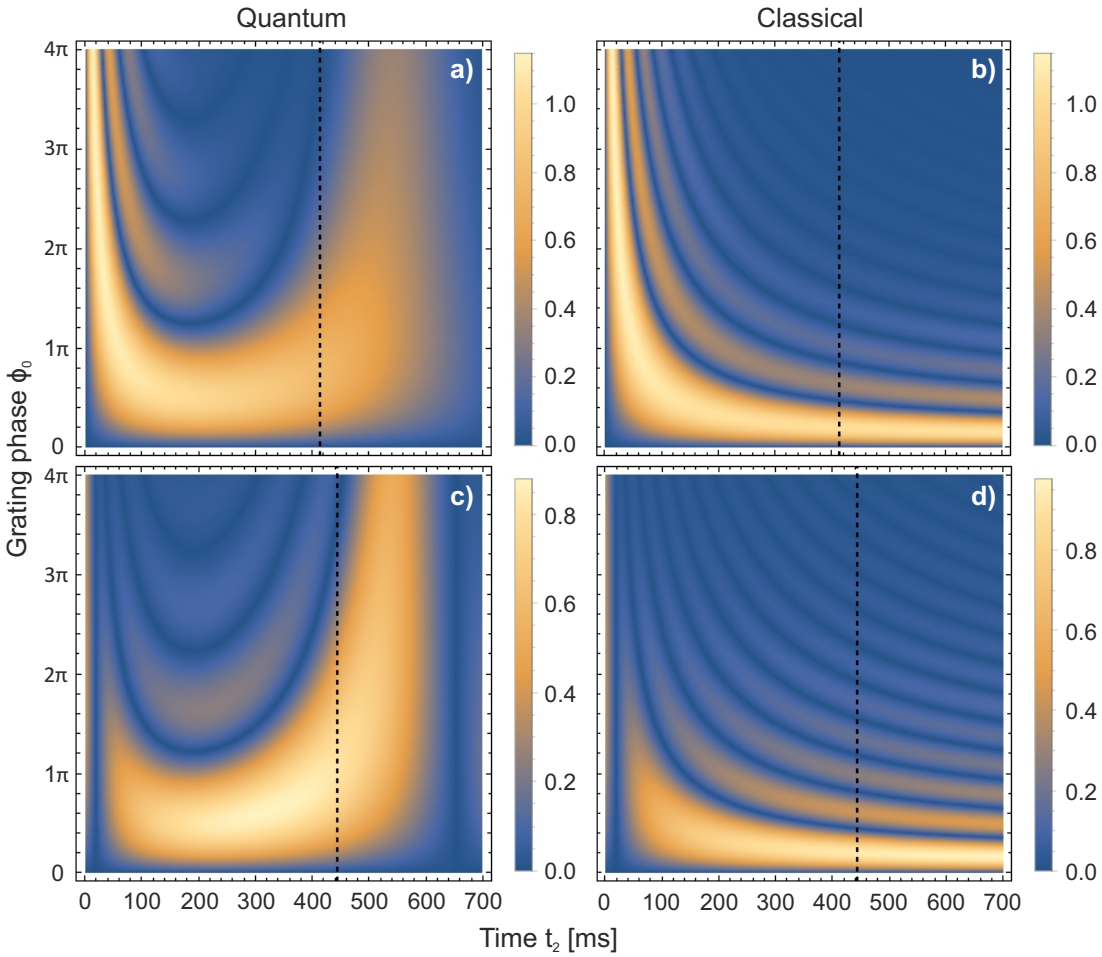

Figure 1.3: Quantum versus classical sinusoidal fringe visibility for near-field interferometry with 10^7 amu silicon particles and $\lambda_{\mathrm{grating}} = 213\,\mathrm{nm}$ as a function of the free fall time t_2 and the grating phase ϕ_0. The free fall time t_1 is set to $2t_{\mathrm{T}}$. a) Visibility of the quantum contrast and b) classical pattern in the case of a phase grating, including absorption of grating photons. c) Visibility of the quantum contrast and d) classical pattern in the case of photoionization and phase contribution. The time t_2 for highest quantum versus fringe visibility for both cases is marked by vertical dashed lines in a) & b) and c) & d) respectively. A plot along these lines is shown in Figure 1.5.

To determine the optimal interferometer length L_{tot} for particles of given mass and grating wavelength we optimize ξ to maximize the quantum fringe visibility while minimizing the classical visibility. For any free fall time t_1 from the source to the grating, this sets an optimal time t_2, a total free-fall time $t_{\mathrm{tot}} = t_1 + t_2$ and interferometer length $L = g(t_1 + t_2)^2/2$. In the following, the time t_1 is set to be $2t_{\mathrm{T}}$, which facilitates a coherent illumination of the grating while keeping the interferometer as short as possible. Figure 1.4a shows the required interferometer lengths for various grating wavelengths (3^{rd}, 4^{th} and 5^{th} harmonic of a Nd:YAG laser at 355/266/213 nm, respectively, and an F_2 excimer laser at 157 nm) as a function of particle mass. A list of ideal interferometer configurations is given in Appendix A.

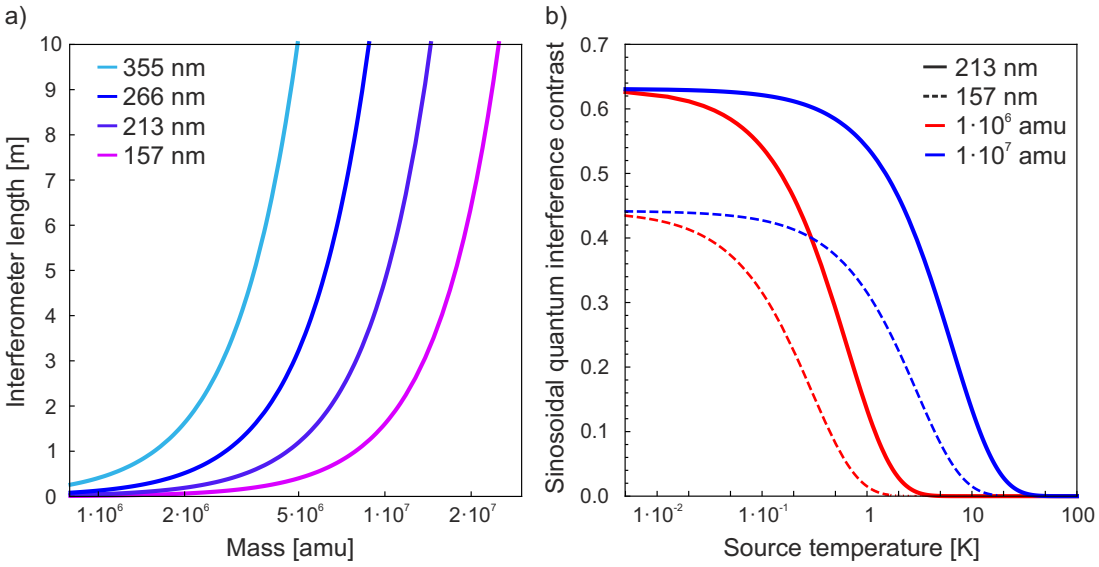

Figure 1.4: Required interferometer lengths and source temperatures for near-field interferometry starting from a point-like source as outlined in Figure 1.2. a) Scaling of the required interferometer length with the nanoparticle mass for various grating wavelengths of 157 nm (pink), 213 nm (purple), 266 nm (blue), and 355 nm (light blue). We assume the grating to act as a phase grating including absorption (the dielectric properties of silicon at these wavelengths are listed in Appendix A). b) Interference contrast (sinusoidal fringe visibility) as a function of the particle temperature in the cavity. We consider an axial cavity trap frequency of $\nu_{\mathrm{trap}} = 200\,\mathrm{kHz}$, grating wavelengths of 213 nm (solid lines) and 157 nm (dashed lines), and particle masses of 1×10^6 amu (red) and 1×10^7 amu (blue), respectively. For sufficiently low particle temperatures the source prepares nanoparticles with high enough spatial coherence to achieve maximal interference visibilities.

To test the quantum nature of the observed fringe visibility, the grating phase ϕ_0 and number of absorbed photons n_0 can be scanned by varying the pulse energy of the grating laser. This corresponds to moving along the vertical dashed lines in Figure 1.3. A plot along these lines in Figure 1.5 shows the different scaling of quantum and classical

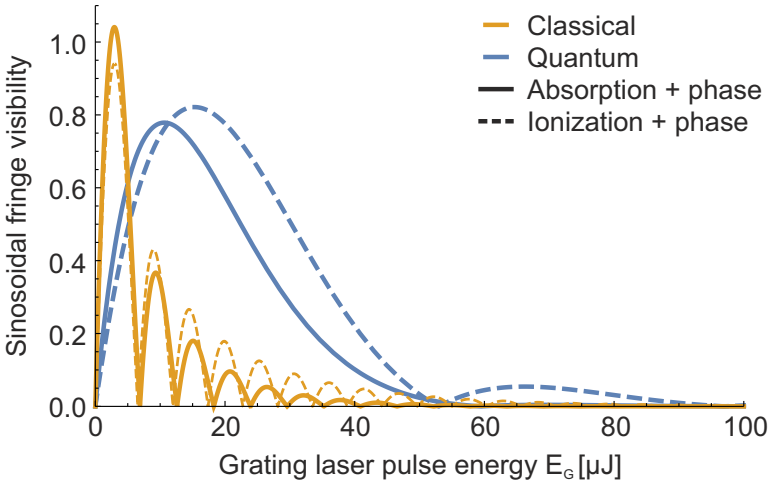

Figure 1.5: Scan over the grating phase by changing the pulse energy of the laser. We assume a nanoparticle mass of 10^7 amu, a laser wavelength of 213 nm, a spot radius of 50 mm, free-fall times $t_1 = 2t_T = 574$ ms and $t_2 = 445$ ms with and 413 ms without ionisation, a nanoparticle temperature $T_{com} = 10$ mK, and a trapping frequency $\nu_{trap} = 200$ kHz. The sinusoidal fringe visibility in the quantum and classical case are plotted as a function of pulse energy E_G for both a phase and ionizing + phase grating. In both cases the quantum interference and the ballistic trajectories can be distinguished unambiguously.

visibility for both a phase and ionizing grating with a grating laser beam waist radius of 50 mm.

As mentioned before, starting from a well-localized source is critical to obtain the required transverse coherence within the interferometer. To specify the necessary source requirements, we assume the nanoparticle to be harmonically trapped in the axial direction of the cavity field, both in the cases of a particle transiting the cavity mode (see section 2.3) or being three-dimensionally trapped and released. The motion of the harmonically trapped particle can be quantified using its mean thermal occupancy $\langle n \rangle = k_B T_{com}/\hbar\omega_{trap}$, with T_{com} the center of mass temperature corresponding to the 1D particle motion along the cavity axis, and ω_{trap} the angular trapping frequency. The position and momentum uncertainty of the particle therefore are given by

$$\begin{aligned} \Delta z &\simeq \sqrt{n}\sqrt{\frac{\hbar}{m\omega_{trap}}} = \sqrt{\frac{k_B T_{com}}{(2\pi)^2 \nu_{trap}^2 m}}, \\ \Delta p &\simeq \sqrt{n}\sqrt{m\hbar\omega_{trap}} = \sqrt{m k_B T_{com}}. \end{aligned} \tag{1.3}$$

The sinusoidal fringe visibility of the observed pattern scales with the initial localization Δz and thus the particle temperature T_{com} within the cavity field as $V_{vis} \propto \exp(-2\pi^2 \Delta z^2 t_2^2/d^2(t_1+t_2)^2)$, thereby accounting for a non-perfectly coherent illumi-

nation of the grating [73]. Figure 1.4b shows this dependence for 10^6 amu and 10^7 amu particles and grating wavelengths of 157 nm and 213 nm. For 10^7 amu particles a source temperature of below 50 mK and a trap frequency of $\nu_{\text{trap}} = 200$ kHz ensure the fringe visibility to be affected by less than a few percent due to the spatial coherence of the particles.

For technical reasons, further source requirements have to be met: Sufficiently many particles must be counted in order to resolve the interference pattern. In addition, a homogeneous illumination of the particles by the grating pulse must be ensured due to the intensity dependent phase that is imprinted onto the particles. The particle velocities in y-direction thus also become important. As discussed in Chapter 3, cavity cooling can also cool the y-component of the particle velocity. To ensure the particle beam to only interact with the central 10 mm region of the 50 mm wide grating spot (less than 1% variation of the pulse energy) a velocity of less than 16 mm/s in y-direction or an initial temperature of less than 160 mK is required. This leads to an extent of the interference pattern at the detection plate of 32 mm in the case of an interferometer designed for 10^7 amu particles at $\lambda_{\text{grating}} = 213$ nm. The resulting sinusoidal fringes with periodicity $D = 180$ nm for silicon nanoparticles of 25 nm diameter can be detected by means of interferometric scattering microscopy [82, 83] or electron microscopy.

In addition, this interferometer scheme requires the particles to be dropped from the same anti-node of the cavity field. The miss-match between cavity and grating wavelength would result in an incoherent addition of the interference patterns for particles originating from different initial locations, leading to the total smearing of the interference contrast. Loading particles into this sub-micron region will be a major challenge but could be solved by employing cryogenic sources and additional laser fields to guide the particles into the cavity, as discussed in Chapter 5. Additional optical dipole traps, as discussed in Chapter 3, may also be capable of delivering particles to the right position within the cavity field [87]. In dedicated microcavities (see Section 3.2), which will be capable of cooling 10^7 amu particles, only a total number of $40 - 50$ anti-nodes will be supported. Detecting the position of the particle will therefore be possible either via scattering, or the particle coupling rates, measured with two neighbouring longitudinal modes of the cavity (see Chapter 3).

A photoionization grating reduces the amount of transmitted particles by a transmission probability [39, 68]

$$T = \frac{1}{d}\int_{-d/2}^{d/2} \exp\left[-2\phi_0\beta\cos^2\left(\frac{\pi z}{d}\right)\right] dz. \tag{1.4}$$

In the case of a $d = 157/2$ nm grating this probability at the pulse energy corresponding to the highest quantum fringe contrast ($\beta = 0.474$, $n_0 = 3.42$) amounts to 34%. For $d = 213/2$ nm ($\beta = 0.207$, $n_0 = 1.54$) the transmission goes up to 53%.

To collect a sufficient number of particles to form an interference pattern, while keeping the interferometer stable, the cooling stage should operate with short duty cycles. Typically a few thousand particles are sufficient to keep the $1/\sqrt{N}$ noise at a level of a few percent. For the nanoparticle launching techniques discussed in Chapter 2, nanoparticles can be loaded into the interferometer at a rate of up to 50 Hz. For optimised two-mode cavity cooling [88, 89] (see Section 3.1.2), interaction times of the particle with the cavity fields of a few milliseconds are sufficient to cool the particle motion down to the required temperature. This is compatible with the repetition rate in state of the art nanoparticle sources.

1.3.3 Sources of decoherence

Besides the challenge of building a sufficiently long vertical interferometer to resolve the interference pattern of nanoparticles with masses up to 10^7 amu, decoupling the experiment from the environment poses additional experimental demands. Already at particle masses below 10^4 amu, various decoherence mechanisms need to be considered to avoid reduced fringe visibilities in state of the art interferometers [20, 21, 90, 91]. All decoherence mechanisms scale unfavourably with larger interferometer sizes and higher particle masses, making high-mass matter-wave interferometry challenging.

We will discuss the most relevant sources of decoherence and the limits they pose for the proposed interferometric scheme, such as the emission, absorption and scattering of thermal photons and collisions with residual gas molecules. Absorption of grating photons is already included in the calculations for the sinusoidal fringe visibilities (Equations 1.1 and 1.2). It enters through the power dependent phase ϕ_0 and material parameter β resulting in a number of $n(z) = 2\phi_0\beta\cos^2(\pi z/d)$ photons which are absorbed during the time of the grating pulse at position z in the standing light wave. Again, detailed derivations can be found in References [68, 73].

Scattering of grating photons

Scattering of grating photons adds an incoherent term to the phase grating operation. It is quantified by the number of scattered photons at position z in the grating which is given by $n_{\mathrm{sca}}(z) = 2\eta\phi_0\cos^2(\pi z/d)$ [73] with

$$\eta = \frac{2}{3}\left(\frac{2\pi R}{\lambda_{\mathrm{grating}}}\right)^3 \frac{|\varepsilon(\omega)-1|^2}{|\varepsilon(\omega)|^2 + \mathrm{Re}\left[\varepsilon(\omega)\right] - 2}. \tag{1.5}$$

For silicon particles of $m = 10^7$ amu and $\lambda_{\mathrm{grating}} = 157$ nm this amounts to $\eta = 0.16$ (the dielectric properties of bulk silicon are given in Appendix Figure A.1). Re-evaluating Equations 1.1 and 1.2 including incoherent momentum kicks due to scattering of grating photons (see Reference [73]) leads to the conclusion that for silicon particles with masses

higher than a few 10^6 amu, scattering plays a crucial rule and can't be neglected as it would lead to a substantial reduction of the interference contrast. To reach high particle masses in an interferometer based on a non-ionizing grating a wavelength of $\lambda_{\text{grating}} = 213\,\text{nm}$ is the best choice, with $\eta < 0.04$ for 10^7 amu particles.

For ionization gratings, however, in which the particles that interact with the high field regions of the standing light wave get ionized and removed from the particle beam when they absorb a photon, the ratio of absorption over scattering cross-section is the important figure of merit. Only for those particles, which scatter a photon without absorbing one, can decoherence occur. The ratio of absorption over scattering cross-section is given by [68]

$$\frac{\sigma_{\text{sca}}}{\sigma_{\text{abs}}} = \frac{4\pi^2 m}{3\rho\lambda_{\text{grating}}^3} \frac{|\varepsilon - 1|^2}{\text{Im}(\varepsilon)}, \tag{1.6}$$

with the particle density $\rho = 2330\ \text{kg/m}^3$ in case of silicon. For 10^7 amu particles this ratio amounts to 0.34 and 0.18 for a grating wavelength of 157 nm and 213 nm, respectively. As discussed in detail in reference [68] for values of this order of magnitude a reduction of fringe visibility of approximately 10% and a shift of ideal interferometer parameters of a few percent will occur.

Emission of thermal photons

Unlike the case of atomic BECs, there is no need to prepare the internal state of the nanoparticles within the interferometer when we consider single-particle interference. However, when the internal degrees of freedom couple to the motional state of the particles, decoherence can reduce the interference fringe visibilities. For instance, the emission of thermal photons can lead to *which-path information* that eventually decoheres the quantum state. The longer a particle transits through the interferometer the more likely such an event becomes. While for near-field interferometry with comparably light C_{70} molecules (840 amu), the thermal radiation of photons only leads to a reduction of interference visibility at internal temperatures exceeding 1300 K [91], for interference with 10^7 amu particles the temperature requirements are far more stringent.

When the internal temperature T_{int} of the particles exceeds that of the environment T_{env}, i.e. $T_{\text{int}} \gg T_{\text{env}}$, the spectral emission rate is given by [73]

$$\gamma_{\text{emi}}(\omega, T_{\text{int}}) = \frac{4}{\pi}\left(\frac{\omega R}{c}\right)^3 \exp\left(-\frac{\hbar\omega}{k_{\text{B}} T_{\text{int}}}\right) \text{Im}\left(\frac{\varepsilon(\omega) - 1}{\varepsilon(\omega) + 2}\right). \tag{1.7}$$

This leads to a reduced sinusoidal fringe visibility $R_{\text{emi}} \cdot V_{\text{vis}}$ with [73]

$$R_{\text{emi}} = \exp\left[-\int \text{d}\omega \int_0^1 \text{d}\vartheta (t_1 + t_2)\gamma_{\text{emi}}\left(\omega, T_{\text{int}}\right)\left[1 - \text{sinc}\left(\frac{h\omega t_2}{\mu m c d}\vartheta\right)\right]\right]. \tag{1.8}$$

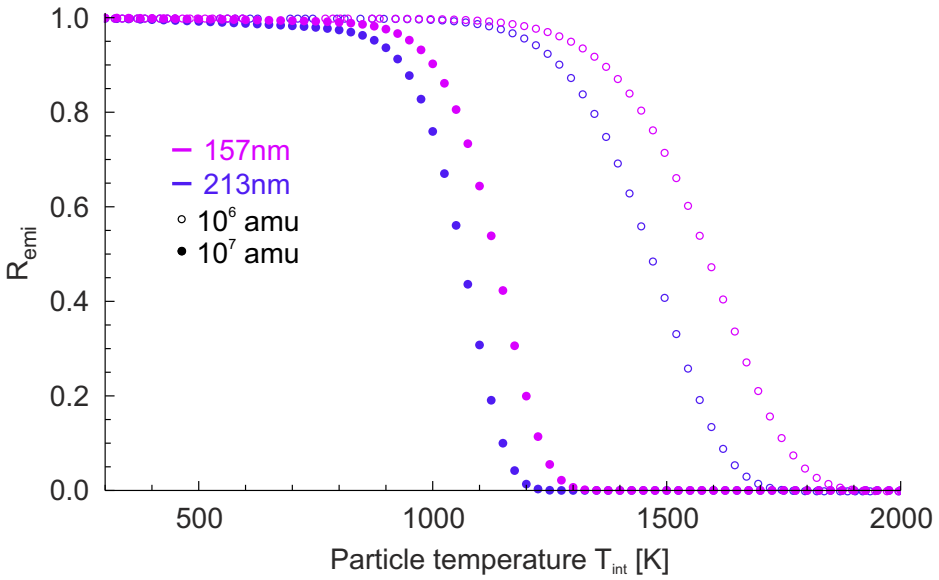

Figure 1.6: Reduction of the fringe visibility due to emission of thermal photons. By evaluating Equation 1.8, using the dielectric properties of bulk silicon as listed in Appendix A, the reduction factor for the fringe visibility of 10^6 amu (empty circles) and 10^7 amu silicon nanoparticles (full circles) for a grating wavelength of $\lambda_{\text{grating}} = 157\,\text{nm}$ (purple) and 213 nm (blue) depending on the internal temperature T_{int} is plotted. For 10^7 amu particles and a 213 nm grating, internal temperatures of up to 700 K can be reached before thermal decoherence kicks in. For the calculations we assume a temperature of the environment of $T_{\text{env}} = 300\,\text{K}$ and free fall times as listed in Table A.2.

Due to silicon being a poor emitter of thermal radiation, the internal temperature of the particles after releasing them from the cavity can be considered constant. For silicon particles with masses $m = 10^6$ and 10^7 amu the temperature dependent reduction factor of the fringe visibility due to thermal decoherence is shown in Figure 1.6 for two different interferometer configurations. In case of 10^6 amu silicon nanoparticles in a 213 nm grating internal temperatures below 1100 K need to be achieved. 10^7 amu particles require temperatures colder than 700 K such that the interference pattern is not affected by thermal decoherence. This corresponds to silicon interacting with the cavity field (intra-cavity intensity $I_{\text{cav}} \simeq 1 \times 10^7\,\text{W cm}^{-2}$) for less than 1350 ms.

Absorption of thermal photons

Emission of thermal photons from the interferometer chamber and absorption by the nanoparticles lead to a momentum kick and therefore decoherence. At a temperature T_{env} of the environment the absorption rate of thermal photons derived from the Planck

formula is given by [68, 73]

$$\gamma_{\mathrm{abs}} = \frac{4(\omega R/c)^3/\pi}{\exp\left(\hbar\omega/k_{\mathrm{B}}T_{\mathrm{env}}\right) - 1} \mathrm{Im}\left[\frac{\varepsilon(\omega) - 1}{\varepsilon(\omega) + 2}\right]. \tag{1.9}$$

In analogy to the case of emission of thermal photons, the dielectric properties of silicon (see Appendix A) are used to determine the reduction factor R_{abs} of the interference visibility due to the absorption of thermal photons [73]

$$R_{\mathrm{abs}} = \exp\left[-\int \mathrm{d}\omega \gamma_{\mathrm{abs}}(\omega)\left(1 - \frac{\mathrm{Si}\left(h\omega t_2/\mu m c d\right)}{h\omega t_2/\mu m c d}\right)(t_1 + t_2)\right], \tag{1.10}$$

with $\mathrm{Si}(x) = \int_0^x \sin(t)/t \, \mathrm{d}t$ the sine integral.

Due to the low absorption of silicon at thermal photon wavelengths, decoherence for particles with masses $\leq 1 \times 10^7$ amu is negligible in an interferometric scheme as proposed here.

Scattering of thermal photons

Instead of being absorbed by the particle, thermal photons can be scattered, transferring momentum and leading to decoherence. The rate at which these scattering events happen for the interferometer being at room temperature is given by [68, 73]

$$\gamma_{\mathrm{sca}}(\omega) = \frac{8(\omega R/c)^6/3\pi}{\exp\left(\hbar\omega/k_{\mathrm{B}}T_{\mathrm{env}}\right) - 1} \left|\frac{\varepsilon(\omega) - 1}{\varepsilon(\omega) + 2}\right|^2, \tag{1.11}$$

leading to a fringe visibility reduction [68, 73]

$$R_{\mathrm{sca}} = \exp\left[\int \mathrm{d}\omega \gamma_{\mathrm{sca}}(\omega)\left(\frac{\mathrm{Si}\left(2h\omega t_2/\mu m c d\right)}{h\omega t_2/\mu m c d} - \mathrm{sinc}\left(\frac{h\omega t_2}{\mu m c d}\right) - 1\right)(t_1 + t_2)\right]. \tag{1.12}$$

As in the case of absorption of thermal photons, this decoherence mechanism can be neglected here for the experiment being at room temperature.

Collisions with residual gas particles

In analogy to scattering of photons, the particle collisions with residual gas particles exert momentum kicks at a rate Γ_{col} leading to decoherence. For growing free-fall times this poses additional constraints on the vacuum system employed in the experiment. We assume a residual nitrogen gas with pressure p_g, temperature T_{env} and mean velocity of the gas particles $v_{\mathrm{g}} = \sqrt{2k_{\mathrm{B}}T_{\mathrm{env}}/m_{\mathrm{g}}}$. From a van der Waals scattering model an approximate expression for the collision rate is given by [68, 73, 90, 92]

$$\Gamma_{\mathrm{col}} \approx \frac{4\pi\Gamma(0.9)}{5\sin(\pi/5)}\left(\frac{3\pi C_6}{2\hbar}\right)^{2/5} \frac{p_{\mathrm{g}} v_{\mathrm{g}}^{3/5}}{k_{\mathrm{B}}T_{\mathrm{env}}}, \quad C_6 \approx \frac{3\alpha(\omega = 0)\alpha_{\mathrm{g}} E_{\nu,\mathrm{g}} E_\nu}{32\pi^2\varepsilon_0^2(E_\nu + E_{\nu,\mathrm{g}})}, \tag{1.13}$$

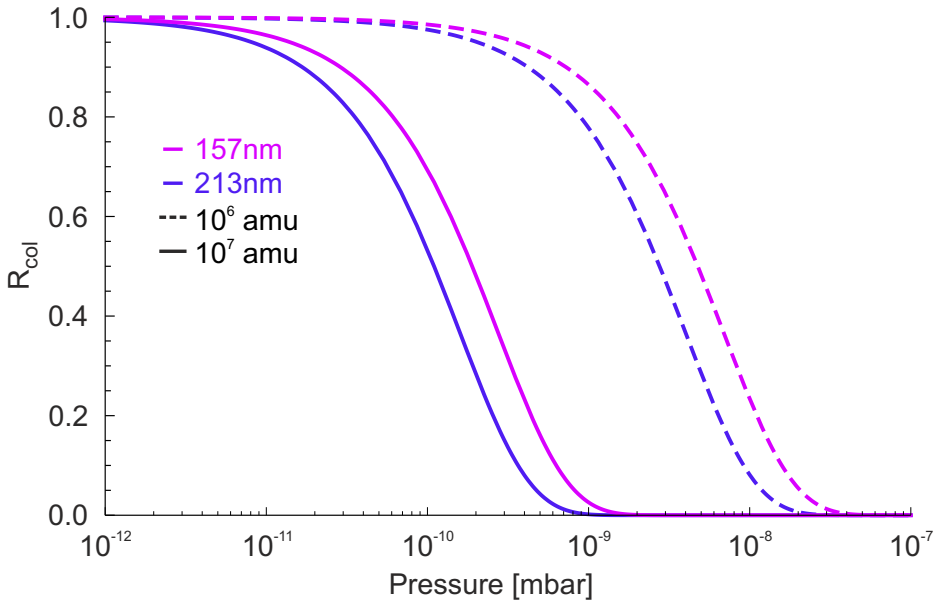

Figure 1.7: Reduction of the fringe visibility due to elastic scattering of residual gas particles. For an ambient temperature of $T_{\mathrm{env}} = 300\,\mathrm{K}$ the pressure dependence of the reduction factor R_{col} is plotted for 10^6 amu (dashed lines) and 10^7 amu (solid lines) for grating wavelengths of 157 nm (purple) and 213 nm (blue).

with $\alpha = 0.784 \times 4\pi\varepsilon_0 R^3$ and $\alpha_{\mathrm{g}} = 1.74 \times 4\pi\varepsilon_0\,\text{Å}^3$ the static polarisabilities of the particle and the gas molecules, respectively, and $E_\nu = 4.5\,\mathrm{eV}$ and $E_{\nu,\mathrm{g}} = 15.6\,\mathrm{eV}$ their ionisation energies. Figure 1.7 shows the reduction factor $R_{\mathrm{col}} = \exp\left[-\Gamma_{\mathrm{col}}(t_1 + t_2)\right]$ of the interference visibility due collisions with residual nitrogen gas as a function of the pressure p_{g} within the interferometer. Assuming an ambient temperature of $T_{\mathrm{env}} = 300\,\mathrm{K}$ pressures on the order of 10^{-12} mbar need to be achieved to preserve the interference contrast. Using cryogenic environments, pressures down to 5×10^{-17} mbar have been reported [93, 94]. State of the art non-evaporative getter pumps in combination with coated vacuum chambers, achieve pressures down to 10^{-14} mbar [95].

Stability of the interferometer

The requirements on the stability of the grating with respect to the source is comparable to the limits on the initial localisation of the particles in the source [73]. The mirror forming the standing light wave by back-reflection of the grating laser therefore needs to be stabilised to less than $5 - 10\,\mathrm{nm}$, which can be achieved by interferometric readout of the relative positions and active feedback. In addition, the grating needs to be orthogonal to gravity by less than micro-radians due to the acceleration of the particles in the gravitational field [73].

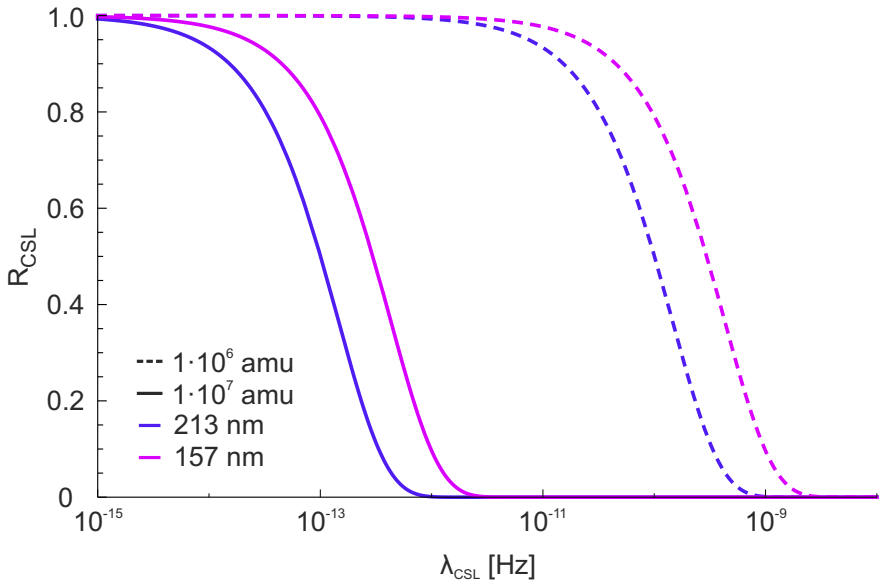

Figure 1.8: Reduction of the sinusoidal fringe visibility due to CSL-induced collapse for 10^6 amu (red) and 10^7 amu (blue) silicon nanoparticles with 157 nm (dashed) and 213 nm (solid) laser gratings, respectively. For $m = 10^7$ amu particles and $\lambda_{\text{grating}} = 213\,\text{nm}$ CSL localization rates down to λ_{CSL} less than $1 \times 10^{-13}\,\text{Hz}$ can be tested. We assume a characteristic length $r_{\text{C}} = 10^{-7}\,\text{m}$. The full excluded parameter space for 10^7 amu particles and 213 nm laser wavelength is shown in Figure 1.1.

Contrast reduction due to CSL

To experimentally test the CSL model as discussed in Section 1.2.2 we can calculate the reduction factor R_{CSL} of the sinusoidal fringe visibility due to spontaneous collapse of the wavefunction which is given by [37, 73, 96]

$$R_{\text{CSL}} = \exp\left[-\left(\frac{m}{1\,\text{amu}}\right)^2 \lambda_{\text{CSL}}\left[1 - \frac{\sqrt{\pi} r_{\text{C}} m D}{h t_2}\,\text{erf}\left(\frac{h t_2}{2 m D r_{\text{C}}}\right)\right](t_1 + t_2)\right]. \tag{1.14}$$

Figure 1.8 shows the sinusoidal fringe visibility for interferometry with 10^6 and 10^7 amu silicon nanoparticles with $\lambda_{\text{grating}} = 157\,\text{nm}$ and 213 nm. Assuming a critical length $r_{\text{C}} = 100\,\text{nm}$, as proposed in the original GRW model, localization rates λ_{CSL} of the CSL model down to $10^{-13}\,\text{Hz}$ can be excluded by observing sinusoidal interference contrasts of more than 50% of the theoretically expected value at a nanoparticle mass of 10^7 amu and a grating wavelength of 213 nm. This would shift current bounds set by matter-wave interferometry [28] by more than seven orders of magnitude. The entire excluded parameter space is shown in Figure 1.1.

In conclusion, a matter-wave interferometer for 10^7 amu silicon nanoparticles is proposed, which will exceed state of the art interferometry experiments [28] by three orders of magnitude and will be capable of probing hitherto unexplored regions in

parameter space for the CSL model. It can be associated with a macroscopicity value of $\mu_{\mathrm{macro}} > 20$ [44], which would exceed that of present-day interferometry ($\mu_{\mathrm{macro,KDTLI}} = 12$) [28] and be comparable with other proposals involving quantum superpositions of a mirror [97]. These bounds may be shifted even further by employing a fountain-like interferometer scheme, reaching masses of up to 10^8 amu. In addition, it is proposed that superposition experiments with massive objects can also be used to measure extremely soft collision with dark matter [98].

In the proposed experiment decoherence poses challenging but feasible experimental requirements. For reasons of laser stability, available optical pulse energies, and coherence times, but also to prevent decoherence due to scattering of laser photons, a grating wavelength of $\lambda_{\mathrm{grating}} = 213\,\mathrm{nm}$ will be the best choice. Lasers with sufficient power stability at this wavelength can be obtained from the 5^{th} harmonic of an Nd:YAG. For the proposed grating phases, optical pulse energies of less than $300\,\mu\mathrm{J}$ will be sufficient. Reaching pressures of down to $10^{-12}\,\mathrm{mbar}$ and keeping the interferometer at sub-10 nm position, and sub-μrad angular stability will be the most demanding experimental challenge. To realise sufficient spatial coherence in the source will require optical cooling of 25 nm diameter silicon particles in low mode-volume optical cavities (see Section 3.2). For non-isotropic particles additional control and cooling of the rotational degrees of freedom will be necessary (see Chapters 2, 3, and 4) to avoid orientation dependent decoherence sources [99].

Since all the particles contributing to the interference pattern have to originate from the same cavity anti-node, additional methods will have to be implemented, in order to reproducibly deliver the particles into the cavity and to detect their position. Future improved cooling schemes (see Section 3.1.2) will be capable of cooling particles to below 50 mK in a few milliseconds, thereby avoiding internal heating of the nanoparticles. Dropping the particles from this well-localised source will ensure the forward velocity to be spread out by approximately 0.5%, thereby preventing the smearing of the interference pattern due to a lack of longitudinal coherence or the influence of coriolis forces [100]. The velocity selection could be improved further by applying stronger radial cooling or employing time-of-flight resolving detection or selection methods [101].

2 Launching, tracking and manipulating nanoparticles in high vacuum

2.1 Nanoparticle launching

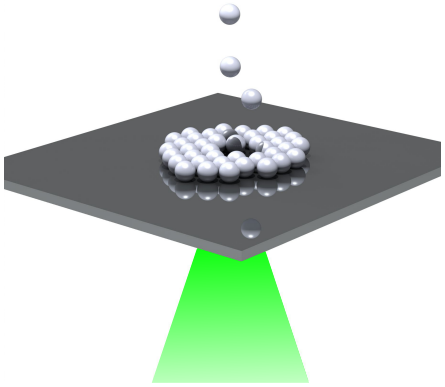

Figure 2.1: Basic working principle of laser-induced acoustic desorption (LIAD) of nanoparticles into vacuum. A focussed laser pulse (wavelength 532 nm, pulse length 6 ns, and pulse energy 1-10 mJ) hits the back-side of a substrate. Ablation and deformation of the substrate material lead to acoustic shock-waves which shake off the nanoparticles at the front side.

Developing a reliable source of clean, neutral, slow, size- and shape-selected particles which operates at ultra-high vacuum (UHV) conditions is the first crucial step for cavity-cooling, matter-wave interferometry and levitated optomechanics experiments. In this chapter I will present volatilisation methods for various nanoparticle types and shapes, such as silica nanospheres and nanofabricated silicon particles. Furthermore, I will discuss their interaction with light fields in terms of scattering, optical forces and torques.

Whilst at modest vacuum conditions above millibar pressures the motional energy of a particle can be dissipated by the surrounding gas, free flight experiments in high vacuum require a soft launch mechanism to achieve long interaction times of a cavity field or interferometer with the particle (see Chapters 1 and 3). Nanoparticles can be trapped in an optical tweezer in a buffer gas environment and transferred into high vacuum while their motion is cooled with active feedback either in free space [87] or

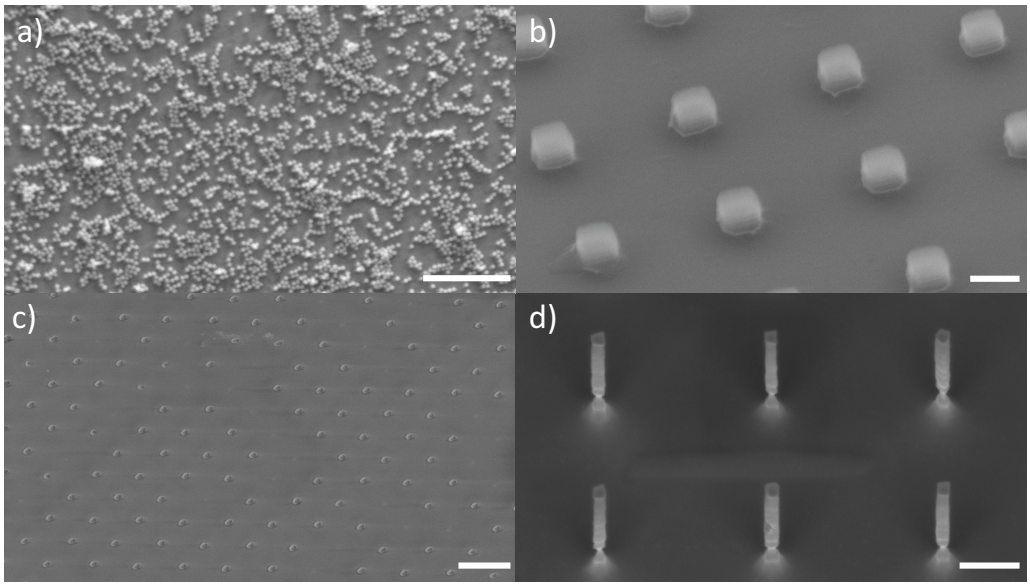

Figure 2.2: Library of particles tested in our experiments. a) Commercial silica particles (diameter 300 nm) spin-coated onto a 300 μm thick aluminium foil. b) Silicon cubes (edge length 300 nm) etched into a silicon on insulator (SOI) wafer with an expected break-off point at the silicon to insulator boundary. c) Spherical silicon particles patterned and deposited onto a silicon wafer via nanodicing [103]. d) Silicon nanorods etched into a silicon wafer with a pre-defined point of rupture [104]. Scale bars: a) 5 μm, b) 400 nm, c) 2 μm, and d) 400 nm.

inside a hollow-core fiber [102] (see Chapter 3). To avoid differential pumping stages and achieve faster duty cycles we are developing sources of nanoparticles which can be operated directly in UHV. For many of these techniques we rely on tailor-made nanoparticles and substrates which are nano-fabricated by our collaboration partners Alon Kosloff and Fernando Patolsky at Tel Aviv University, Israel.

Dielectric nanoparticles of various materials, sizes and shapes can be coated onto a supporting foil, e.g. aluminium, silicon or titanium, or nanofabricated into the substrate itself, see Fig. 2.2. To volatilize them in vacuum one has to overcome the van der Waals potential between the particles and the substrate, or the binding energy of the material. Irradiation of the rear side of the sample with a focussed pulsed laser (spot size of $\sim 50\,\mu$m, a wavelength of 532 nm, where the substrates absorb the laser pulses, and pulse energies of a few milliJoules) causes ablation and deformation of the material. The resulting acoustic shock-waves in the substrate lead to accelerations of the particles which are high enough to overcome the binding potential and lift them into vacuum[105]. This laser induced acoustic desorption (LIAD) technique has previously been used to desorb organic and biomolecular ions [106–109], and single bioparticles [110]. At even higher pulse energies the front surface of the substrate itself can be cracked and fragments of various sizes and shapes can be launched [111].

The volatilization of spherical and rod-shaped particles is shown in Figure 2.3. Spherical particles with diameters ranging from 400 nm down to 30 nm, and rod-shaped particles with lengths between 600-1300 nm and diameters of 60-120 nm, are launched into vacuum and recollected on a sample plate, where they can be observed using an SEM or AFM. Larger spheres with diameters around 300 nm and nanorods with masses on the order of 10^{10} amu are suitable for demonstrations of cavity cooling [111, 112], optical trapping in a tweezer [113] and rotational optomechanics [104, 114]. Smaller particles with diameters below 30 nm will be required for cavity cooling in small mode-volume cavities (see Chapter 3) and earth-based free flight matter-wave interferometry, which is conceivable for masses between 10^6 and 10^7 amu (see Chapter 1). To influence the velocity distribution of charged particles we can apply an electric field between the sample substrate and the cavity block or otherwise connect both to common ground (see Appendix Figure B.1).

2.2 Nanoparticle detection

To characterize and optimize the various nanoparticle launch techniques we utilize the strongly pumped (300 W intra-cavity power) field of a high-finesse optical cavity at $\lambda = 1550$ nm to measure the velocity distribution of the nanoparticles. A single particle flying through the cavity mode scatters a portion of the cavity light into free space. The intensity depends on the particle's x- and z-position within the cavity mode. For non-spherical particles the scattering intensity in the direction of the detector additionally depends on the orientation of the particle with respect to both the k-vector and the axis of polarisation of the cavity field (see Publications 2.4 and 3.5). To detect the scattered light we place the bare, polished end of a 1 mm diameter optical fiber (Thorlabs FP1000ERT) close to the cavity mode, orthogonal to both the cavity axis and the polarisation vector of the light field. We focus the rear fiber end onto a fast, amplified InGaAs detector using a droplet of fiber connector epoxy (Thorlabs F112), as described in References [89, 104, 113].

For low mode-volume microcavities, as discussed in Publication 3.4, with large linewidths, the nanoparticle motion can also be detected via the frequency shift imprinted by the dielectric particle onto the cavity mode (see Chapter 3). This shift can be seen as an intensity modulation of the light transmitted through the cavity. In the following I will discuss the scattering behaviour of spherical and elongated particles in a linearly polarised standing light wave.

2.2.1 Silica nanospheres

When interacting with a light field at $\lambda = 1550$ nm, silica nanoparticles with diameters smaller than 400 nm can be considered as point particles in the Rayleigh approxima-

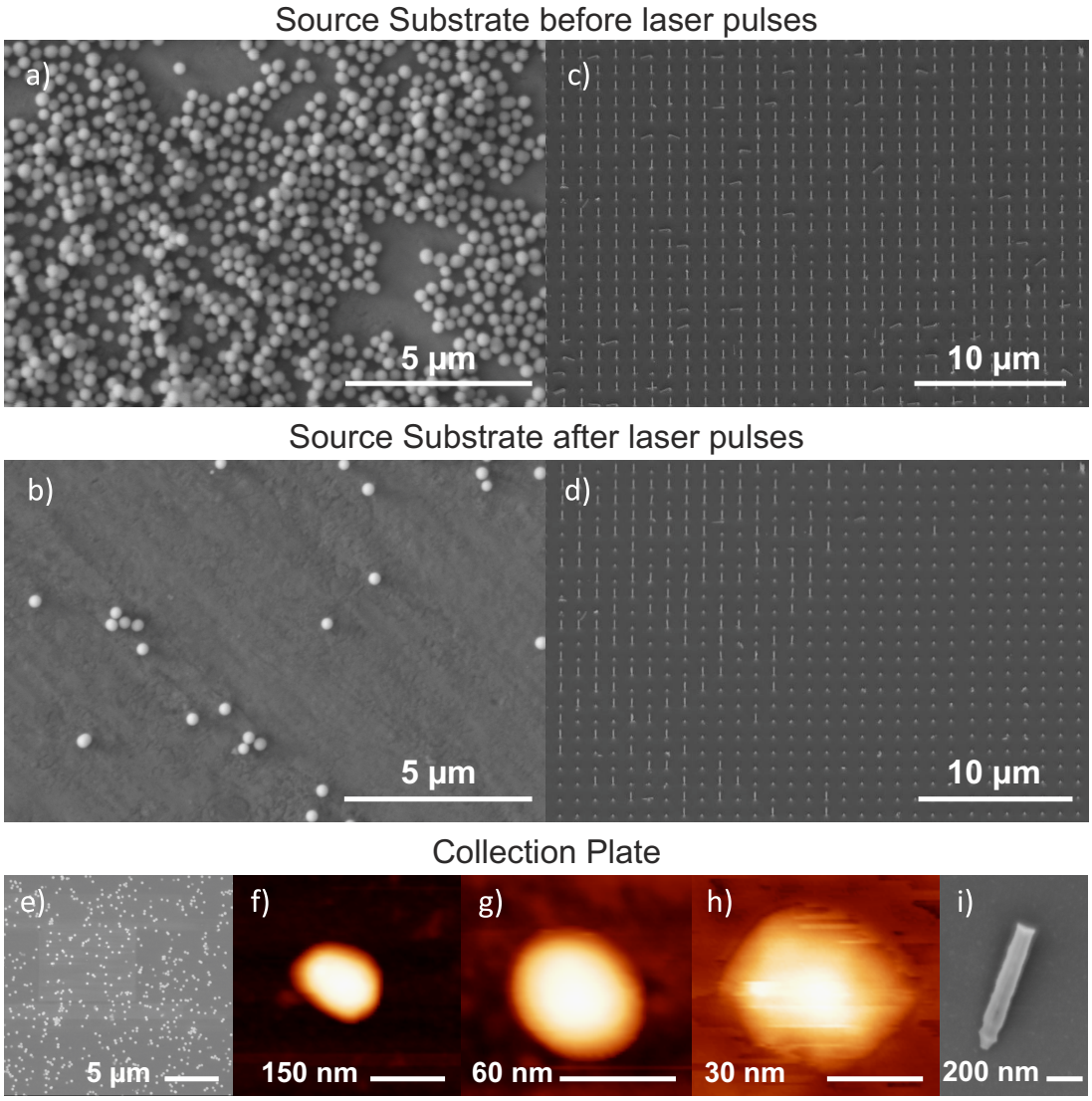

Figure 2.3: Launching of spherical and rod-shaped nanoparticles with masses ranging from 10^7 to 10^{10} amu. a) An aluminium foil of 300 μm is spin-coated with commercially available 300 nm silica nanospheres (Bangs Laboratories). b) After LIAD a substantial amount of nanoparticles is removed. c) The same sample spot of etched silicon nanorods on a 500 μm thick wafer before and d) after LIAD reveals the efficient break-off of the rods. The nanospheres with diameters of 300 nm (e), 150 nm (f), 60 nm (g), and 30 nm (h) as well as the silicon nanorods (i) can be re-collected on a silicon sample plate, a few centimeters away from the source, and observed under a scanning electron microscope (e & i) or using an atomic force microscope (f-h).

tion and their scattering is dominated by the dipole contribution [68, 115, 116]. The normalised scattering intensity in direction orthogonal to both the cavity axis and the polarisation vector is given by [111]

$$S_{\mathrm{N}}(t) = \cos^2\left(kz\left(t\right)\right) \exp\left(-2x\left(t\right)^2 / w_0^2\right), \tag{2.1}$$

with wavenumber $k = 2\pi/\lambda$ and mode waist radius w_0, and is experimentally obtained by normalising the ratio of detected scattering and transmitted cavity intensity [89]. It consists of two distinct features: A Gaussian envelope due to the particle crossing the cavity mode in forward direction along x and a periodic modulation caused by the particle running over the cavity's standing light wave along z.

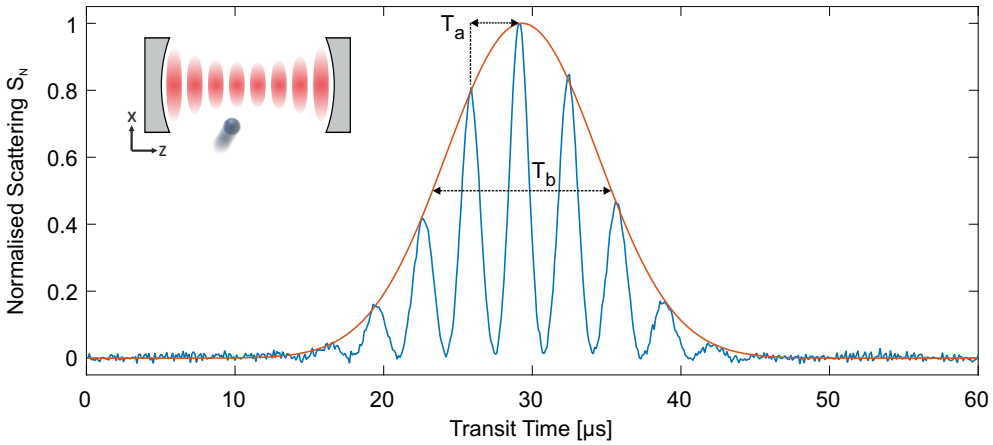

Figure 2.4: Normalised scattering signal (blue, according to Equation 2.1) for a single 300 nm SiO2 particle in transit through a $w_0 = 57\,\mu$m cavity in high vacuum. By fitting the envelope of the scattering signal with a Gaussian (orange curve) we measure a forward velocity $v_x = 5.6 \pm 0.2\,$m/s and from the period (averaged over the whole transit) of the sinusoidal modulation we determine a transverse velocity of $v_z = 0.24 \pm 0.01\,$m/s

A typical scattering signal of a fast particle transiting the cavity mode is shown in Figure 2.4. As the particle's kinetic energy is much larger than the optical potential, its velocity can be considered constant during the transit. From the $1/\mathrm{e}^2$ width T_b of the fitted Gaussian envelope we determine the forward velocity of the particle $v_x = w_0/T_\mathrm{b}$. The transverse velocity is determined from the time difference T_a between the scattering maxima via $v_z = \lambda/2T_\mathrm{a}$. The high intra-cavity intensity results in a high signal to noise of the scattered light. We can measure the particle velocity under various source conditions and test their suitability for cavity cooling and matter-wave interferometry. The detailed results are discussed in Appendix B.1. The slowest particle velocities have been achieved using 200 nm thick aluminium substrates. To protect the mirrors from deposition of charged nanoparticles we apply a potential difference of -200 V between the cavity block and the sample surface.

2.2.2 Nanodiced silicon

Both for cooling and for matter-wave experiments it is favourable to use silicon rather than silica nanoparticles. At a wavelength of 1550 nm silicon exhibits a polarizability to mass ratio which is 2.5 times higher than for silica, resulting in 1.5 times higher optical forces. In addition, a work function of 4.5 eV in silicon allows to realise single photon ionisation gratings (see Chapter 1) [25]. Mono-disperse silicon nanoparticles are not yet available commercially in the desired diameter-range of $20 - 300$ nm. However, nanofabrication of silicon has been perfected in the last decade [117].

The group of Fernando Patolsky at Tel Aviv University (TAU) has developed a method to produce arrays of silicon nanoparticles with well defined sizes, which allows them to position the particles on arbitrary surfaces [103]. In brief, an array of silicon nanorods is etched into a silicon wafer and filled with an epoxy resin. In the next step, slices of the desired thickness are cut using an ultramicrotome, resulting in arrays of particles with well defined geometries, which are embedded in the thin epoxy lamellas. Those slices are then put onto an arbitrary surface, where the polymer can be removed using an oxygen plasma, leaving equally spaced tailored particles on the substrate (see Figure 2.2c). We place those substrates in high vacuum underneath the optical cavity and launch the silicon particles using LIAD. Their velocity distributions (see Appendix B.2) resemble those of the silica nanoparticles. However, a shift of the velocity distribution in an electric field indicates that a higher fraction of the launched silicon particles is charged, compared to silica. This may be explained by charge deposition during the exposure to the oxygen plasma.

2.2.3 Silicon nanorods

The TAU team has provided us with tailored and pristine silicon nanoparticles of various sizes and shapes. In particular, elongated silicon particles can be produced in a series of time-multiplexed reactive ion etching steps [104], forming an array of silicon nanorods standing on a silicon wafer with a spacing of $1\,\mu m$, as shown in Figure 2.2d. Anisotropic etching of the nanorod base in a Bosch process results in small kerfs, which serve as break-off points in the launching process (see Publication 2.4).

Using LIAD we can reproducibly break off the nanorods at pulse energies of a few milliJoule. Figure 2.3c and d show the same sample spot before and after launching some of the rods with a single laser pulse. A typical launched and re-captured rod is presented in Figure 2.3i, showing the break-off at the desired rupture point. In this way, we can reproducibly launch well defined rod-shaped particles through a high finesse optical cavity in UHV (see Publication 2.4) or reliably load an optical dipole trap at millibar gas pressures, where the rods can be stably levitated for more than 100 days (see Chapter 4 and Publications 4.1 and 4.2).

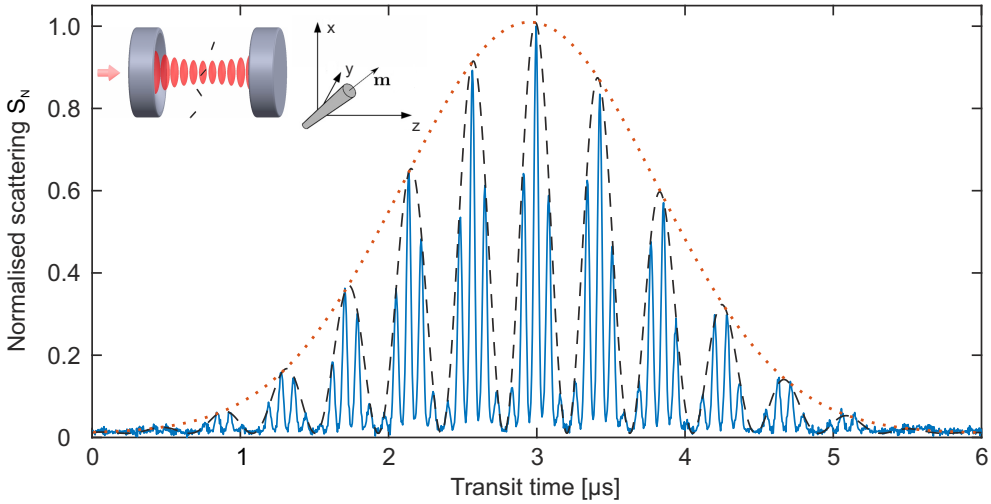

Figure 2.5: Normalised scattering intensity for a nanorod passing through a strongly pumped high-finesse cavity field polarised along x in UHV. Its forward (orange dotted Gaussian envelope) and transverse velocity (black, dashed envelope) can be determined as discussed in the case of spheres in section 2.2.1. The rod rotation (fast modulation) can be deduced from the time-resolved signal via Equation 2.2, as explained in Publication 2.4.

During the launch process, mechanical strain in the nanorod base is released and the LIAD shock waves add energy to both the forward and the rotational motion of the rod. In high vacuum there is no damping by residual gas and the rods can move and rotate freely. By launching them through a high finesse optical cavity, and monitoring the light they scatter in the direction orthogonal to both the cavity axis and the axis of polarisation, we can track the dynamics of each individual rod transiting the field. The scattering amplitude depends again on the rod's center of mass position within the Gaussian cavity field of waist w_0, as in the case of spherical particles (see Section 2.2.1). In addition the scattering amplitude depends on the orientation of the rod with respect to the axis of polarisation and direction of propagation of the light field. For a rod of length L and radius a at the position (x, y, z), pointing in direction $\mathbf{m}$ in an optical field which propagates along $\mathbf{e}_z$, and is polarised along $\mathbf{e}_x$, the scattered light intensity I_{sca} in direction $\mathbf{n}$ in the far field is proportional to

$$I_{\mathrm{sca}} \propto k^4 a^4 L^2 \left(\frac{\varepsilon_{\mathrm{r}} - 1}{\varepsilon_{\mathrm{r}} + 1}\right)^2 |\mathbf{n} \times \mathbf{u}_{\mathrm{int}}|^2 \left[S_+^2 + 2\cos(kz) S_+ S_- + S_-^2\right] e^{-2(x^2+y^2)/w_0^2}, \quad (2.2)$$

with $S_\pm = \mathrm{sinc}\left[\mathbf{m} \cdot (\mathbf{e}_z \pm \mathbf{n}) kL/2\right]$ and the electric field within the nanorod $\mathbf{u}_{\mathrm{int}} = 2\mathbf{e}_x + (\varepsilon_{\mathrm{r}} - 1)(\mathbf{m} \cdot \mathbf{e}_x)\mathbf{m}$.

For the direction of observation $\mathbf{n} = \mathbf{e}_y$ realised in our experiments, the scattered light intensity will therefore always be modulated by the particles' center of mass motion through the standing light wave and Gaussian beam waist, and their rotation. Only in

the case of a particle rotating in the plane orthogonal to the axis of polarisation of the light field there is no modulation due to rotation. Equation 2.2 holds in the Rayleigh-Gans approximation for thin needles for which the particle length exceeds its radius ($L \gg a$) and for which the radius is small compared to the wavelength ($nka \ll 1$) [118].

In Figure 2.5 we show a typical scattering signal for a rod with $L = (780 \pm 14)\,\mathrm{nm}$ and $a = (65.5 \pm 5.5)\,\mathrm{nm}$, rotating at an angular frequency of $\omega_{\mathrm{rot}} = 2\pi \times 5.9\,\mathrm{MHz}$. We observe the Gaussian and sinusoidal envelopes of the scattering, attributed to the particle transiting the cavity field in forward direction and moving over the standing light wave. On top of that, there is a high-frequency modulation of the scattered intensity which is caused by the rotation of the rod, as given in Equation 2.2. We can determine the particle velocities and rotation rates for different samples and various break-off conditions by analysing the spectrum of the time resolved scattering signal. A more detailed explanation of the experiment can be found in Publication 2.4. By changing the etching parameters in the nanorod fabrication process, one can alter the ratio between the kerf and nanorod diameter. A list of all rod parameters is given in Appendix Table C.1. Figure 2.6 shows that the mean rotation energy of the nanorods, $E_{\mathrm{rot}} = I\omega_{\mathrm{rot}}^2/2$, with the moment of inertia $I = mL^2/12$, can be reduced by lowering the ratio between kerf and rod diameter. The mean forward velocities and rotation energies for the different nanorod samples are listed in Appendix Table C.2.

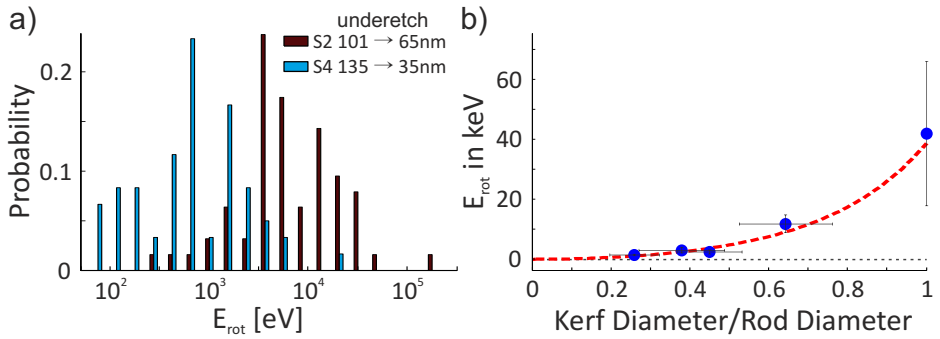

Figure 2.6: Reduction of the rotation energies by variation of the ratio between kerf and nanorod diameter. a) Distribution of rotation rates after launching with identical pulse-laser parameters for samples S2 and S4, which exhibit two different underetching ratios (see Appendix Table C.1). b) Dependency of the mean rotation energies on the kerf to diameter ratio. The mean rotation energy can be reduced by stronger underetching. An exponential fit (red, dashed curve) serves as a guide to the eye. The errorbars are given by the standard deviation of the energy distributions and the uncertainty of the rod lengths after break-off. For underetched nanorods this uncertainty is substantially smaller than for those which do not have a pre-defined point of rupture.

2.3 Optical forces and torques

2.3.1 Optical forces

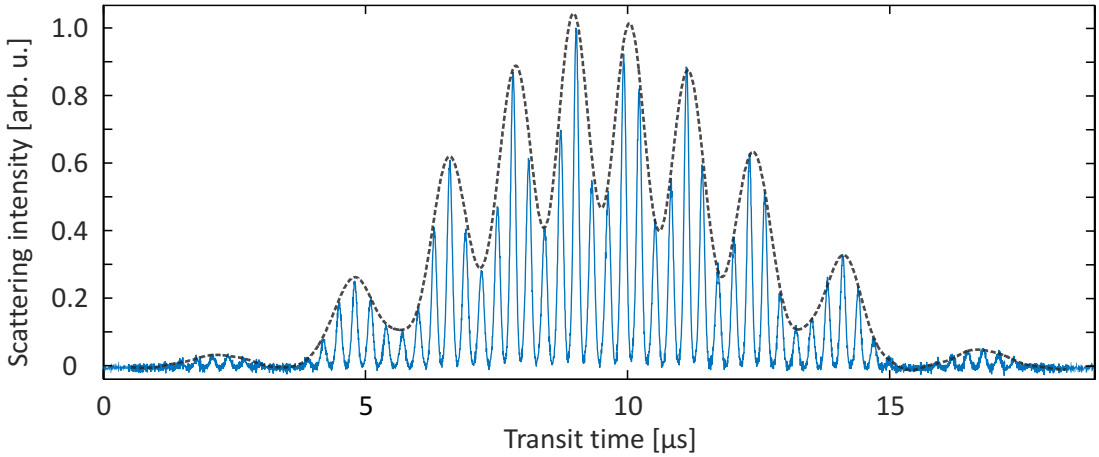

Figure 2.7: Scattering signal from a nanorod transiting the cavity beam, which gets one-dimensionally channelled in the standing light wave. Contrary to the rod displayed in Figure 2.5, around the center of the cavity mode, the envelope of the scattered light (black, dashed line) does not drop to zero anymore, due to the onset of channelling. From the maximum axial trapping frequency the interaction strength between the particle and the cavity field can be determined, as discussed in Publication 2.4.

In an optical field, which is far off-resonant with respect to all internal transitions, the forces acting on a dielectric particle with static polarizability α result from the induced dipole moment $\mathbf{d} = \alpha\mathbf{E}$ in the electric field $\mathbf{E}$ and the time-averaged dipole force $\mathbf{F}(\mathbf{r}) = \alpha\nabla\left|\mathbf{E}(\mathbf{r})\right|^2/4$. Therefore, in a standing light wave Gaussian beam there is a force in the radial direction r associated with the field gradient along the beam waist, and an axial force associated with the gradient along the standing wave in z-direction. Under the right experimental conditions, these forces can lead to axial and/or radial harmonic confinement of a particle (see Chapters 3 and 4). The stiffness of this confinement in both cases can be quantified via the resulting trapping angular frequencies ω_r and ω_z, which depend on the polarizability-to-mass ratio α/m of the particle and the intensity of the light field I_0. They are given by [119]

$$\omega_r = \sqrt{\frac{8\alpha I_0}{m\varepsilon_0 c w_0^2}} \quad \text{and} \quad \omega_z = \sqrt{\frac{4\alpha I_0 k^2}{m\varepsilon_0 c}}. \tag{2.3}$$

For spheres the polarizability is a scalar, which can be determined from the Clausius-Mossotti relation $\alpha = 4\pi\varepsilon_0 R^3(\varepsilon_\mathrm{r}-1)/(\varepsilon_\mathrm{r}+2)$ [120, 121]. For anisotropic particles the polarizability, in general, takes the form of a tensor, and their interaction with

a light field thus depends on their orientation with respect to the field [122]. The polarizability of a rod-shaped particle is maximal when its long axis is aligned along the axis of polarisation, taking a value of $\alpha_{\parallel} = a^2\pi L\varepsilon_0(\varepsilon_\mathrm{r} - 1)$. It is minimal for a rod pointing orthogonal to the axis of polarisation, resulting in $\alpha_{\perp} = a^2\pi L\varepsilon_0 2(\varepsilon_\mathrm{r} - 1)/(\varepsilon_\mathrm{r} + 1)$. Averaged over all rotation axes, the polarizability reads $(\alpha_{\parallel} + 2\alpha_{\perp})/3$, and for a rod rotating in a plane orthogonal to the beam axis it is given by $(\alpha_{\parallel} + \alpha_{\perp})/2$. The high relative permittivity of silicon at telecom wavelengths ($\varepsilon_\mathrm{r} \simeq 12$) results in a significant shape-enhanced polarisability for the nanorods, with $\alpha_{\parallel}$ almost five times larger compared to a sphere of same volume. Even when averaged over all rotation axes, the rods' polarizability is two times higher than in the case of a sphere. As discussed in Publications 2.4 and 3.5, this leads to stronger interactions between the particles and the light field, which can be exploited in nanoparticle cooling and matter-wave interferometry experiments. Figure 2.7 shows the scattering from a rotating rod channelled along one anti-node of the cavity field, revealing the enhanced optical forces as discussed in Publication 2.4.

2.3.2 Optical torques

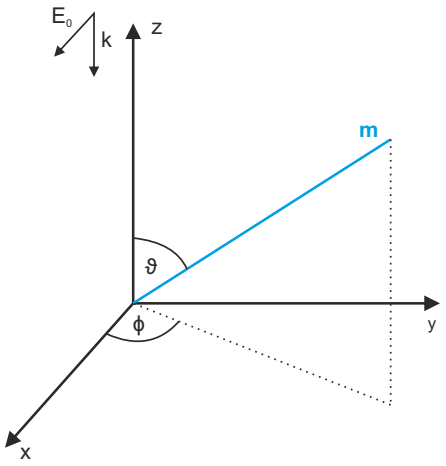

Figure 2.8: Euler angles in the $z - y' - z''$ convention. The orientation $\mathbf{m}$ of the rod with respect to the beam propagation axis along z and the field polarisation along x is determined by the angles (ϕ, ϑ).

As all dielectric particles which exhibit an off-resonant index of refraction higher than their surrounding medium, silicon nanoparticles behave as high-field seekers. Thin nanorods with a length comparable to half the wavelength do not only tend to be attracted towards the center of the anti-nodes of a standing light wave, they also align along the axis of polarisation where their polarizability reaches its maximal value. In a light field linearly polarised along x, with amplitude E_0 and direction of propagation

in z-direction, the resulting dipole torque is given by [123]

$$\begin{aligned}\mathbf{N} = &-\frac{kLE_0^2}{8}\cos(2kz)j_1(kL\cos\vartheta)\left(\alpha_\perp + \Delta\alpha\cos^2\phi\sin^2\vartheta\right)(\mathbf{m}\times\mathbf{e}_z)\\ &+\frac{\Delta\alpha E_0^2}{2}\cos\phi\sin\vartheta\left(\frac{1}{2}+\frac{1}{2}\cos(2kz)\mathrm{sinc}(kL\cos\vartheta)\right)(\mathbf{m}\times\mathbf{e}_x)\,,\end{aligned} \tag{2.4}$$

where (ϕ, ϑ) specify the rod's orientation $\mathbf{m}$ (see Figure 2.8), $\Delta\alpha = \alpha_\parallel - \alpha_\perp$, and j_1 the first order spherical Bessel function. As mentioned before, the torque vanishes for the rod pointing along the axis of polarisation ($\mathbf{m} = \mathbf{e}_x$; $\phi = 0, \vartheta = \pi/2$). In addition, there is an unstable equilibrium at which the torque vanishes in case the rod is pointing in the direction orthogonal to both the beam and polarisation axis ($\mathbf{m} = \mathbf{e}_y$; $\phi = \vartheta = \pi/2$) or along the beam axis ($\mathbf{m} = \mathbf{e}_z$; $\vartheta = 0$). For rods whose length exceeds the wavelength of the light field, the second term in the expression for the torque can become dominant. Such long rods would therefore tend to align along the beam axis.

As presented in Publication 2.4, this torque can influence the rotation of a nanorod during its transit through an intense standing light wave. In Chapter 3 and 4 we will discuss how optical forces and torques can be used to cool and confine the rotational motion of a rod.

2.4 Reprint: Cavity-Assisted Manipulation of Freely Rotating Silicon Nanorods in High Vacuum

S. Kuhn et al., "Cavity-Assisted Manipulation of Freely Rotating Silicon Nanorods in High Vacuum," Nano Letters 15(8),5604-5608 (2015), reports on the detection and manipulation of freely rotating silicon nanorods in high vacuum, using the intense field of a high-finesse optical cavity. The process of nanoparticle fabrication, laser-pulse induced launching, detection of rotation via a modulation of scattering intensity, shape-enhancement of the nanoparticle polarizability and optical torques influencing the particle rotation are discussed.

As the leading author I conceived the experiment together with M. Arndt and P. Asenbaum, took all relevant measurements together with P. Asenbaum, performed the data analysis together with B. A. Stickler and S. Nimmrichter and wrote the paper together with P. Asenbaum, B. A. Stickler, S. Nimmrichter, K. Hornberger and M. Arndt. The nanoparticle fabrication was carried out at Tel Aviv University by A. Kosloff, O. Cheshnovsky and F. Patolsky in correspondence with M. Sclafani. The scattering theory was developed by B. A. Stickler, S. Nimmrichter and K. Hornberger at the University of Duisburg-Essen.

NANO LETTERS

Letter

pubs.acs.org/NanoLett

Cavity-Assisted Manipulation of Freely Rotating Silicon Nanorods in High Vacuum

Stefan Kuhn,[†] Peter Asenbaum,[†] Alon Kosloff,[‡] Michele Sclafani,[†,∥] Benjamin A. Stickler,[§] Stefan Nimmrichter,[§] Klaus Hornberger,[§] Ori Cheshnovsky,[‡] Fernando Patolsky,[‡] and Markus Arndt*[,†]

[†]University of Vienna, Faculty of Physics, VCQ, Boltzmanngasse 5, 1090 Vienna, Austria

[‡]School of Chemistry, Tel-Aviv University, Ramat-Aviv 69978, Israel

[§]University of Duisburg-Essen, Lotharstraße 1, 47048 Duisburg, Germany

S *Supporting Information*

ABSTRACT: Optical control of nanoscale objects has recently developed into a thriving field of research with far-reaching promises for precision measurements, fundamental quantum physics and studies on single-particle thermodynamics. Here, we demonstrate the optical manipulation of silicon nanorods in high vacuum. Initially, we sculpture these particles into a silicon substrate with a tailored geometry to facilitate their launch into high vacuum by laser-induced mechanical cleavage. We manipulate and trace their center-of-mass and rotational motion through the interaction with an intense intracavity field. Our experiments show that the anisotropy of the nanorotors leads to optical forces that are three times stronger than on silicon nanospheres of the same mass. The optical torque experienced by the spinning rods will enable cooling of the rotational motion and torsional optomechanics in a dissipation-free environment.

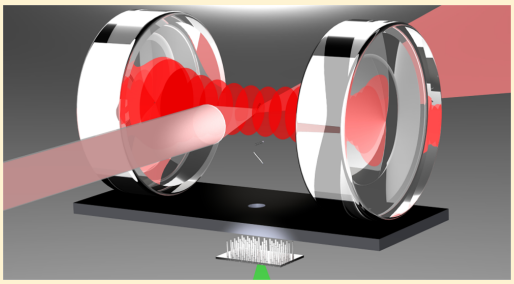

KEYWORDS: *Nanoparticle launching, nanoparticle detection, silicon nanorods, cavity optomechanics*

Nanoparticles often exhibit unique optical, mechanical, or electromagnetic properties because of quantum effects in confined geometries and low dimensions.[1] Complementary to that, our present study is part of a long-term effort to control the quantum properties of the objects' motion.[2−4] First experiments demonstrating de Broglie wave optics with macromolecules[5] were triggered by the question whether the superposition principle of quantum mechanics holds on all scales. They have led to the observation of quantum interference with masses beyond 10 000 amu.[6] An even higher mass regime, which might give insight into the quantum-classical transition, can be reached with novel coherent manipulation schemes.[7] Models of a spontaneous localization of the wave function,[8] and nonstandard effects of gravity,[9,10] will become relevant for delocalized particles in the mass range of 10^5−10^8 amu, and above 10^{10} amu, respectively. Tests of such models will require neutral, size- and shape-selected, cold, and slow nanoparticles that are mechanically isolated from their environment. This has motivated new experiments to launch and cool dielectric nanospheres in optical tweezers,[11−13] in ion traps,[14] and in free-flight.[15]

Here, we extend this research to rod-shaped dielectrics of tailored geometry and anisotropic polarizability. Once their rotational motion can be controlled sufficiently well, these nanorods may be suitable for realizing torsional optomechanics.[16−18] Earlier experiments have shown that optomechanical torques can be exerted on nanorods in solution using the polarization or orbital angular momentum of a light field.[19−22] The manipulation of nanoparticles in a dissipation-free environment, however, has remained challenging.[23] The coupling between rotational and motional degrees of freedom was recently demonstrated with optically trapped birefringent microspheres in a low pressure environment.[24]

We have prepared periodic arrays consisting of more than a million silicon nanorods per square millimeter by dry-etching crystalline silicon wafers (see Methods and Materials). A scanning electron microscopy image of such an array is displayed in Figure 1A. The individual nanorods exhibit a length of 795 ± 17 nm and a diameter of 108 ± 16 nm corresponding to a mass of $(1.0 \pm 0.3) \times 10^{10}$ amu. The sample was positioned in a chamber evacuated to 10^{-6} Pa underneath an optical cavity. The backside of the sample was locally heated by a pulsed laser beam (1−3 mJ pulse energy, 6 ns duration and 532 nm wavelength) focused to 100 μm, which desorbs the rods by laser-induced thermomechanical stress (LITHMOS).[15] After launch, the freely moving and rotating rods need to pass a

Received: June 10, 2015
Revised: July 4, 2015
Published: July 13, 2015

DOI: 10.1021/acs.nanolett.5b02302
Nano Lett. 2015, 15, 5604−5608

Nano Letters Letter

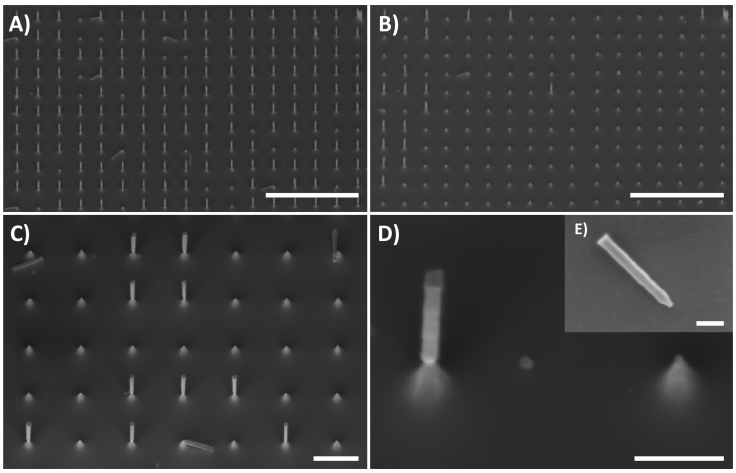

Figure 1. SEM micrographs of the nanosculptured silicon rods. Array of nanorods with underetched kerfs (A) before and (B) after LITHMOS desorption. (C and D) The kerfs define the break points where the rods crack. The actual rod length appears shortened under the oblique viewing angle. Nanorods with well-defined geometries can be launched, sent through the cavity and collected on a sample plate (E). Scale bars: (A and B) 5 μm, (C) 1 μm, (D) 400 nm, and (E) 200 nm.

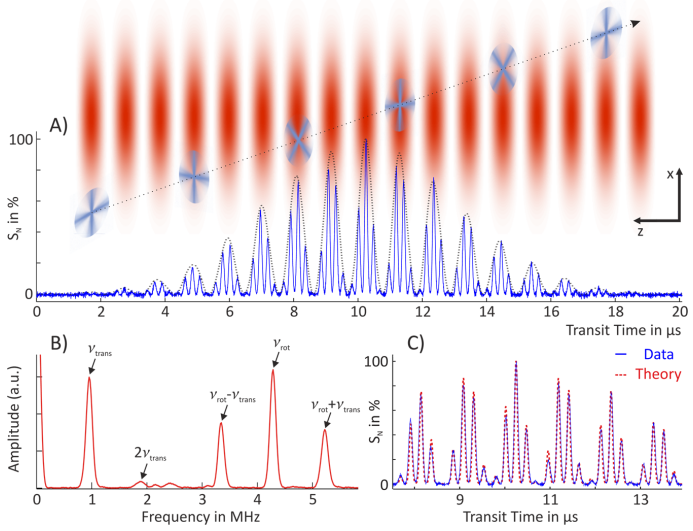

Figure 2. Tracing the nanorotor kinematics. The motion of every single nanorod can be deduced from the light it scatters while passing the cavity. (A) The signal as a function of time conveys three distinct time scales corresponding to (i) the vertical transit through the cavity mode (Gaussian envelope), (ii) the transverse motion across the standing wave (black dotted line, low frequency ν_{trans}), and (iii) the nanorod rotation (high frequency ν_{rot}). (B) These frequency contributions can also be identified in the Fourier spectrum of the signal. The particle displayed here exhibits the vertical velocity v_x = 11.5 ± 0.5 m/s, the on-axis velocity v_z = 0.77 ± 0.05 m/s and the rotation rate f_{rot} = 2.15 ± 0.03 MHz. The geometric collimation of the incident particle trajectories permits an unambiguous distinction of the translational and rotational motion. (C) The measured scattering signal (blue solid line) is well explained by a simple theoretical model (red dashed line), see Methods and Materials and Supporting Information.

500 μm diameter and 4 mm long aperture before entering a strongly pumped high-finesse infrared cavity (λ = 1560 nm, 400 W intracavity power, 330 000 finesse, w_0 = 65 μm waist). The rotation rates differ from shot to shot ranging from 550 kHz up to 30 MHz; the forward velocities vary between 3 and 78 m/s. Small kerfs etched into the nanorod base define the desired break-off conditions (see Figure 1C and D; details in the Methods and Materials). In Figure 1A and B, we show an electron micrograph of a sample spot before and after the LITHMOS pulses. It demonstrates that the rods can be

DOI: 10.1021/acs.nanolett.5b02302
Nano Lett. 2015, 15, 5604−5608

reproducibly broken off at the tailored constrictions. Figure 1E depicts a close-up of the etched conical tip of a rod after launch and recapture.

The standing light wave field of a high-finesse cavity allows us to track the translational and rotational motion of the particles. It is optically pumped by a linearly polarized, distributed-feedback laser locked close to the cavity resonance. At the laser wavelength of 1560 nm, silicon exhibits a high relative permittivity ($\varepsilon_r \simeq 12$) and minimal absorption. In a homogeneous field, the polarizability assumes a maximum value of $\alpha_\parallel/(4\pi\varepsilon_0) = 6.4 \times 10^9$ Å^3 and a minimum value of $\alpha_\perp/(4\pi\varepsilon_0) = 9.8 \times 10^8$ Å^3 when the rods are oriented parallel and perpendicular to the field, respectively.[25] Even for rotating rods, the polarizability averaged over all possible rotation axes, $((1/3)\alpha_\parallel + (2/3)\alpha_\perp)/(4\pi\varepsilon_0) = 2.8 \times 10^9$ Å^3, is larger than for a silicon nanosphere of the same mass, $\alpha_{sph}/(4\pi\varepsilon_0) = 1.4 \times 10^9$ Å^3.

We can trace each nanorotor using the light it scatters into the direction perpendicular to both the cavity axis and the field polarization. We collect this light in a 1 mm multimode fiber placed at a distance of 200 μm from the cavity center. The detected intensity depends on the rod's position in the standing wave and also on its orientation (see Methods and Materials).

When a symmetric rotor enters the cavity and moves freely along the cavity axis, we expect a modulation of the scattering signal at two distinct frequencies: One is the translational frequency $\nu_{trans} = 2v_z/\lambda$ of the particle passing the standing-wave nodes with velocity v_z, the second one is twice the rotation frequency, $\nu_{rot} = 2f_{rot}$.

Figure 2A displays the normalized scattering intensity of a freely rotating nanorod, $S_N \equiv (I_S/I_C)/\max(I_S/I_C)$, where I_S is the measured scattering signal and I_C the simultaneously recorded intracavity intensity. Panel C shows that it agrees well with the theoretical expectations for light scattering at dielectric needles (red dotted line). An expression for the expected scattering signal as a function of the rod's center-of-mass position and orientation is presented in the Methods and Materials. This signal is evaluated along the rotor trajectory. In the Supporting Information, we provide a full comparison between the measured signal in panel A and the model, simulating the trajectory with an appropriate choice of the initial conditions and the field amplitude. The corresponding Fourier spectrum, depicted in panel B, exhibits the distinct frequency contributions of translation and rotation.

For slow rods, we could observe cavity-induced translational channelling, that is, one-dimensional trapping along an antinode of the standing light wave. One such case is displayed in Figure 3, where the scattering signal (panel A) differs significantly from Figure 2. By low-pass filtering the scattering signal, we can eliminate the modulation due to the rotation of the rod. The resulting modulation envelope (black dotted curve) does not drop to zero while the particle is close to the center of the Gaussian beam. During this time the frequency related to the transverse motion of the rod is influenced significantly. In panel B, we reconstruct the particle trajectory through the cavity mode from the time evolution of the light scattering curve.[15] This is reproduced in a simulation of the rod's motion under the influence of the cavity field (see Supporting Information Figure S2).

The optical channelling effect benefits from the geometrically enhanced induced dipole moment, due to the strong anisotropy of the rods.[25] For silicon nanorods rotating in the plane perpendicular to the cavity axis the orientation-averaged

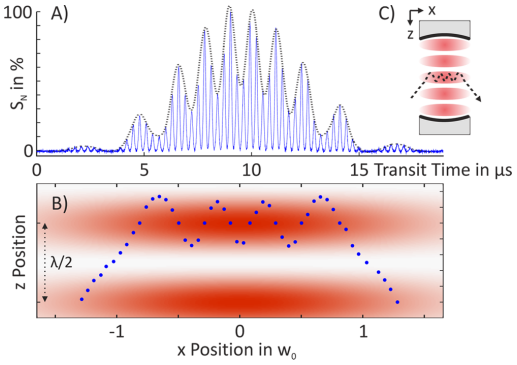

Figure 3. Transverse optical forces. (A) Scattering signal of a spinning nanorod temporarily channelled in the standing-wave field. As the particle approaches the center of the cavity mode along x, after approximately 5 μs, the optical potential of the standing light wave is sufficiently deep to trap the rod's center of mass resulting in an oscillatory motion around an antinode along z. Thus, the modulation envelope (black dotted line) no longer falls to zero, in contrast to Figure 2 (panel A, black dotted line). The oscillation frequency of up to 470 kHz is deduced from the separation between the envelope peaks. A silicon sphere with the same volume would only be trapped at a frequency of 290 kHz.[15] The fast modulation of the scattered light (blue solid line) is due to the rotation of the rod at $f_{rot} = 1.7$ MHz. (B) Reconstruction of the trajectory of the rod. (C) Illustration of the experimental geometry.

polarizability in the light field, $(\alpha_\parallel + \alpha_\perp)/2$, is enhanced by a factor of 2.7 in comparison to silicon spheres of the same mass. In Figure 3, we observe an enhancement of the trapping potential by a factor of 2.6.

In addition to the optical force on the particle's center of mass, the cavity field exerts a torque on the rods, which tends to align them along the field polarization axis.[26] Figure 4 displays the scattering curve of a slowly rotating nanorod manipulated in both its center-of-mass motion and its rotation. In analogy to Figure 3, we observe transverse channelling, but the rotation rate (black circles) is now influenced significantly by the optical torque. The influence of the optical potential on the rotation rate is most pronounced at around 12 μs. The net increase of rotational energy during the transit of the rod can be attributed to the coupling between the rotational degrees of freedom and the time dependent optical potential (see Supporting Information Figure S3).

In conclusion, we have presented a method to tailor, launch, track, and manipulate high-mass silicon nanorods with well-defined geometry and high aspect ratio. Light scattering inside a high-finesse infrared cavity allows us to follow the translational and rotational motion of the nanorotors in real time. For some of the rods, cavity assisted 1d-trapping and even rotational forces could be demonstrated. Our results are in good agreement with theoretical expectations and show that the rod-like shape enhances the interaction between the particles and the cavity field significantly, compared to silicon nanospheres of the same mass. Optomechanical trapping and cooling of the center-of-mass motion[4,11−15] will benefit from aligning the rods along the axis of polarization. Recent studies on single particle thermodynamics[27−29] may be extended to rotating systems. Our results represent a first step toward realizing rotational and torsional nano-optomechanics[16−18,30,31]

DOI: 10.1021/acs.nanolett.5b02302
Nano Lett. 2015, 15, 5604−5608

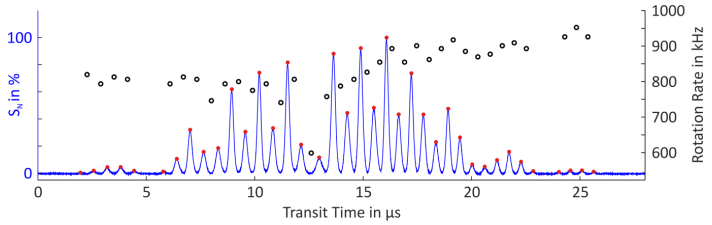

Figure 4. Optically induced torque. Scattering signal (blue curve) of a channelled nanorod, whose average rotation rate (black circles, right scale) is deduced from the separation of two adjacent scattering maxima (red dots), that is, half a rotation period. We observe that the particle first spins down to 600 kHz before it speeds up again to beyond 900 kHz (see also Supporting Information Figure S3).

and rotational cooling, which may become applicable to delicate biological nanomaterials such as the similarly shaped tobacco mosaic virus.[32,33]

Methods and Materials. *Nanorod Sculpting.* The silicon nanorod arrays were fabricated from a single crystalline Si wafer by adapting a previously described dry etching method.[34] The 380 μm thick, ⟨100⟩ cut and p-doped wafers exhibit a resistivity of 1−10 Ω cm. They were cleaned by sonication, first in acetone then in isopropyl alcohol (IPA), each for 5 min. They were then thoroughly rinsed with deionized water and dried in a stream of N_2. The clean Si wafers were spin coated with MMA resist (Copolymer resist EL9, MicroChem) at 4000 rpm for 60 s, followed by baking at 180 °C on a hot plate for 2 min. PMMA resist (Polymer resist A2, MicroChem) was deposited on the MMA layer by spinning at 2000 rpm for 60 s, followed by baking at 180 °C on a hot plate for 2 min.

An array of 250 nm diameter circular dots with 1 μm spacing was written using a Raith 150 ultrahigh-resolution e-beam lithography system (Raith GmbH, Dortmund, Germany). The patterned wafer was developed in MIBK/IPA 1:3 for 1 min, followed by rinsing with IPA for 20 s and drying in an N_2 stream. A nickel dot array was prepared by e-beam evaporating a 100 nm thick nickel layer at a base pressure of 10^{-7} Torr with a rate of 1 Å/s. Finally, the remaining resist was lifted-off in an acetone/IPA 1:1 solution, washed with IPA, and dried. The nickel nanodot arrays served as masks in the following dry etching.

Vertical silicon nanowire arrays were fabricated by applying time-multiplexed reactive ion etching in an inductively coupled plasma deep reactive ion etching machine (ICP-DRIE, PlasmaTherm SLR 770). In order to form nanopillars with a well-defined breaking point, we have implemented a Bosch process, that is, passivation followed by anisotropic etching. A variation of the ratio between the etching and the passivation times varies the scalloping and leads to different rod diameters. On the basis of this, we set up a three-stage etching process: six "passivation-etching" sequences with a time ratio of 1:1 allowed us to form 700 nm long nanorod segments. In order to create the breaking points, the ratio of the time windows was logarithmically changed to 0.7:1 during four further steps. Finally, a wider base was formed by changing the interval ratio linearly to 2:1 in six further steps. The silicon rods were cleaned by removing the nickel caps chemically.

Scattering Theory. In order to compute the normalized scattered light intensity S_N, the rods are modeled as thin, homogeneous, dielectric needles of length L, diameter D, and relative permittivity ε_r. We adopt the scattering theory for dielectric needles,[35] valid in the limit $L \gg D/2$ and $(\sqrt{(\varepsilon_r)}kD)/2 \ll 1$, to a standing-wave situation. The light intensity in the direction perpendicular to both the cavity axis $\mathbf{e}_z$ and the field polarization axis $\mathbf{e}_x$ is then proportional to

$$\frac{I_S}{I_C} \propto k^4 D^4 L^2 \left(\frac{\varepsilon_r - 1}{\varepsilon_r + 1}\right)^2 |\mathbf{e}_y \times \mathbf{u}_{int}|^2 \times [S_+^2 + 2\cos(2kz)S_+S_- + S_-^2]e^{-2(x^2+y^2)/w_0^2}$$

with $k = 2\pi/\lambda$ the wavenumber, w_0 the cavity waist, and $S_\pm = \mathrm{sinc}[\mathbf{n}\cdot(\mathbf{e}_z \pm \mathbf{e}_y)kL/2]$. Here, we denote the center-of-mass position of the rod by (x, y, z), and the orientation of the rod is determined by the radial unit vector $\mathbf{n}$. The internal field points in the direction $\mathbf{u}_{int} = 2\mathbf{e}_x + (\varepsilon_r - 1)(\mathbf{n}\cdot\mathbf{e}_x)\mathbf{n}$.

For comparison with the experiment in Figure 2C and in Supporting Information Figure S1, the scattering intensity is evaluated along the rotor trajectory and normalized with respect to its maximum. The simplified equations of motion (given in the Supporting Information) reproduce the experimental observation remarkably well, although we have $(\sqrt{(\varepsilon_r)}kD)/2 \simeq 0.7$. A precise description of the optical forces and torques requires advanced (numerical) techniques.[36]

■ ASSOCIATED CONTENT

Supporting Information

We provide simulations of the rod's dynamics for the experimental results displayed in Figures 2−4. The Supporting Information is available free of charge on the ACS Publications website at DOI: 10.1021/acs.nanolett.5b02302.

■ AUTHOR INFORMATION

Corresponding Author

*E-mail: markus.arndt@univie.ac.at.

Present Address

‖Institut de Ciencies Fotoniques, 08860 Castelldefels, Barcelona, Spain.

Notes

The authors declare no competing financial interest.

■ ACKNOWLEDGMENTS

Our work has been supported by the European Commission (304886) as well as by the Austrian Science Fund (FWF): W1210-3 and P27297. We acknowledge support by S. Puchegger and the faculty center for nanostructure research at the University of Vienna in imaging the nanorods. F.P. acknowledges the Legacy Program (Israel Science Foundation) for its support.

DOI: 10.1021/acs.nanolett.5b02302
Nano Lett. 2015, 15, 5604−5608

REFERENCES

(1) Krahne, R., Manna, L., Morello, G., Figuerola, A., George, C., Deka, S. *Physical Properties of Nanorods*; Springer: Berlin, 2013.
(2) Hornberger, K.; Gerlich, S.; Haslinger, P.; Nimmrichter, S.; Arndt, M. *Rev. Mod. Phys.* **2012**, *84*, 157−173.
(3) Arndt, M.; Hornberger, K. *Nat. Phys.* **2014**, *10*, 271−277.
(4) Bateman, J.; Nimmrichter, S.; Hornberger, K.; Ulbricht, H. *Nat. Commun.* **2014**, *5*, 4788.
(5) Arndt, M.; Nairz, O.; Vos-Andreae, J.; Keller, C.; van der Zouw, G.; Zeilinger, A. *Nature* **1999**, *401*, 680−682.
(6) Eibenberger, S.; Gerlich, S.; Arndt, M.; Mayor, M.; Tuxen, J. *Phys. Chem. Chem. Phys.* **2013**, *15*, 14696−14700.
(7) Haslinger, P.; Dörre, N.; Geyer, P.; Rodewald, J.; Nimmrichter, S.; Arndt, M. *Nat. Phys.* **2013**, *9*, 144−148.
(8) Bassi, A.; Lochan, K.; Satin, S.; Singh, T. P.; Ulbricht, H. *Rev. Mod. Phys.* **2013**, *85*, 471−527.
(9) Diosi, L. *Phys. Lett. A* **1987**, *120*, 377−381.
(10) Penrose, R. *Gen. Rel. Grav.* **1996**, *28*, 581−600.
(11) Li, T.; Kheifets, S.; Raizen, M. G. *Nat. Phys.* **2011**, *7*, 527−530.
(12) Gieseler, J.; Deutsch, B.; Quidant, R.; Novotny, L. *Phys. Rev. Lett.* **2012**, *109*, 103603.
(13) Kiesel, N.; Blaser, F.; Delic, U.; Grass, D.; Kaltenbaek, R.; Aspelmeyer, M. *Proc. Natl. Acad. Sci. U. S. A.* **2013**, *110*, 14180−14185.
(14) Millen, J.; Fonseca, P. Z. G.; Mavrogordatos, T.; Monteiro, T. S.; Barker, P. F. *Phys. Rev. Lett.* **2015**, *114*, 123602.
(15) Asenbaum, P.; Kuhn, S.; Nimmrichter, S.; Sezer, U.; Arndt, M. *Nat. Commun.* **2013**, *4*, 2743.
(16) Shi, H.; Bhattacharya, M. *J. Mod. Opt.* **2013**, *60*, 382−386.
(17) Yin, Z.; Geraci, A.; Li, T. *Int. J. Mod. Phys. B* **2013**, *27*, 1330018.
(18) Müller, T.; Reinhardt, C.; Sankey, J. C. *Phys. Rev. A: At., Mol., Opt. Phys.* **2015**, *91*, 053849.
(19) Bonin, K. D.; Kourmanov, B. *Opt. Express* **2002**, *10*, 984−989.
(20) Paterson, L.; MacDonald, M. P.; Arlt, J.; Sibbett, W.; Bryant, P. E.; Dholakia, K. *Science* **2001**, *292*, 912−914.
(21) Jones, P. H.; Palmisano, F.; Bonaccorso, F.; Gucciardi, P. G.; Calogero, G.; Ferrari, A. C.; Marago, O. M. *ACS Nano* **2009**, *3*, 3077−3084.
(22) Tong, L.; Miljkovic, V. D.; Kall, M. *Nano Lett.* **2010**, *10*, 268−73.
(23) Marago, O. M.; Jones, P. H.; Gucciardi, P. G.; Volpe, G.; Ferrari, A. C. *Nat. Nanotechnol.* **2013**, *8*, 807−19.
(24) Arita, Y.; Mazilu, M.; Dholakia, K. *Nat. Commun.* **2013**, *4*, 2374.
(25) Van De Hulst, H. C. *Light scattering by small particles*; Wiley: New York, 1957.
(26) Bishop, A. I.; Nieminen, T. A.; Heckenberg, N. R.; Rubinsztein-Dunlop, H. *Phys. Rev. A: At., Mol., Opt. Phys.* **2003**, *68*, 033802.
(27) Gieseler, J.; Novotny, L.; Quidant, R. *Nat. Phys.* **2013**, *9*, 806−810.
(28) Gieseler, J.; Quidant, R.; Dellago, C.; Novotny, L. *Nat. Nanotechnol.* **2014**, *9*, 358−64.
(29) Millen, J.; Deesuwan, T.; Barker, P.; Anders, J. *Nat. Nanotechnol.* **2014**, *9*, 425−429.
(30) Rubin, J. T.; Deych, L. I. *Phys. Rev. A: At., Mol., Opt. Phys.* **2011**, *84*, 023844.
(31) Bhattacharya, M. *J. Opt. Soc. Am. B* **2015**, *32*, B55−B60.
(32) Ashkin, A.; Dziedzic, J. M. *Science* **1987**, *235*, 1517−1520.
(33) Romero-Isart, O.; Juan, M.; Quidant, R.; Cirac, J. *New J. Phys.* **2010**, *12*, 033015.
(34) Pevzner, A.; Engel, Y.; Elnathan, R.; Ducobni, T.; Ben-Ishai, M.; Reddy, K.; Shpaisman, N.; Tsukernik, A.; Oksman, M.; Patolsky, F. *Nano Lett.* **2010**, *10*, 1202−1208.
(35) Schiffer, R.; Thielheim, K. *J. Appl. Phys.* **1979**, *50*, 2476−2483.
(36) Simpson, S. H. *J. Quant. Spectrosc. Radiat. Transfer* **2014**, *146*, 81−99.

DOI: 10.1021/acs.nanolett.5b02302
Nano Lett. 2015, 15, 5604−5608

Supporting Information, Cavity-assisted manipulation of freely rotating silicon nanorods in high vacuum

Stefan Kuhn,[1] Peter Asenbaum,[1] Alon Kosloff,[2] Michele Sclafani,[1,3]
Benjamin A. Stickler,[4] Stefan Nimmrichter,[4] Klaus Hornberger,[4]
Ori Cheshnovsky,[2] Fernando Patolsky,[2] and Markus Arndt[1,*]

[1]*University of Vienna, Faculty of Physics,*
VCQ, Boltzmanngasse 5, 1090 Vienna, Austria
[2]*School of Chemistry,Tel-Aviv University, Ramat-Aviv 69978, Israel*
[3]*Current address: Institut de Ciencies Fotoniques, 08860 Castelldefels, Barcelona, Spain*
[4]*University of Duisburg-Essen, Lotharstr. 1, 47048 Duisburg, Germany*

[*] markus.arndt@univie.ac.at

The following figures S1-S3 display the simulated dynamics of a $L = 800\,\mathrm{nm}$ long and $D = 100\,\mathrm{nm}$ thick silicon rod with mass M and moment of inertia $\Theta = ML^2/12$, which rotates in the plane perpendicular to the cavity z-axis. In this case the rod can be treated as a sub-wavelength particle at position $z(t)$, and its orientation with respect to the field polarization x-axis is described by $\boldsymbol{n} = (\cos\phi(t), \sin\phi(t), 0)$. Given a constant intra-cavity field amplitude E_0, the rod's motion is governed by the following classical equations of motion:

$$\ddot{z}(t) = -\frac{E_0^2 k}{4M}\left[\alpha_\perp + \left(\alpha_\parallel - \alpha_\perp\right)\cos^2\phi\right]\sin\left(2kz\right) e^{-2\frac{(v_x t)^2}{\omega_0^2}}$$
$$\ddot{\phi}(t) = -\frac{E_0^2}{4\Theta}\left(\alpha_\parallel - \alpha_\perp\right)\sin\left(2\phi\right)\cos^2\left(kz\right) e^{-2\frac{(v_x t)^2}{\omega_0^2}}$$

with ω_0 the cavity waist, v_x the vertical velocity of the rod, and $\alpha_{\parallel,\perp}$ the polarizability components, as given in the main text. Particle trajectories that do not pass through the cavity center, but slightly off-axis, can be accounted for by decreasing the field amplitude E_0 below the cavity value $\sqrt{4I_C/c\varepsilon_0}$. The corresponding scattering intensity is obtained by evaluating the expression given in the Methods section along the simulated trajectory. Since the scattering signal is here proportional to $S_\mathrm{N} \propto \cos^2(kz)\exp\left(-2v_x^2t^2/\omega_0^2\right)$, the center-of-mass trajectory of a freely rotating rod can be reconstructed from the measured scattering signal by averaging over the fast rotation period.

We ensure that we capture the full transit through the cavity mode by carrying out each simulation over the time interval between $\pm 10\omega_0/v_x$. In order to compare this to the measured data, the scattering signal must be normalized, and the time offset of the simulation must be adjusted, accordingly.

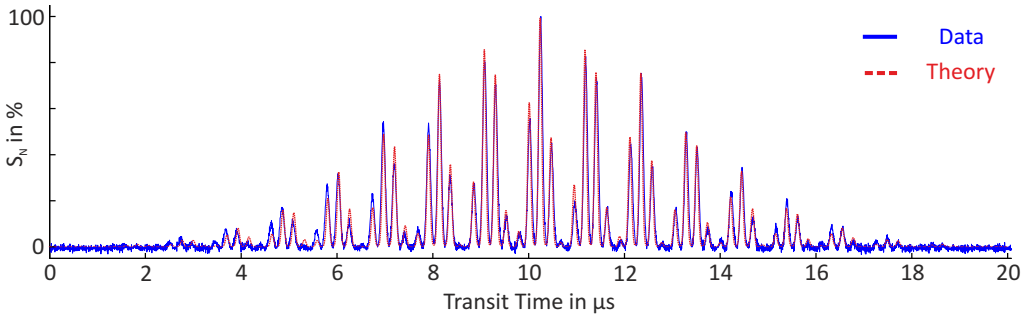

Figure S1: **Normalized scattering signal of a freely rotating nanorod.** Simulated signal as a function of time (red dashed line) in comparison to experimental data (blue solid line). The following parameters and initial values were assumed: $E_0 = 4.15 \times 10^6\,\mathrm{V/m}$, $v_x = 11.5\,\mathrm{m/s}$, $z(0) = -89.85/k$, $\dot{z}(0) = 0.74\,\mathrm{m/s}$, $\phi(0) = 0.1\,\mathrm{rad}$, $\dot{\phi}(0)/2\pi = 2.14\,\mathrm{MHz}$.

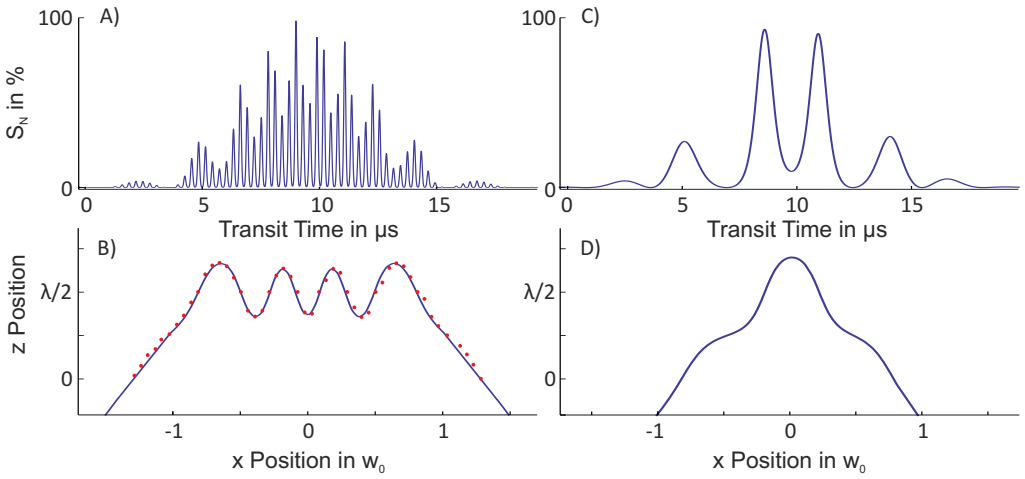

Figure S2: **Simulation of a 1d-channelled nanorod.** (A) Normalized scattering signal of a 1d-channelled particle. (B) Simulated center-of-mass trajectory (blue solid line), compared to the trajectory reconstructed from the experimental data (red dots). The following parameters and initial values were assumed: $E_0 = 8.2 \times 10^6\,\mathrm{V/m}$, $v_x = 11.3\,\mathrm{m/s}$, $z(0) = -91/k$, $\dot{z}(0) = 0.28\,\mathrm{m/s}$, $\phi(0) = -0.4\,\mathrm{rad}$, $\dot{\phi}(0)/2\pi = 1.685\,\mathrm{MHz}$. The scattering behaviour (C) and trajectory (D) of a sub-wavelength silicon nanosphere of the same mass is simulated for identical parameters. It illustrates that spherical particles are subjected to weaker optical forces compared to rods.

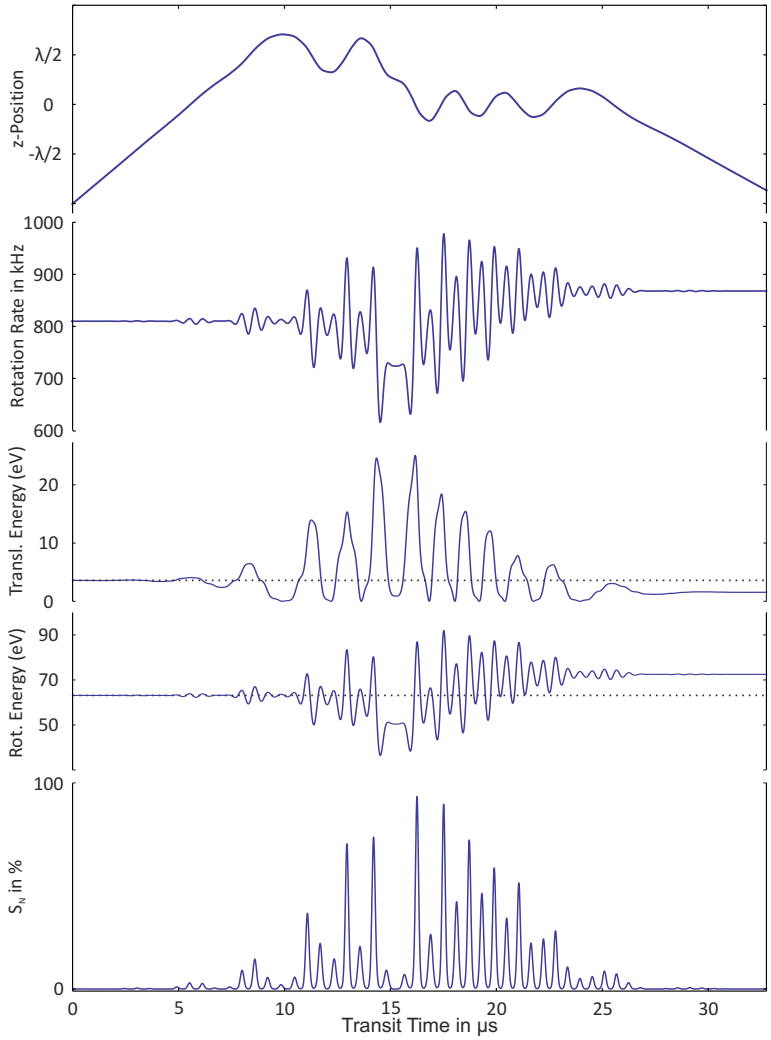

Figure S3: **Simulation of translational and rotational manipulation of a rod.** This simulation qualitatively resembles the case displayed in Figure 4 of the main text. The motional and rotational degrees of freedom couple via the optical potential, most dominantly after approximately 15 μs. At this point, the channelled rod escapes the trapping potential of an anti-node and falls into the adjacent one, while the rotation rate temporarily slows down. The following parameters and initial values were assumed: $E_0 = 8.0 \times 10^6\,\mathrm{V/m}$, $v_x = 7.94\,\mathrm{m/s}$, $z(0) = -99/k$, $\dot{z}(0) = 0.28\,\mathrm{m/s}$, $\phi(0) = -0.10098\,\mathrm{rad}$, $\dot{\phi}(0)/2\pi = 810\,\mathrm{kHz}$. After transit, we find a 7 % higher rotation rate, whereas the on-axis velocity is reduced by 34 %.

3 Cavity cooling of nanoparticles

3.1 State of the art nanoparticle cooling

Controlling and cooling the motion of dielectric nano- and micro-particles in vacuum using optical fields [87, 102, 111, 124–131] has become a thriving field of research. It is motivated by fundamental questions of quantum physics [132–134] (see Chapter 1) and by force sensing applications [135–138], single-particle nano-thermodynamics studies [139–143], electron spin resonance measurements [144, 145], and high-frequency gravitational wave detection [146]. It has recently been extended to rotational degrees of freedom [104, 113, 114, 145, 147] (see Chapter 4). The need for optical cooling techniques, in principle, arises from the lack of sources producing slow and well localised nanoparticles in high vacuum. Particles, which are confined in optical fields, couple to a heat bath, e.g. residual gas particles colliding with the particle. This results in thermal states of the particle motion which is in equilibrium with its environment. To perform quantum experiments cooling is required to prepare sufficient spatial coherence for free matter-wave interferometry (see Chapter 1), and low thermal occupation numbers in traps, close to the ground state, at which quantum effects arise.

In principle, cooling techniques can be split into two categories: Active feedback cooling is based on the detection of a particle's motion within a light field and the use of this information to actively modulate the optical forces acting on the particle accordingly; in contrast to that, cavity cooling relies on the passive, intrinsic modulation of a cavity field caused by the particle whose motion induces a modulation of the index of refraction in the cavity. In this chapter I will review the working principle and experimental realisations of both cooling schemes, present experimental results illustrating two-mode cavity cooling, discuss the prospects of cooling 10^7 amu nanoparticles in dedicated microcavities, and introduce a cooling scheme for the ro-translational motion of anisotropic particles in a high-finesse optical cavity.

3.1.1 Feedback cooling

The basic principle of feedback cooling is simple, thus versatile. By monitoring the motion of an object oscillating in a harmonic potential - e.g. an optically trapped particle or a mechanical cantilever - and applying optical forces with appropriate phase lag, motional energy can be removed from the mechanical system. First feedback

schemes based on the radiation pressure were implemented by Arthur Ashkin and colleagues to stabilise the motion of microparticles in air [148]. With this technique, microspheres trapped in high-vacuum have been cooled to millikelvin temperatures [124]. Nowadays, parametric feedback schemes are commonly employed, where the position $q(t)$ of the oscillator is measured and multiplied by its time derivative, resulting in a velocity dependent signal proportional to $q(t)\dot{q}(t)$ [149]. This corresponds to a phase-shifted signal at twice the mechanical frequency which is used to modulate the stiffness of the harmonic dipole potential of the optical trap in which the particle is oscillating. By adjusting the latency of the feedback-loop one can achieve both damping and amplification of the mechanical motion.

Parametric feedback has been implemented to drive the motion of piezoelectric nano-electromechanical systems (NEMS) [150], to cool the motion of nanoparticles optically levitated in the field of a high-NA microscope objective [125], inside an optical hollow-core fiber [102], a parabolic mirror [129], and in movable optical traps [87]. Using low-noise electronic circuits and phase-locked loops, temperatures of 150 μK have been achieved, corresponding to a mean phonon occupation number of $n = 21$ [151]. Ultimately, however, active feedback cooling runs into some limits:

Feedback cooling critically depends on the signal-to-noise ratio of the position measurement [152]. While this can be improved, employing higher optical intensities, the shot noise of the increasing radiation pressure becomes a limiting factor [131, 152]. Especially for small particles the detection limit plays a crucial role, since the Rayleigh scattering intensity, which is typically utilized to observe the particle motion, scales quadratically with the particle volume. In state of the art experiments, nanoparticle detection efficiencies of up to 0.0005 have been achieved for 100 nm diameter silica spheres [131]. It is therefore challenging to use active feedback methods to prepare particles for matter-wave interferometry experiments (see Chapter 1). For small masses, feedback cooling of 5×10^8 amu particles to 3 K has been realised [138].

3.1.2 Cavity cooling

While resonant cooling of atoms, molecular dimers and trimers has become highly advanced [153–162], leading to great progress in the fields of atomic and molecular physics, direct laser cooling of complex molecules, clusters and nanoparticles is still impossible due to the lack of narrow intrinsic level structures and closed cyclic transitions that can be individually addressed. However, inspired by direct laser cooling, more than 30 years ago, a new technique was proposed to cool the motion of atoms or dielectric particles, exploiting their off-resonant interaction with the field of an optical cavity [163, 164]. The basic idea of this Sisyphus cooling technique relies on compensating the lack of intrinsic resonances by an external resonance of a high-finesse optical cavity, using the dispersive coupling between a dielectric particle and the cavity field.

Assume a cavity, which is pumped by a laser field of frequency ω_L, red-detuned by $\Delta = \omega_\mathrm{L} - \omega_\mathrm{C} < 0$ with respect to a cavity resonance ω_C. A particle in the cavity exhibits a higher refractive index than the vacuum inside the cavity and effectively increases the cavity length. Thereby it shifts the cavity towards resonance with the pump and allows more light to build up inside the cavity. When the particle moves through the cavity field, this results in a position-dependent modulation of the intra-cavity intensity with a time-lag between the motion of the particle and the change in cavity intensity. This time lag is set by the inverse of the cavity decay rate $\kappa = c\pi/2\mathcal{F}L$. It is given by the cavity length L and cavity finesse $\mathcal{F} = \pi\sqrt{R}/(1-R)$, that in turn depends on the reflectivity R of the cavity mirrors.

Dielectric particles in infrared light are high-field seekers and feel a force towards the center of a Gaussian beam or the anti-nodes of a standing light wave. For a particle in a cavity of beam waist radius w_0 and wavenumber k the optical potential can be written as

$$V(\mathbf{x}) = -\hbar U_0 \left|a\right|^2 f^2(\mathbf{x}), \tag{3.1}$$

with a the complex amplitude of the cavity field, $f^2(\mathbf{x}) = \cos^2(kz)\exp(-2(x^2+y^2)/w_0^2)$ the mode function of the Gaussian standing light wave, and the coupling rate [111, 165]

$$U_0 = \frac{\alpha\omega_\mathrm{L}}{2\varepsilon_0 V_\mathrm{m}}. \tag{3.2}$$

This coupling rate scales linearly with the angular frequency of the cavity field ω_L, the polarizability α, and thus the volume of the particle, and inversely with the cavity mode-volume $V_\mathrm{m} = \pi w_0^2 L/4$. It determines the amount $U_0 f^2(\mathbf{x})$ by which the cavity resonance is shifted due to the presence of a particle in the cavity mode. This frequency shift results in a time-delayed change of the intra-cavity intensity, which in turn is proportional to the photon number $|a|^2$. The evolution of the complex optical field amplitude can be quantified with the rate equation [166]

$$\dot{a} = \left[i\left(\Delta + U_0 f^2(\mathbf{x}(t))\right) - \kappa - \gamma f^2(\mathbf{x}(t))\right] a + \eta_\mathrm{pump}, \tag{3.3}$$

with γ the free space scattering rate, which is proportional to the square of the particle polarizability α, and η_pump the rate at which the laser pumps the cavity. For a detuning $\Delta \simeq -\kappa$, a coupling rate $U_0 \simeq \kappa$ and small scattering rates $\gamma \ll U_0, \kappa$ this results in self-induced modulation of the optical potential such that the particle has to climb up steeper potential hills than it falls down, as illustrated in Figure 3.1. This results in a loss of motional energy which is transferred to the cavity field and eventually leaks out of the cavity at the rate $\kappa\left|a(t)\right|^2$. In this way, a particle can be cooled in the radial and axial direction through its motion along the Gaussian beam waist and along the standing light wave, respectively. A more detailed semi-classical description of the

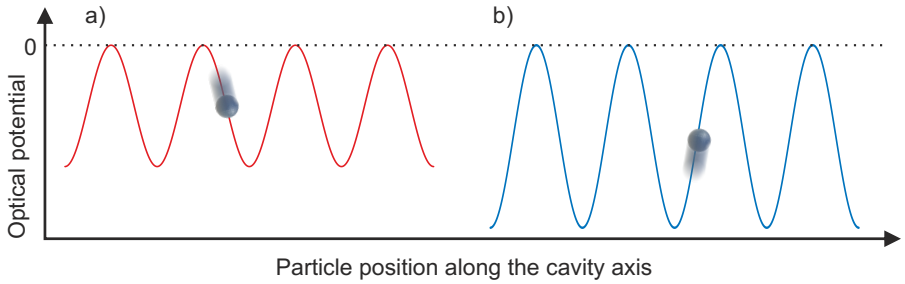

Figure 3.1: Schematic principle of cavity cooling. a) For a particle coming from a node of the standing light wave, where the coupling and thus the frequency shift exerted by the particle onto the cavity were minimal, the intra-cavity intensity is unaffected and the particle is accelerated towards the anti-node. b) After crossing the anti-node, where the coupling and frequency shift were maximal, more light is coupled into the cavity resulting in a deeper optical potential. As a consequence the particle gets decelerated more than it was accelerated before in a) resulting in an overall reduction of its kinetic energy.

cooling process can be found in References [89, 111, 116, 132, 167]. A full quantum description of nanoparticle cavity cooling is given in References [133, 134, 165].

Experimentally, off-resonant cavity cooling has first been realised with atomic ensembles [168], single atoms [169] and atomic ions [170]. For dielectric particles, cavity cooling has first been implemented for sub-micron silica spheres trapped in a cavity field under modest vacuum conditions [126], and for free silicon nanoparticles being launched through the cavity field in high-vacuum [111]. Since then, cavity cooling was optimised and nanoparticle temperatures of below 1 K have been achieved in hybrid ion-optical traps [127, 128]. For atoms, cavity cooling has recently been advanced to cool the motion of an atomic ensemble to 10 μK [171].

Fundamentally, cavity cooling is limited by the cavity decay rate, allowing for a minimal motional temperature of $T = \hbar\kappa/k_\mathrm{B}$. Experimentally, however, the achieved cavity cooling performance so far has been limited by heating due to residual gas molecules [126–128] or the interaction time of the particle with the cavity field [111]. Another technical limiting factor lies in the fact that, for decreasing temperatures, the particles become more strongly confined in the optical potential, resulting in a lower modulation depth of the intra-cavity intensity induced by the particle motion, and thus leading to lower cooling rates. This can be overcome by displacing the particles, using the electric field of an ion trap [127, 128], or optical fields, which are either formed by a separate optical tweezer [87, 133], or an additional cavity mode [126]. For particles traversing the cavity field, as described in Reference [111], the addition of a neighbouring longitudinal cavity mode can increase the cooling rate. Close to the centre of the cavity, the position of the anti-nodes of the second mode overlap with the nodes of the first mode. This reduces the conservative trapping potential while boosting the overall cooling forces [88, 89, 172, 173].

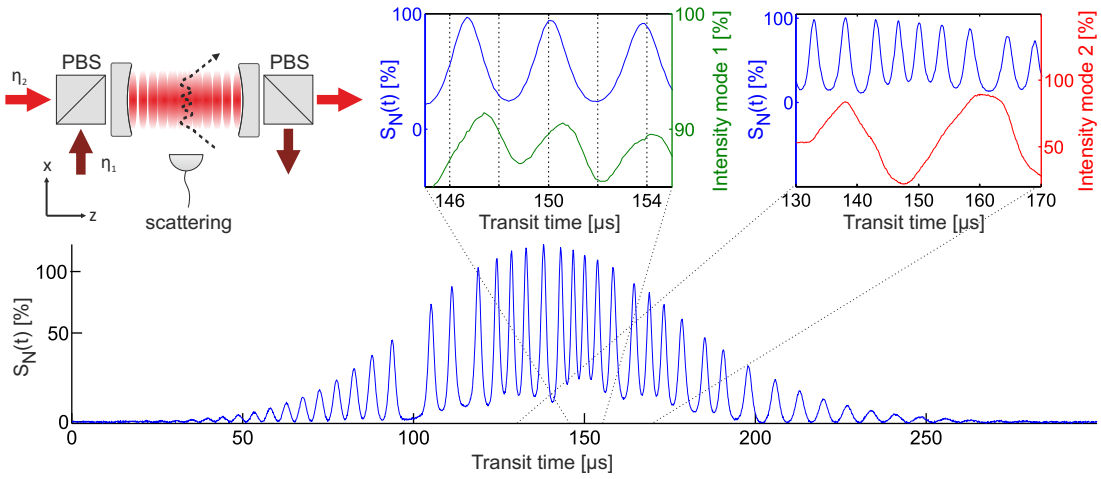

Figure 3.2: Cooling of a 300 nm diameter silica nanosphere in transit through a cavity in high vacuum (10^{-9} mbar). The cavity is pumped by two neighbouring longitudinal modes (M_1, M_2), which are both detuned by $\Delta = -\kappa$ from their respective cavity resonance. The particle enters the cavity field and freely runs over the standing light wave as seen in the light the particle scatters from M_1 (blue curve, also see Section 2.2). After approximately 100 μs the particle is trapped in one dimension and channelled by M_1 (see Section 2.3). While the particle freely crosses the cavity in forward direction we monitor the intensity of M_1 in transmission (green curve in the left sub-panel). It is modulated by the particle motion along z with the right time-delay. This results in cooling. During the particle transit the intensity of M_2 (red curve in the right sub-panel) is fluctuating due to thermal length oscillations in the mirror coating (see Reference [89]). Depending on the intensity of M_2 the conservative trapping potential of M_1 is reduced, resulting in a modulation of the frequency at which the particle is channelled (see upper right panel), thereby illustrating the basic principle of two-mode cooling. Overall, the transverse kinetic energy of the particle is reduced by a factor of three.

Figure 3.2 illustrates the basic principle of two-mode cooling with a 300 nm diameter silica sphere. While the nanoparticle transits the field of a high-finesse optical cavity (finesse $\mathcal{F} \simeq 4 \cdot 10^5$, length 3.5 mm, beam waist radius 56 μm, linewidth 110 kHz) it is one-dimensionally trapped and cooled by the first cavity mode M_1. A second cavity mode M_2, which is frequency-shifted by one free spectral range of the cavity, partially reduces the conservative trapping potential formed by the standing light wave of M_1. The intensity of M_2 fluctuates due to thermal oscillations in the coating material (see Reference [89]), at a frequency lower than the particle induced modulation frequency of M_1. When M_2 is more intense, the 1D trapping frequency in the field of M_1 is reduced, thereby illustrating the basic principle of two-mode cavity cooling. Overall, the particle is cooled by a factor of three in terms of its transverse kinetic energy. Due to the short interaction time determined by the initial particle velocity, the fluctuations in the

second cavity mode, and the weaker interaction strength of silica particles compared to silicon, the cooling performance of earlier, single-mode experiments [111] has not yet been exceeded. The full layout of the optical setup can be found in Reference [89].

New sources for silicon nanoparticles are currently being developed, and the thermal fluctuations in the mirror coating can also be compensated by additional feedback on the pump lasers. Future cryogenic particle sources (see Chapter 5) will boost the cooling. An additional limiting factor in the experiment is posed by contaminations of the mirrors with nanoparticles. They result in a significant loss of cavity finesse. Even though the mirrors are geometrically protected from being hit by neutral particles (see Section 2.2.1), attractive forces due to charges on the mirror surfaces and the nanoparticles might explain the observed contamination. Once the cavity finesse has dropped, the mirrors need to be taken out of vacuum and be replaced, or cleaned with a special polymer (First Contact), which fully recovers the reflectivity of the mirrors.

Theory predicts that two-mode cooling will allow for particle temperatures on the order of 10 μK [89] for interaction times of a few milliseconds. This will facilitate future matter-wave interferometry experiments, which will require axial temperatures of less than 50 mK (see Chapter 1). For this purpose, nanoparticle sources need to be developed that launch particles with forward velocities on the order of 10 cm/s. Also, stable trapping of nanoparticles in a cavity field at high vacuum for more than 1 ms would solve the challenge. In addition, as discussed in Chapter 1, future high-mass free-fall matter-wave interferometry experiments will be limited to nanoparticles of mass 10^7 amu or below. Up to now cavity cooling has only be realised for particles with masses on the order of 10^{10} amu. In the following we will therefore discuss how nanoparticles with diameters down to 10 nm can be coupled to and cooled by low mode-volume cavities.

3.2 Low mode-volume silicon microcavities

It follows from Equation 3.2 that the dispersive coupling to the cavity falls linearly with the particle size. In order to counteract this, cavities with smaller mode-volumes can be employed. Conventional, highly polished mirror substrates are limited to radii of curvature on the order of 1 cm. New techniques had therefore to be developed to obtain strongly curved mirrors, which maximize the confinement of the cavity field. Fibre-based microcavities have been successfully realised and optimised, using intense CO_2 lasers for material ablation at the end-facet of optical fibres [174–176]. Such cavities have been coupled to individual nitrogen vacancy centres in diamond [177, 178], single ions [179] and acoustic modes of superfluid helium [180]. Buckled dome cavities, fabricated in a monolithic self-assembly, reach single atom cooperativities of up to 65[181]. There, a thin layer of fluorocarbon between two reflecting surfaces is

heated, resulting in a deformation of the reflectors and the formation of a cavity.

In an alternative approach, mirrors can be formed by chemical etching of silicon surfaces [182, 183], which are transparent at the employed telecom wavelengths. Using a micro-machined pre-alignment system, symmetric open-access cavities have been fabricated by our collaboration partners Georg Wachter and Michael Trupke at the University of Vienna and TU Vienna, achieving mirror radii of curvature ranging from 10 μm to 1 mm. The chip surface is first smoothed through multiple steps of oxidation and etching with hydrofluoric acid to achieve a low surface roughness of below 5 Å rms. The chips have been coated with dielectric layers (Advanced Thin Films) to reach a finesse up to 100.000 [184].

A single cavity chip containing 100 cavities with mode volumes between $1-15$ pL (as compared to 7 nL for the cavities discussed in Section 3.1.2) has been placed, positioned and characterised in high-vacuum to identify the cavities with the highest finesse. This is achieved by scanning the frequency of a widely tunable laser (Toptica CTL) over the individual cavity resonances. The modehop-free tunability of this laser over the entire telecom C-band is needed to cover the large free spectral range of the cavities which is on the order of 1 THz. We can add sidebands onto the carrier frequency, using an electro-optical modulator, in order to determine the linewidths of the individual cavities [185]. One of those cavities has been selected and optically pumped, stabilizing the laser red-detuned from the cavity resonance by more than two cavity decay rates. Particles are launched through the cavity field and detected in real time by measuring the intensity of the light transmitted through the cavity. In this way we can deduce the particle-induced frequency shift of the cavity resonance (also see Chapter 2) and observe strong coupling. The successful nanoparticle detection and the prospects of using silicon microcavities for future nanoparticle cooling are discussed in Publication 3.4.

So far, the cavity performance has been limited by imperfections of the mirror shape. The finesse drops when the cavity length exceeds 130 μm because larger beam waists sample larger areas of the mirrors and experience scattering losses. Cavity decay rates of $\kappa > 2\pi \times 17$ MHz have been achieved. For cavity decay rates exceeding the modulation frequency imposed by the particle motion, the cavity field reacts almost instantaneously which results in an adiabatic modulation of the optical potential and no cooling. Improved mirror structures have been fabricated and are being coated to achieve finesses of up to 200.000 for cavities of length $l \approx 100 - 200\,\mu$m and radii of curvature around $r \approx 200\,\mu$m. They should enable cooling of particles in a mass range between $10^7 - 10^8$ amu.

Improving the smoothing procedure in the manufacturing process of even smaller micro-mirrors in the future, thereby achieving a surface roughness on the order of a few Å rms, shall allow the fabrication of cavities with $l \approx 20-30\,\mu$m, $\mathcal{F} > 2{\cdot}10^5$ and $r \approx 20\,\mu$m. They are designed for cooling of particles below 10^7 amu in mass, as discussed

in Publication 3.4. Testing the performance of these high-finesse microcavities at high intra-cavity intensities ($> 2 \times 10^7\,\mathrm{W/cm^2}$) is still subject to ongoing investigations. Microcavities with decay rates on the order of $\kappa > 2\pi \times 10\,\mathrm{MHz}$, on the contrary, can be of use for feedback experiments where the high detection efficiency provided by the cavity can be exploited.

3.3 Cavity cooling of rotational degrees of freedom

In analogy to cavity cooling of the center-of-mass motion of spherical particles, there is a cooling effect for both the translational and rotational motion of anisotropic nanoparticles [112]. While the intra-cavity field for a spherical object is modulated by position changes with respect to the cavity mode function $f(\mathbf{x})$, for dielectric rods and disks there is also a contribution due to the orientation of the particle with respect to the cavity axis and the axis of polarisation. In the same way, there is an additional term in the optical potential leading to optical torques, as described in Equation 2.4. For instance, in the case of a silicon nanorod rotating through, or being librationally trapped in, the linearly polarized cavity field, the rotational motion of the rod modulates the intra-cavity intensity. For the pump laser being red-detuned from the cavity resonance by at least the particle coupling rate U_0, this modulation exhibits the required time-lag with respect to the particle's 5D-motion in order to result in a Sisyphus cooling effect reducing the rod's rotational and translational energy, irrespective of the particle's initial position and orientation[1]. A detailed derivation and analysis of ro-translational cavity cooling, given in Publication 3.5, shows that, in principle, cooling to the ro-translational quantum ground state is feasible for realistic experimental conditions. While rods cooled into the quantum regime will enable future quantum experiments in the rotational degrees of freedom (see Chapters 4 and 5), ro-translationally cold, anisotropic particles can facilitate future high-mass matter-wave interferometry experiments, where the alignment of the rods and the shape enhanced interaction strength in an optical field can be exploited [186, 187].

[1] An animated simulation of the cooling effect for a rod rotating through the field of a high-finesse optical cavity can be found on YouTube: https://youtu.be/RZTDZi1suuA

3.4 Publication: Nanoparticle detection in an open-access silicon microcavity

S. Kuhn et al., "Nanoparticle detection in an open-access silicon microcavity", Applied Physics Letters, 111 (2017), presents the detection and strong coupling of silica nanoparticles in the field of a high-finesse silicon microcavity. The low beam waist and mode volume realised in microfabricated silicon-based cavities lead to large frequency shifts imprinted by the particles onto the cavity field, allowing for the detection of transiting particles via the light transmitted through the cavity. The prospects of such cavity systems for nanoparticle cooling as preparation stage for high-mass interferometry is discussed.

As the leading author I conceived the experiment together with F.-F. Wieser, J. Millen and M. Arndt, took all measurements together with F.-F. Wieser and J. Millen, analysed the data together with F.-F. Wieser, performed the calculations on cavity cooling together with M. Trupke and wrote the paper together with J. Millen, M. Trupke and M. Arndt. The microcavities were fabricated by G. Wachter, M. Schneider, J. Schalko, U. Schmid and M. Trupke.

Nanoparticle detection in an open-access silicon microcavity

Stefan Kuhn,[1,*] Georg Wachter,[1,2] Franz-Ferdinand Wieser,[1] James Millen,[1] Michael Schneider,[3] Johannes Schalko,[3] Ulrich Schmid,[3] Michael Trupke,[1,2] and Markus Arndt[1]

[1] *University of Vienna, Faculty of Physics, VCQ, Boltzmanngasse 5, 1090 Vienna, Austria*
[2] *Institute for Atomic and Subatomic Physics, Vienna University of Technology, VCQ, Stadionallee 2, 1020 Vienna, Austria*
[3] *Institute for Sensor and Actuator Systems, Vienna University of Technology, 1040 Vienna, Austria*

We report on the detection of free nanoparticles in a micromachined, open-access Fabry-Pérot microcavity. With a mirror separation of 130 μm, a radius of curvature of 1.3 mm, and a beam waist of 12 μm, the mode volume of our symmetric infrared cavity is smaller than 15 pL. The small beam waist, together with a finesse exceeding 34,000, enables the detection of nano-scale dielectric particles in high vacuum. This device allows monitoring of the motion of individual 150 nm radius silica nanospheres in real time. We observe strong coupling between the particles and the cavity field, a precondition for optomechanical control. We discuss the prospects for optical cooling and detection of dielectric particles smaller than 10 nm in radius and 1×10^7 amu in mass.

Optical microcavities recirculate and strongly confine light, thereby enhancing the interaction between light and matter [1, 2]. Small mode volume cavities have been coupled to single atoms [3, 4], Bose-Einstein condensates [5], organic molecules [6], quantum dots [7], and nitrogen vacancy centers [8]. Whispering gallery mode (WGM) resonators can be used to detect and characterize label-free molecules [9], single viruses [10], aerosol-particles [11] and particles with radii of a few tens of nanometers [12, 13] when the specimen is adsorbed onto the resonator. Similar results have been achieved in photonic crystal cavities [14–16] and nanoplasmonic-photonic hybrid microcavities [17].

In recent years, a growing number of research groups have utilized optical cavities to control the motion of dielectric nanoparticles [18–20]. Cavity-mediated quantum ground state cooling is predicted to be within reach for both their centre of mass motion [21–23] and their rotational degrees of freedom [24, 25]. Cold, free particles in high vacuum are considered excellent candidates for matter-wave interferometry [26, 27], in a mass range where limits to established quantum theory may be explored [28–31]. The coupling of nanoparticles to a cavity field can be increased by exploiting the shape-enhanced polarizability of non-spherical particles [32, 33], and by reducing the mode volume of the cavity. Bulk optical cavities are typically limited to beam waist radii larger than $\sim 50\,\mu$m, due to limitations on the radii of curvature of the cavity mirrors.

Here, we present the detection of free nanoparticles in transit through a chip-based, high finesse, open-access silicon Fabry-Pérot microcavity, with a 15 pL mode volume. We detect the motion of the particles via the transmitted cavity light, and extract their velocity. Such gas-phase detection and characterization is advantageous in many fields, such as aerosol physics, nanoparticle synthesis and nanoparticulate exposure studies. In addition, we observe strong coupling between a nanoparticle and the optical field, which is of utmost importance for efficient optomechanical cooling.

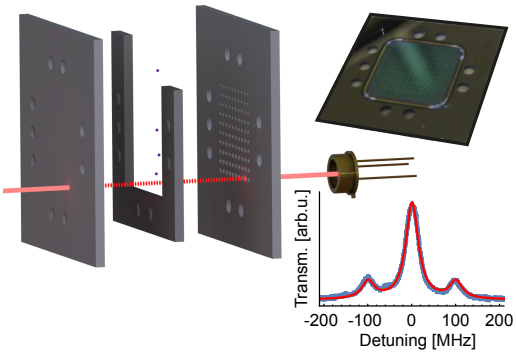

FIG. 1. Schematic of the microcavity array with nanoparticle injection. The fundamental mode of a single microcavity is strongly pumped by a laser at 1547 nm, and the transmitted light is monitored with an InGaAs photodetector. Silica nanoparticles are launched through the cavity mode via Laser Induced Acoustic Desorption [32, 35]. The upper inset shows a photograph of one of the mirror chips. The lower inset shows a scan over the TEM_{00} cavity mode in transmission (blue), in which two side-bands, 100 MHz separated from the carrier, are used to calibrate the frequency scan. From a Lorentzian fit (red) of the cavity transmission we find the cavity decay rate $\kappa/2\pi = (17 \pm 0.7)$ MHz and deduce a Finesse of 34,000 from the ratio of free spectral range to cavity linewidth κ/π.

The method for fabricating and characterizing the silicon microcavities will be explained in detail elsewhere. Briefly, two silicon chips, which are the mirror image of each other, are patterned with an array of 100 mirrors with radii of curvature ranging from 70 μm to 1.4 mm. They are separated by a 106 μm thick, silicon spacer, as illustrated in Fig. 1, which lithographically pre-aligns the cavities. The total length of the individual cavities depends in addition on the depth of the mirrors. The mirror chips are coated with a high reflectivity, multilayer dielectric coating (Advanced Thin Films, target transmis-

* stefan.kuhn@univie.ac.at

sion of 15 ppm). A single cavity, exhibiting sufficiently high finesse, is pumped with 25 mW at a wavelength of 1547 nm (Toptica CTL-1550) to excite a TEM_{00} mode, and the laser frequency is stabilized to the cavity resonance via side-of-fringe locking using the back-reflected beam. Here, we use an optical cavity with a length $L = (130 \pm 3)\,\mu$m, a free spectral range $\nu_{\mathrm{FSR}} = c/2L = (1.15 \pm 0.03)$ THz, a mode coupling of 30 %, mirror radius of curvature $R = (1.3 \pm 0.2)$ mm, a mode waist (radius) $w_0 = (12 \pm 1)\,\mu$m, a decay rate $\kappa/2\pi = (17 \pm 0.7)$ MHz, and a finesse of $\mathcal{F} = 34,000 \pm 1,300$. This yields a mode volume $V_m = 14.5\,\mathrm{pL}$ or $3,900\,\lambda^3$, and an on-resonance intracavity intensity at the waist of approximately $2 \times 10^7\,\mathrm{Wcm}^{-2}$. The cavity finesse is limited by the deviation of the mirror shape from an ideal parabolic profile, and can be improved by optimization of the fabrication parameters [34].

Silica nanoparticles (Bangs Laboratories) of radius $r = (150 \pm 20)$ nm are launched through the cavity field at a pressure of 10^{-7} mbar, using Laser Induced Acoustic Desorption [32, 35]. To detect the nanoparticles, the cavity input light is detuned from resonance by $\Delta = -2.3\,\kappa$, and the transmitted light is monitored on a photodiode. The presence of a dielectric particle inside the cavity mode effectively increases the optical path length, thus shifting the cavity towards resonance and increasing the amount of light transmitted through the mirrors. The particle also scatters light out of the cavity mode, decreasing the amount of light transmitted. A net increase of the transmitted signal is a clear sign of strong, dispersive coupling between the particle and the cavity field [36]. This allows the detection of particles with a signal-to-noise ratio (SNR) of more than 35, enabling detection of silica particles as small as 50 nm in radius.

An example nanoparticle transit is shown in Fig. 2a. As the particle traverses the optical mode in the x-direction i.e. perpendicular to the optical axis of the cavity, the transmitted signal increases with a Gaussian envelope (red dotted line), directly mirroring the Gaussian waist w_0 of the microcavity mode. Since w_0 is known from the cavity geometry, we can extract the velocity in the x-direction, $v_x = (15.6 \pm 0.1)\,\mathrm{ms}^{-1}$. There is also a fast modulation of the signal, as the nanoparticle crosses the optical standing-wave in the z-direction. Since the wavelength of the light is known, we can extract the velocity in the z-direction, $v_z = (3.13 \pm 0.07)\,\mathrm{ms}^{-1}$. There is a slight decrease in signal below the baseline level in Fig. 2a, which is due to the particle scattering light from the cavity mode. In total, the particle dispersively shifts the cavity resonance by more than $2\,\kappa$, confirming strong coupling between the particle and the cavity field. The extracted velocities for 19 nanoparticles are shown in Fig. 2b.

We now consider one specific application of such microcavities, namely their use for the optomechanical cooling of dielectric nanoparticles [18–23, 37, 38]. Cooling is believed to be necessary, for instance, to enable matter-wave interferometry with nanoscale objects [26, 27]. In

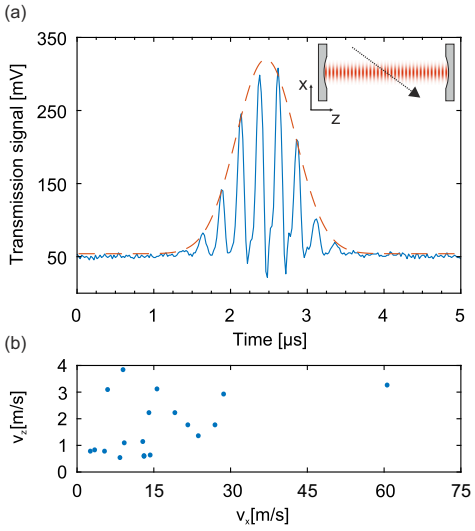

FIG. 2. (a) An example of the microcavity transmission as a 150 nm radius silica nanoparticle traverses the cavity field. The laser which pumps the cavity is red-detuned from the empty cavity resonance by $2.3\,\kappa$. The envelope due to the motion in the x-direction (see inset) across the cavity waist is indicated by the red dotted line. The periodic structure is due to the particle's motion in the z-direction, crossing multiple nodes of the cavity field. From this signal, the velocity in the x- and z-directions can be extracted ($v_x = (15.6 \pm 0.1)\,\mathrm{ms}^{-1}$ and $v_z = (3.13 \pm 0.07)\,\mathrm{ms}^{-1}$). The signal drops below the baseline due to light scattering out of the cavity mode. (b) The extracted transverse velocity v_z and forward velocity v_x for 19 particles.

particular, we will consider cooling of silicon nanoparticles due to their favourable dielectric properties [19], their applicability for nanofabrication [33] and their compatibility with optical ionization gratings [39]. Such experiments are challenging at high mass, since the short de Broglie wavelength of a massive object requires a long interferometer. For a given resolution in the interference pattern on the detector screen, the required flight time through the interferometer scales linearly with the particle mass [44], limiting the mass to the $10^6 - 10^7$ amu range [27] i.e. silicon spheres of 6-12 nm radius. Such small particles cannot be cooled in macroscopic cavities.

For optimal cooling the following criteria must be met: A) Operating in the regime of strong coupling, i.e. the dispersive frequency shift of the cavity resonance induced by the particle

$$U_0 = \frac{2\pi\omega_L r^3}{V_m}\frac{\varepsilon - 1}{\varepsilon + 2}, \tag{1}$$

(laser frequency ω_L and relative permittivity of the particle ε) is larger than the cavity decay rate $\kappa = c\pi/2\mathcal{F}L$. B) Working in the resolved side-band limit to ensure that

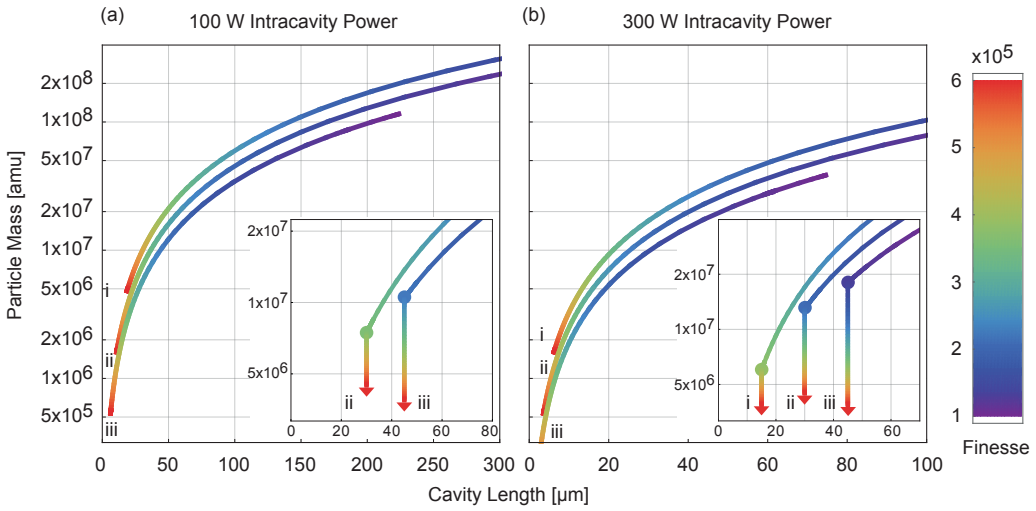

FIG. 3. Optimizing microcavity parameters to achieve optomechanical control of low-mass silicon nanospheres. We find the required cavity parameters to enable cooling of particles of a given mass under strong coupling and resolved sideband conditions (see text). We consider an intra-cavity power of (a) 100 W and (b) 300 W, at fixed L/R ratios of i) 0.5, ii) 1.0 and iii) 1.5. The insets illustrate that, even with a lower bound of $R = 30\,\mu$m (large points), it is still possible to reduce the coolable mass by increasing the cavity finesse. For realistic cavity parameters and geometries, cooling of silicon spheres with masses below 1×10^7 amu, corresponding to a silicon sphere of radius below 12 nm, is feasible.

the response of the cavity field amplitude is retarded relative to the motion of the particle. Therefore, the axial mechanical trapping frequency of the particle

$$\omega_z = \sqrt{\frac{24k^2 P_{\rm cav}}{\pi w_0^2 \rho c}\frac{\varepsilon - 1}{\varepsilon + 2}}, \tag{2}$$

(wave-vector of the cavity field k, intra-cavity power $P_{\rm cav}$ and particle density ρ) needs to be larger than κ. In order to cool small masses, the following cavity parameters can be optimized: finesse $\mathcal{F}$, beam waist radius

$$w_0 = \sqrt{\frac{\lambda}{2\pi}\sqrt{L(2R - L)}}, \tag{3}$$

via L and R, and the intra-cavity power $P_{\rm cav}$.

The parameter-space for optimal cooling is displayed in Fig. 3. The coloring of the curves indicates the minimum finesse, for a given ratio L/R and intra-cavity power, required to fulfill conditions A & B. This finesse, in turn, sets the minimal mass that can be cooled for the given set of geometrical constraints. Increasing the mass does not allow for a reduction in finesse due to condition B. At a given L/R, however, the minimum mass can be decreased by improving the finesse, as shown in the insets of Fig. 3. We consider fixed ratios L/R of i) 0.5, ii) 1.0 [45], and iii) 1.5, and intra-cavity powers of a) 100 W and b) 300 W. Hence, by moving to smaller cavities with higher finesse [43] ($\mathcal{F} > 2 \times 10^5$, $R \approx 20\,\mu$m, $L \approx 20 - 30\,\mu$m, $P_{\rm cav} > 300$ W) it will be possible to cool silicon nanoparticles with masses below 1×10^7 amu, corresponding to a sphere of radius 12 nm. Assuming the same SNR as presented here, optimized microcavities could detect particles down to 5 nm in radius.

In conclusion, we present the detection of free nanoparticles in an open-access silicon microcavity. We observe their transit via the transmitted cavity light, extract their velocity, and observe strong coupling between the particle and intracavity field. Such a system will be useful for optomechanics, and for characterization and detection of nanoparticles, bio-molecules, viruses, and aerosols. With further improvements, this microcavity system will enable cavity cooling of a diverse range of sub-10 nm particles, which are suitable for matter-wave interferometry in a hitherto unexplored mass range of $10^6 - 10^7$ amu.

Acknowledgments

We are grateful for financial support by the Austrian Science Fund (FWF) through the projects P27297, "SiC-EiC", DK-CoQuS (W1210) and DK-Solids4Fun (W1243). We further acknowledge funding from the Vienna University of Technology research funds. JM acknowledges funding from the European Union's Horizon 2020 research and innovation programme under the Marie Skłodowska-Curie grant agreement No 654532.

[1] K. Vahala, *Nature* **424**, 839–846 (2003).
[2] Y. Zhi, X.-C. Yu, Q. Gong, L. Yang, Y.-F. Xiao, *Adv. Mater.* **29**, 1604920 (2017).
[3] T. Aoki, B. Dayan, E. Wilcut, W.P. Bowen, A.S. Parkins, T.J. Kippenberg, K.J. Vahala and H.J. Kimble, *Nature* **443**, 671–674 (2006).
[4] M. Trupke, J. Goldwin, B. Darquie, G. Dutier, S. Eriksson, J. Ashmore and E. A. Hinds, *Phys. Rev. Lett.* **99**, 063601 (2007).
[5] Y. Colombe, T. Steinmetz, G. Dubois, F. Linke, D. Hunger and J. Reichel, *Nature* **450**, 272–276 (2007).
[6] C. Toninelli, Y. Delley, T. Stöferle, A. Renn, S. Götzinger and V. Sandoghdar, *Appl. Phys. Lett.* **97**, 021107 (2010).
[7] R.J. Barbour, P.A. Dalgarno, A. Curran, K.M. Nowak, H.J. Baker, D.R. Hall, N.G. Stoltz, P. M. Petroff and R.J. Warburton, *J. Appl. Phys.* **110**, 053107 (2011).
[8] R. Albrecht, A. Bommer, C. Deutsch, J. Reichel and C. Becher, *Phys. Rev. Lett.* **110**, 243602 (2013).
[9] F. Vollmer, D. Braun, A. Libchaber, M. Khoshsima, I. Teraoka and S. Arnold, *Appl. Phys. Lett.* **80**, 4057–4059 (2002).
[10] F. Vollmer, S. Arnold and D. Keng, *Proc. Natl. Acad. Sci. USA* **105**, 2071–20704 (2008).
[11] J. Zhu, S.K. Ozdemir, Y.-F. Xiao, L. Li, L. He, D.-R. Chen and L. Yang, *Nature Photon.* **4**, 46–49 (2010).
[12] T. Lu, H. Lee, T. Chen, S. Herchak, J.-H. Kim, S. E. Fraser, R. C. Flagan and K. Vahala, *Proc. Natl. Acad. Sci. USA* **108**, 5976–5979 (2011).
[13] B.-B. Li, W. R. Clements, X.-C. Yu, K. Shi, Q. Gong, Y.-F. Xiao, *Proc. Natl. Acad. Sci. USA* **111**, 14657–14662 (2014).
[14] M.R. Lee and P.M. Fauchet, *Opt. Lett.* **32**, 3284–3286 (2007).
[15] Q. Quan, D.L. Floyd, I.B. Burgess, P.B. Deotare, I.W. Frank, S.K.Y. Tang, R. Ilic and M. Loncar, *Op. Express* **21**, 32225–32233 (2013).
[16] F. Liang and Q. Quan, *ACS Photonics* **2**, 1692–1697 (2015).
[17] V.R. Dantham, S. Holler, C. Barbre, D. Keng, V. Kolchenko and S. Arnold, *Nano Lett.* **13**, 3347–3351 (2013).
[18] N. Kiesel, F. Blaser, U. Delic, D. Grass, R. Kaltenbaek, and M. Aspelmeyer, *Proc. Natl. Acad. Sci. USA* **110**, 14180 – 14185 (2013).
[19] P. Asenbaum, S. Kuhn, S. Nimmrichter, U. Sezer, and M. Arndt, *Nat. Commun.* **4**, 2743 (2013).
[20] J. Millen, P. Z. G. Fonseca, T. Mavrogordatos, T. S. Monteiro, and P. F. Barker, *Phys. Rev. Lett.* **114**, 123602 (2015).
[21] D. E. Chang, C. A. Regal, S. B. Papp, D. J. Wilson, J. Ye, O. Painter, H. J. Kimble and P. Zoller, *Proc. Natl. Acad. Sci.* **107**, 1005–1010 (2010).
[22] O. Romero-Isart, M. Juan, R. Quidant, and J. Cirac, *New J. Phys.* **12**, 033015 (2010).
[23] P.F. Barker and M.N. Schneider, *Phys. Rev. A* **81**, 023826 (2010).
[24] B. A. Stickler, S. Nimmrichter, L. Martinetz, S. Kuhn, M. Arndt and K. Hornberger, *Phys. Rev. A* **94**, 033818 (2016).
[25] T.M. Hoang, Y. Ma, J. Ahn, J. Bang, F. Robicheaux, Z.-Q. Yin, and T. Li, *Phys. Rev. Lett.* **117**, 123604 (2016).
[26] M. Arndt and K. Hornberger, *Nature Phys.* **10**, 271–277 (2014).
[27] J. Bateman, S. Nimmrichter, K. Hornberger, and H. Ulbricht, *Nat. Commun.* **5**, 4788 (2014).
[28] G. C. Ghirardi, P. Pearle, and A. Rimini, *Phys. Rev. A* **42**, 78 – 89 (1990).
[29] L. Diósi, *Phys. Lett. A* **120**, 377–381 (1987).
[30] G. C. Ghirardi, R. Grassi, and A. Rimini, *Phys. Rev. A* **42**, 1057 – 1064 (1990).
[31] R. Penrose, *Gen. Rel. Grav.* **28**, 581–600 (1996).
[32] S. Kuhn, P. Asenbaum, A. Kosloff, M. Sclafani, B. A. Stickler, S. Nimmrichter, K. Hornberger, O. Cheshnovsky, F. Patolsky, and M. Arndt, *Nano Lett.* **15**, 5604–5608 (2015).
[33] A. Kosloff, O. Heifler, E. Granot and F. Patolsky, *Nano Lett.* **16**, 6960–6966 (2016).
[34] D. Kleckner, W.T.M. Irvine,S.S.R. Oemrawsingh and D. Bouwmeester, *Phys. Rev. A* **81**, 043814 (2010).
[35] J. Millen, S. Kuhn, F. Patolsky, A. Kosloff and M. Arndt, *Proc. SPIE* **9922**, 99220C (2016).
[36] M. Aspelmeyer, T. J. Kippenberg, and F. Marquardt, *Rev. Mod. Phys.* **86**, 1391–1452 (2014).
[37] P. Horak, G. Hechenblaikner, K. Gheri, H. Stecher and H. Ritsch, *Phys. Rev. Lett.* **79**, 4974–4977 (1997).
[38] V. Vuletic and S. Chu, *Phys. Rev. Lett.* **84**, 3787–3790 (2000).
[39] E. Reiger, L. Hackermüller, M. Berninger and M. Arndt, *Opt. Commun.* **264**, 326–332 (2006).
[40] R. Kaltenbaek, M. Aspelmeyer, P. F. Barker, A. Bassi, J. Bateman, K. Bongs, S. Bose, C. Braxmaier, Č. Brukner, B. Christophe, *et al.*, *EPJ Quant. Tech.* **3**, 5 (2015).
[41] O. Romero-Isart, *New J. Phys.*, accepted (2017).
[42] S. Nimmrichter, K. Hammerer, P. Asenbaum, H. Ritsch and M. Arndt *New J. Phys.* **12**, 083003 (2010).
[43] C. Derntl, M. Schneider, J. Schalko, A. Bittner, J. Schmiedmayer, U. Schmid and M. Trupke, *Opt. Express* **22**, 22111 (2014).
[44] There are proposals to overcome this limitation by operating in a zero-g environment [40] or with magnetically levitated superconductors [41].
[45] The influence of frequency-degenerate higher-order transverse modes [42] can be neglected due to the finite extent of the mirrors, which only support low order modes.

3.5 Reprint: Rotranslational cavity cooling of dielectric rods and disks

B. A. Stickler et al., "Rotranslational cavity cooling of dielectric rods and disks," Physical Review A 94, 033818 (2016), proposes the use of an optical cavity to cool the ro-translational motion of a nanorod or a disk to the quantum ground-state. Therefore, a full theoretical toolbox is developed to describe the dynamics and interaction of the nanoparticle with a cavity field. In a phase-space description a cooling rate is derived which predicts ground-state cavity cooling to be feasible under realistic experimental conditions.

As a co-author I contributed the experimental knowledge to discuss the feasibility of the proposed experiment under realistic parameters.

PHYSICAL REVIEW A **94**, 033818 (2016)

Rotranslational cavity cooling of dielectric rods and disks

Benjamin A. Stickler,[1] Stefan Nimmrichter,[1,2] Lukas Martinetz,[1] Stefan Kuhn,[3] Markus Arndt,[3] and Klaus Hornberger[1]
[1]*Faculty of Physics, University of Duisburg-Essen, Lotharstraße 1, 47048 Duisburg, Germany*
[2]*Centre for Quantum Technologies, National University of Singapore, Singapore*
[3]*Faculty of Physics, University of Vienna, VCQ, Boltzmanngasse 5, 1090 Vienna, Austria*
(Received 18 May 2016; published 12 September 2016)

We study the interaction of dielectric rods and disks with the laser field of a high-finesse cavity. The quantum master equation for the coupled particle-cavity dynamics, including Rayleigh scattering, is derived for particle sizes comparable to the laser wavelength. We demonstrate that such anisotropic nanoparticles can be captured from free flight at velocities higher than those required to capture dielectric spheres of the same volume and that efficient rotranslational cavity cooling into the deep quantum regime is achievable.

DOI: 10.1103/PhysRevA.94.033818

I. INTRODUCTION

Laser cooling and controlling the rotranslational degrees of freedom of a nanoparticle in vacuum is a challenging task [1] with far-reaching implications: Levitated dielectrics in a high-finesse cavity can be used as ultrasensitive force sensors with atto- or even zeptonewton sensitivity [2–5]. In addition, preparing nanoscale dielectrics in the deep quantum regime may allow one to address fundamental questions, such as the thermalization of a single particle [6–9] or the validity of the quantum superposition principle at high mass scales [10,11].

In the case of small molecules with a sharp internal transition, the rotranslational motion can be laser cooled by exploiting the methods developed for atoms [12–14]. Micron-sized particles in solution and low vacuum can be trapped and manipulated rotationally with optical tweezers and vortex beams [15–23]. A first step towards controlling the rotranslational state of a nanometer-sized rod in high vacuum was demonstrated recently [24].

Here, we show that nanoscale rods and disks are excellent candidates for cavity cooling [25–27], possibly even into their rotranslational ground state. This is due to a number of fortuitous properties: (i) The anisotropic shape of a dielectric appreciably enhances the effective interaction with the cavity as compared to a sphere of the same volume, and (ii) for sufficiently red-detuned cavities, efficient cooling takes place for all orientations and positions of the particle. In addition, (iii) their rotranslational motion can be tracked from the scattered light, since the particle's position and orientation are encoded in the polarization and intensity, and (iv) the final temperature is well below the rotranslational level spacing in the trap potential.

The finite extension of the dielectric must be taken into account when describing the interaction between a nanoparticle and the field of a high-finesse cavity since the laser intensity varies on the length scale of the particles [24,28–30]. Rather than using numerical techniques [31,32] or iterative methods [33], we exploit the fact that the considered particles are thin, allowing us to analytically derive the internal polarization field [34] and thus the optical potential. Here, it is crucial that we adopt the direction of the internal polarization field from the exact electrostatic solution [35] and therefore correctly account for the anisotropic susceptibility of the particle. Our resulting analytic expressions for the Markovian particle-cavity dynamics and the scattered light intensity provide the theoretical toolbox required to carry out cavity experiments with dielectric nanorods and nanodisks in high vacuum.

We start by deriving the optical potential of a dielectric rod or disk in a standing-wave cavity mode, which enters the Markovian master equation for the combined state of particle and field mode. The cooling rate due to the retarded back action of the light field is then extracted from this equation. It also determines the threshold velocity for capturing a particle in free flight. We account for recoil heating of the particle by light scattering into the vacuum modes by deriving the orientation-dependent Rayleigh scattering operators and determine the final temperature of a deeply trapped particle.

II. CAVITY INDUCED POTENTIAL

We consider a thin dielectric rod or disk, modeled as a cylinder of length ℓ, radius a, and mass M with moment of inertia perpendicular to the symmetry axis, $I_\mathrm{r} = M\ell^2/12$ or $I_\mathrm{d} = Ma^2/4$, respectively. The particle propagates through the field of a standing-wave Gaussian cavity mode of waist w_0 and wavelength $2\pi/k$; see Fig. 1. The cavity mode is driven by a pump laser of angular frequency ω_p and power $P_\mathrm{p} = \hbar\omega_\mathrm{p}\eta^2/2\kappa$, where η is the pump rate [36]. When the z axis is along the cavity axis and the x axis is in the direction of the cavity mode polarization, the local cavity field at position $\mathbf{r}' = (x', y', z')$ reads $\mathbf{E}_\mathrm{in} = \sqrt{2\hbar\omega_\mathrm{p}/\varepsilon_0 V_\mathrm{c}}\, b f(\mathbf{r}')\cos(kz')\mathbf{e}_x$, where $f(\mathbf{r}')$ is the Gaussian envelope with waist w_0 and V_c and b denote the mode volume and the dimensionless field amplitude, respectively.

Evaluating the optical force and torque exerted by the laser field on the dielectric requires knowledge of the macroscopic polarization field $\mathbf{P}$ inside the particle [37,38]. In general, the internal field must be determined numerically if the particle's extension is comparable to the laser wavelength [32]. However, in the present case one can exploit the fact that the particle is very thin in at least one direction in order to derive an approximate analytic expression for the polarization field (generalized Rayleigh-Gans approximation) [34]. Specifically, this is possible for rods and disks of (real) dielectric permittivity ε_r since $k^2a^2(\varepsilon_\mathrm{r} - 1) \ll 1$ or $k\ell(\varepsilon_\mathrm{r} - 1) \ll 1$, respectively.

The resulting internal polarization field acquires the position dependence of the external field but it is rotated

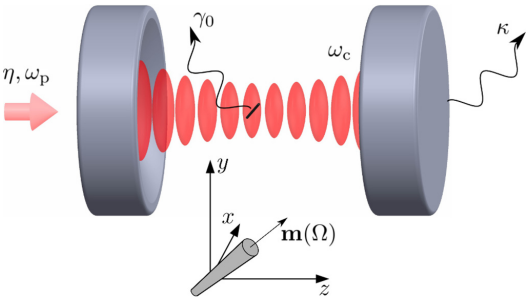

FIG. 1. A thin dielectric rod or disk traverses the laser field of a high-finesse cavity with resonance frequency ω_c, driven with pump rate η and pump frequency ω_p. The cavity detuning is $\Delta = \omega_p - \omega_c$ and κ and γ_0 are the cavity linewidth and the Rayleigh scattering rate, respectively. The orientation vector of the dielectric's symmetry axis is denoted by $\mathbf{m}(\Omega)$.

according to the dielectric's susceptibility tensor. The internal field is the exact solution to Maxwell's equations in the limit of infinitesimally thin particles and it provides a good approximation for the present scenario [24]. In particular, the field accounts correctly for the anisotropic susceptibility of the nanoparticles because its polarization is obtained by solving the corresponding electrostatic problem [34]. In the case of rods, the components of the susceptibility tensor perpendicular and orthogonal to the symmetry axis are $\chi_\parallel^{\mathrm{r}} = \varepsilon_{\mathrm{r}} - 1$ and $\chi_\perp^{\mathrm{r}} = 2(\varepsilon_{\mathrm{r}} - 1)/(\varepsilon_{\mathrm{r}} + 1)$ while $\chi_\parallel^{\mathrm{d}} = (\varepsilon_{\mathrm{r}} - 1)/\varepsilon_{\mathrm{r}}$ and $\chi_\perp^{\mathrm{d}} = \varepsilon_{\mathrm{r}} - 1$ for disks [35]. We denote the anisotropy by $\Delta\chi = \chi_\parallel - \chi_\perp$ and the maximal value by $\chi_{\mathrm{m}} = \varepsilon_{\mathrm{r}} - 1$. Note that the orientationally averaged susceptibility of a dielectric rod or disk thus exceeds the susceptibility of a dielectric sphere. With the above notation, the polarization field is proportional to $\chi_\perp \mathbf{e}_x + \Delta\chi(\mathbf{e}_x \cdot \mathbf{m})\mathbf{m}$ where $\mathbf{m}$ is the direction of the dielectric's symmetry axis. This dependence on the dielectric's orientation is familiar from anisotropically polarizable pointlike particles [39].

The particle-cavity interaction potential can now be calculated by integrating the potential energy density derived from cavity perturbation theory [30,40,41] averaged over one optical cycle, $-\mathbf{P} \cdot \mathbf{E}_{\mathrm{in}}^*/4$, or, equivalently, from the averaged force and torque densities [38]. Denoting the center-of-mass position of the dielectric by $\mathbf{r}$ and its orientation by $\mathbf{m}(\Omega)$, with $\Omega = (\alpha, \beta, \gamma)$ being the Euler angles in the z-y'-z'' convention, we find the optical potential as

$$V(\mathbf{r},\Omega) = \hbar U_0 |b|^2 f^2(\mathbf{r}) \left\{ \frac{\chi_\perp}{\chi_{\mathrm{m}}} + \frac{\Delta\chi}{\chi_{\mathrm{m}}} [\mathbf{m}(\Omega) \cdot \mathbf{e}_x]^2 \right\} \times \left\{ \frac{1}{2} + \frac{1}{2} \cos(2kz) S[\mathbf{m}(\Omega), \mathbf{e}_z] \right\}. \quad (1)$$

Here, $U_0 = -\omega_{\mathrm{p}} \chi_{\mathrm{m}} V_0 / 2V_{\mathrm{c}}$ denotes the coupling frequency with V_0 the dielectric's volume. The orientation-dependent shape function $S(\mathbf{m},\mathbf{n})$ accounts for the particle's finite extension and reads for rods and disks, respectively, as

$$S_{\mathrm{r}}(\mathbf{m},\mathbf{n}) = \frac{\sin(k\ell \mathbf{m} \cdot \mathbf{n})}{k\ell \mathbf{m} \cdot \mathbf{n}},$$

$$S_{\mathrm{d}}(\mathbf{m},\mathbf{n}) = \frac{J_1(2ka|\mathbf{m} \times \mathbf{n}|)}{ka|\mathbf{m} \times \mathbf{n}|}, \quad (2)$$

where $J_1(\cdot)$ denotes a Bessel function of the first kind. Both functions (2) take on their maximum value if their arguments vanish and, thus, it can be seen from (1) that rods tend to align with the field polarization, $\mathbf{m} = \mathbf{e}_x$, while disks align with the cavity axis, $\mathbf{m} = \mathbf{e}_z$. In the limit of small dielectrics, $k\ell \ll 1$ or $ka \ll 1$, the potential of an anisotropic pointlike particle in a standing wave laser field [39] is recovered and the potential (1) becomes proportional to the local laser intensity.

III. MASTER EQUATION FOR DIELECTRIC AND CAVITY

A dielectric particle moving through the cavity modifies the laser intensity by effectively shifting the cavity resonance frequency ω_c as well as enhancing the cavity loss rate. While this retarded reaction of the cavity on the dielectric's motion can cool the particle's motional state, Rayleigh scattering of cavity photons off the dielectric leads to recoil heating. Compared to other decoherence mechanisms [41], recoil heating dominates for deeply trapped particles and thus determines the steady-state temperature. The coupled particle-cavity dynamics can be described with the help of a Markovian quantum master equation for the total state operator ρ. This equation can be derived by coupling the particle-cavity system to the infinite bath of empty vacuum modes, which are then traced out in the Born-Markov approximation [42]. Here, scattering enhanced coupling between vacuum modes [30] can be safely neglected since we consider very thin particles, for which the scattering rate is sufficiently low. Denoting by $\hat{\mathbf{r}}$ and $\hat{\Omega}$ the rotranslational coordinate operators and by b the cavity field operator, one obtains

$$\partial_t \rho = -\frac{i}{\hbar}[\mathsf{H}_{\mathrm{p}}, \rho] - iU_0[v(\hat{\mathbf{r}},\hat{\Omega})\mathsf{b}^\dagger \mathsf{b}, \rho] + \mathcal{L}_{\mathrm{c}}\rho + \gamma_0 \sum_{s=1,2} \int_{S_2} \frac{\mathrm{d}^2\mathbf{n}}{4\pi} \left[\mathsf{L}_{\mathbf{n}s} \rho \mathsf{L}_{\mathbf{n}s}^\dagger - \frac{1}{2}\{\mathsf{L}_{\mathbf{n}s}^\dagger \mathsf{L}_{\mathbf{n}s}, \rho\} \right], \quad (3)$$

where H_{p} is the free particle Hamiltonian and $\mathcal{L}_{\mathrm{c}}\rho$ describes the unperturbed cavity dynamics,

$$\mathcal{L}_{\mathrm{c}}\rho = i[\Delta \mathsf{b}^\dagger \mathsf{b} + i\eta(\mathsf{b} - \mathsf{b}^\dagger), \rho] + \kappa(2\mathsf{b}\rho\mathsf{b}^\dagger - \{\mathsf{b}^\dagger \mathsf{b}, \rho\}), \quad (4)$$

with $v(\mathbf{r},\Omega) = V(\mathbf{r},\Omega)/\hbar U_0 |b|^2$ being the field-independent part of the interaction potential (1). The position- and orientation-dependent Lindblad operators of Rayleigh scattering into polarization direction $\boldsymbol{\epsilon}_{\mathbf{n}s}$ with scattering rate $\gamma_0 = c\chi_{\mathrm{m}}^2 V_0^2 k^4 / 6\pi V_{\mathrm{c}}$, are $\mathsf{L}_{\mathbf{n}s} = \mathsf{b} A_{\mathbf{n}s}[\hat{\mathbf{r}}, \mathbf{m}(\hat{\Omega})]$ with

$$A_{\mathbf{n}s}(\mathbf{r},\mathbf{m}) = \sqrt{\frac{3}{8}} f(\mathbf{r}) \boldsymbol{\epsilon}_{\mathbf{n}s} \cdot \left[\frac{\chi_\perp}{\chi_{\mathrm{m}}} \mathbf{e}_x + \frac{\Delta\chi}{\chi_{\mathrm{m}}} (\mathbf{m} \cdot \mathbf{e}_x)\mathbf{m} \right] e^{-ik\mathbf{n}\cdot\mathbf{r}} \times \{ e^{ikz} S[\mathbf{m}, (\mathbf{e}_z - \mathbf{n})/2] + e^{-ikz} S[\mathbf{m}, (\mathbf{e}_z + \mathbf{n})/2] \}. \quad (5)$$

They are diagonal in the rotranslational degrees of freedom and thus tend to localize the state in position and orientation. While the operator (5) transfers a superposition of the momentum kicks $\hbar k(\mathbf{n} \pm \mathbf{e}_z)$ on the dielectric's center of mass, its action

on the orientational degrees of freedom is more intricate because the angle operators $\hat{\Omega}$ are not the generators of angular momentum kicks but of the canonically conjugate momentum translations [43,44]. Thus, an eigenstate $|m_\alpha,m_\beta,m_\gamma\rangle$ of the canonical momentum operator $\hat{p}_\Omega$ conjugate to the Euler angles Ω transforms under the action of (5) into a superposition of shifted eigenstates, each weighted with the corresponding Fourier coefficient of the Lindblad operator. Nevertheless, it will turn out that the Rayleigh scattering dissipator describes diffusive rotranslational motion for deeply trapped nanoparticles. In addition, in the limit of small, isotropically polarizable point particles [28,41] the operators (5) turn proportional to the local standing wave profile.

IV. SCATTERED LIGHT INTENSITY

The light scattered by the dielectric can be utilized to track its rotranslational motion [24]. Specifically, a detector at position $R\mathbf{n}$ measures the intensity

$$I_{\mathbf{n}}(\mathbf{r},\Omega)=\frac{\hbar\omega_{\mathrm{p}}\gamma_0|b|^2}{4\pi R^2}\sum_{s=1,2}|A_{\mathbf{n}s}[\mathbf{r},\mathbf{m}(\Omega)]|^2 \tag{6}$$

as derived from the electric field integral equation [34] in the far-field limit. The polarization of the scattered field depends only on the dielectric orientation since it is orthogonal to the direction of its internal polarization field.

V. EQUATIONS OF MOTION

In order to assess under which conditions cavity cooling and trapping of the dielectric are possible, we determine the local cooling rate from the classical equations of motion. Denoting by $(\mathbf{p},p_\Omega)$ the canonically conjugate momentum coordinates, the classical equations of motion are obtained from the master equation (3) by replacing all operators with their expectation values,

$$\dot{b}=i(\Delta-U_0v)b-\left(\kappa+\frac{\gamma_{\mathrm{sc}}}{2}\right)b+\eta, \tag{7a}$$

$$\dot{\Omega}=\partial_{p_\Omega}H_{\mathrm{p}},\quad\text{and}\quad\dot{\mathbf{r}}=\partial_{\mathbf{p}}H_{\mathrm{p}}, \tag{7b}$$

$$\dot{p}_\Omega=-\partial_\Omega V+\hbar\gamma_0|b|^2\sum_{s=1,2}\int_{S_2}\frac{d^2\mathbf{n}}{4\pi}\mathrm{Im}(A^*_{\mathbf{n}s}\partial_\Omega A_{\mathbf{n}s}),$$

and

$$\dot{\mathbf{p}}=-\partial_{\mathbf{r}}V+\hbar\gamma_0|b|^2\sum_{s=1,2}\int_{S_2}\frac{d^2\mathbf{n}}{4\pi}\mathrm{Im}(A^*_{\mathbf{n}s}\partial_{\mathbf{r}}A_{\mathbf{n}s}), \tag{7c}$$

where we introduced the total scattering rate as a function of position and orientation,

$$\gamma_{\mathrm{sc}}(\mathbf{r},\Omega)=\gamma_0\sum_{s=1,2}\int_{S_2}\frac{d^2\mathbf{n}}{4\pi}|A_{\mathbf{n}s}[\mathbf{r},\mathbf{m}(\Omega)]|^2. \tag{8}$$

Equation (7a) describes the retarded reaction of the light field on the particle dynamics. The equations of motion of the particle (7b) and (7c) contain the conservative optical potential (1) as well as the nonconservative radiation pressure due to Rayleigh scattering (5). This contribution vanishes close to the minimum of the potential (1); it vanishes everywhere for isotropic point particles.

The particle-cavity equations (7) must be solved numerically in general. However, if the particle is not yet deeply trapped, we can neglect Rayleigh scattering. Assuming further that the particle moves sufficiently slowly, such that the cavity reacts nearly instantaneously, we expand the cavity amplitude to first order in all velocities and angular momenta. Thus, we obtain nonconservative equations describing the dissipative dynamics of the nanoparticle. In general, the different degrees of freedom are strongly coupled and exchange energy, such that it is not useful to define a friction rate for the individual coordinates. Nevertheless, by adapting Liouville's theorem one can calculate the rate at which an infinitesimal phase space volume centered at $(\mathbf{r},\Omega)$ expands or contracts [45],

$$\Gamma(\mathbf{r},\Omega)=\frac{4\hbar\kappa\eta^2U_0^2[\Delta-U_0v(\mathbf{r},\Omega)]}{\{\kappa^2+[\Delta-U_0v(\mathbf{r},\Omega)]^2\}^3}\left\{\frac{[\partial_{\mathbf{r}}v(\mathbf{r},\Omega)]^2}{M}+\frac{[\partial_\alpha v(\mathbf{r},\Omega)]^2}{I\sin^2\beta}+\frac{[\partial_\beta v(\mathbf{r},\Omega)]^2}{I}\right\}. \tag{9}$$

Notably, this rate is everywhere negative if the laser is sufficiently far red-detuned, i.e., for $\Delta<U_0$, and thus cooling occurs irrespective of the particle's position and orientation.

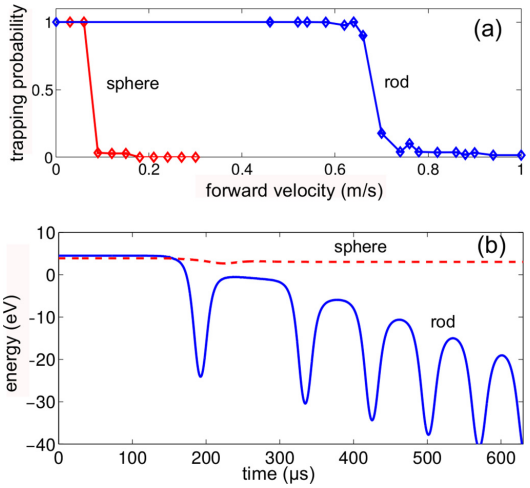

FIG. 2. (a) Trapping probability as function of the forward velocity for a silicon rod (blue; $\ell=800$ nm, $a=25$ nm) and a sphere (red; $R\simeq72$ nm) of the same volume. The nanoparticle is launched towards the cavity with forward velocity v_x. In order to obtain the trapping probability we solve the classical equations of motion (7) for several thousand initial conditions for each v_x. The transverse velocity v_z is uniformly distributed within 5% of the forward velocity v_x, assuming a collimated beam. We neglect the weak y dependence, setting $v_y=0$ and $y=0$, and assume the orientational degrees of freedom to be microcanonically distributed with a total rotation frequency of 1 MHz. For the cavity, we chose the following realizable parameters: $\lambda=1.56\,\mu$m, $\kappa=0.78$ MHz, $P_{\mathrm{in}}=10$ mW, $\Delta=-1.2\kappa$, $F=330\,000$. In panel (b) we show the total energy for a sample trajectory with $v_x=0.5$ m/s and $v_z=-0.3$ m/s. The dielectric rod (blue) is captured and cooled while a sphere (red dashed) of the same volume traverses the cavity almost unaffected. Negative energies indicate that the particle is captured.

This generalizes the results obtained for cavity cooling of point particles [46,47]. The cooling rate (9) vanishes if the particle reaches the mechanical equilibrium, where the partial derivatives of $v(\mathbf{r},\Omega)$ are zero. This could be circumvented by resorting to well-established techniques such as two-mode [41,48] or feedback cooling [49–52].

The facts that cooling occurs almost everywhere for $\Delta < U_0$ and that the effective interaction strength is enhanced due to the anisotropy have a remarkable consequence: They facilitate trapping of rods and disks at velocities at which corresponding spheres would traverse the cavity almost unaffected. This is demonstrated in Fig. 2, which shows the trapping probability as a function of the forward velocity for dielectric rods and spheres of the same volume together with the total energy along one sample trajectory.

VI. COOLING LIMIT

Recoil heating due to Rayleigh scattering prevents the dielectric from being cooled to its absolute ground state. To determine the steady-state temperature, we study the quantum master equation (3) in the case that the particle is already deeply trapped. For simplicity, we consider a moderately sized particle, $k\ell \simeq 1$ or $ka \simeq 1$, for which the interaction potential (1) can be approximated harmonically around its single minimum, implying that the rotranslational degrees of freedom are only coupled via the cavity field. (If a linear coupling between the different degrees of freedom is required by a specific protocol, this can be achieved by illumination with a second laser.)

For a dielectric rod aligned with the field polarization axis, $\mathbf{m}(\Omega_0) = \mathbf{e}_x$, at a position of maximum laser intensity, $\mathbf{r}_0 = 0$, the harmonic frequencies are

$$\omega_z^{\mathrm{r}} = \sqrt{\frac{2\hbar|U_0||b_0|^2k^2}{M}}, \quad \omega_\alpha^{\mathrm{r}} = \sqrt{\frac{2\hbar|U_0||b_0|^2\Delta\chi}{I\chi_\parallel}},$$
$$\omega_\beta^{\mathrm{r}} = \sqrt{\frac{2\hbar|U_0||b_0|^2}{I}\left[\frac{\Delta\chi}{\chi_\parallel} + \frac{(k\ell)^2}{12}\right]}. \tag{10}$$

In a similar fashion, a deeply trapped disk has its surface aligned with the cavity axis, $\mathbf{m}(\Omega_0) = \mathbf{e}_z$, at a position of maximum laser intensity and the frequencies are $\omega_z^{\mathrm{d}} = \omega_\beta^{\mathrm{d}} = \omega_z^{\mathrm{r}}$ together with $\omega_\alpha^{\mathrm{d}} = 0$. Here $b_0 = \eta/(\kappa + \gamma_{\mathrm{sc}}^0/2 + i[\Delta - U_0])$ denotes the steady-state cavity amplitude in the potential minimum with $\gamma_{\mathrm{sc}}^0 = \gamma_{\mathrm{sc}}(\mathbf{r}_0,\Omega_0)$ being the corresponding Rayleigh scattering rate. The frequencies in the transversal direction (x,y) can be safely neglected because the laser waist w_0 is typically much larger than the wavelength. The frequencies (10) are of the same order of magnitude exceeding the cavity linewidth κ. Note that the trapping frequency ω_z is determined by the maximum susceptibility $\chi_{\mathrm{m}} = \varepsilon_{\mathrm{r}} - 1$ rather than by the average value.

Similarly, we expand the Lindblad operators harmonically around the potential minimum. A straightforward calculation demonstrates that the remaining Lindblad operators are linear in the field operator b as well as in the position operators $\hat{z}$ and $\hat{\Omega}$ and thus they describe diffusive motion. One can determine an approximate expression for the steady-state temperature from the resulting relations between steady-state operator expectation values. Defining temperature as the energy difference between the steady-state energy expectation value and the energy minimum divided by Boltzmann's constant, its steady-state value is given by the recoil limit

$$T_\nu = \frac{\gamma_0\hbar^2|b_0|^2}{2M_\nu(\kappa + \gamma_{\mathrm{sc}}^0/2)k_{\mathrm{B}}} \sum_{s=1,2}\int_{S_2}\frac{d^2\mathbf{n}}{4\pi}\left|\partial_\nu A_{\mathbf{n}s}^0\right|^2, \tag{11}$$

for $\nu = z,\alpha,\beta$ with $M_z = M$, $M_{\alpha,\beta} = I$, and $\partial_\nu A_{\mathbf{n}}^0$ the derivative in direction ν of $A_{\mathbf{n}}$ evaluated at the potential minimum. In particular, for small particles, $k\ell \ll 1$, one has $T_z \simeq \gamma_0\hbar^2k^2|b_0|^2/5M\kappa_{\mathrm{eff}}k_{\mathrm{B}}$ and $T_{\alpha,\beta} \simeq \gamma_0\hbar^2\Delta\chi^2|b_0|^2/2I\chi_{\mathrm{m}}^2\kappa_{\mathrm{eff}}k_{\mathrm{B}}$ where $\kappa_{\mathrm{eff}} = \kappa + \gamma_0/2$.

As an example, we consider the silicon rods from Fig. 2. They are strongly coupled to the cavity, $|U_0|/\kappa \simeq 1.1$, yielding the final temperature $T_z \simeq 14\ \mu$K, which corresponds to a mean occupation number in the harmonic potential of $n_z \simeq 0.16$. In a similar fashion, we obtain for the rotational degrees of freedom $T_\alpha \simeq 31\ \mu$K ($n_\alpha \simeq 0.34$) and $T_\beta \simeq 29\ \mu$K ($n_\beta \simeq 0.23$). This demonstrates that reaching the rotranslational ground state should indeed be possible.

VII. CONCLUSIONS

Our findings open the door for numerous experiments and applications: The control gained over center of mass and the orientational degrees of freedom can be used for inertial sensing [2]. By monitoring the scattered light intensity one can track the dynamical impact induced by a background gas, allowing the direct observation of the thermalization of isolated orientational degrees of freedom [9] or, by using a directed beam of ultracold atoms, one can measure the scattering cross section, thus probing the dispersion interaction of nanoscale dielectrics [53].

Ground-state cooling of the nanoparticle would comprise a first step towards optomechanical experiments involving both the center-of-mass and the orientational degrees of freedom [54,55]. Such deeply trapped particles can be used as point sources for orientation-dependent interference experiments [56,57] by rapidly switching off the cavity [58,59]. If the laser intensity is reduced adiabatically [60], on the other hand, a free quantum state of low kinetic and rotational energy can be generated. Finally, aligning many anisotropic particles in a single-cavity mode might give rise to novel phenomena, such as a nonpolar version of a gas of interacting dipoles [61], where synchronization of the dielectric's motion may be observable [22].

ACKNOWLEDGMENTS

S.K. and M.A. acknowledge financial support from the Austrian Science Fund (FWF): P27297 and W1210-3. We thank James Millen for stimulating discussions.

[1] O. M. Maragò, P. H. Jones, P. G. Gucciardi, G. Volpe, and A. C. Ferrari, Optical trapping and manipulation of nanostructures, Nat. Nanotechnol. **8**, 807 (2013).

[2] O. Marago, P. Jones, F. Bonaccorso, V. Scardaci, P. Gucciardi, A. Rozhin, and A. Ferrari, Femtonewton force sensing with optically trapped nanotubes, Nano Lett. **8**, 3211 (2008).

[3] S. Olof, J. Grieve, D. Phillips, H. Rosenkranz, M. Yallop, M. Miles, A. Patil, S. Mann, and D. Carberry, Measuring nanoscale forces with living probes, Nano Lett. **12**, 6018 (2012).

[4] D. C. Moore, A. D. Rider, and G. Gratta, Search for Millicharged Particles Using Optically Levitated Microspheres, Phys. Rev. Lett. **113**, 251801 (2014).

[5] G. Ranjit, M. Cunningham, K. Casey, and A. A. Geraci, Zeptonewton force sensing with nanospheres in an optical lattice, Phys. Rev. A **93**, 053801 (2016).

[6] J. Gieseler, L. Novotny, and R. Quidant, Thermal nonlinearities in a nanomechanical oscillator, Nat. Phys. **9**, 806 (2013).

[7] J. Millen, T. Deesuwan, P. Barker, and J. Anders, Nanoscale temperature measurements using non-equilibrium Brownian dynamics of a levitated nanosphere, Nat. Nano **9**, 425 (2014).

[8] J. Gieseler, R. Quidant, C. Dellago, and L. Novotny, Dynamic relaxation of a levitated nanoparticle from a non-equilibrium steady state, Nat. Nano **9**, 358 (2014).

[9] J. Millen and A. Xuereb, Perspective on quantum thermodynamics, New J. Phys. **18**, 011002 (2016).

[10] A. Bassi, K. Lochan, S. Satin, T. Singh, and H. Ulbricht, Models of wave-function collapse, underlying theories, and experimental tests, Rev. Mod. Phys. **85**, 471 (2013).

[11] M. Arndt and K. Hornberger, Testing the limits of quantum mechanical superpositions, Nat. Phys. **10**, 271 (2014).

[12] G. Morigi, P. W. H. Pinkse, M. Kowalewski, and R. de Vivie-Riedle, Cavity Cooling of Internal Molecular Motion, Phys. Rev. Lett. **99**, 073001 (2007).

[13] E. S. Shuman, J. F. Barry, and D. DeMille, Laser cooling of a diatomic molecule, Nature (London) **467**, 820 (2010).

[14] M. Yeo, M. T. Hummon, A. L. Collopy, B. Yan, B. Hemmerling, E. Chae, J. M. Doyle, and J. Ye, Rotational State Microwave Mixing for Laser Cooling of Complex Diatomic Molecules, Phys. Rev. Lett. **114**, 223003 (2015).

[15] L. Paterson, M. MacDonald, J. Arlt, W. Sibbett, P. Bryant, and K. Dholakia, Controlled rotation of optically trapped microscopic particles, Science **292**, 912 (2001).

[16] K. D. Bonin, B. Kourmanov, and T. G. Walker, Light torque nanocontrol, nanomotors, and nanorockers, Opt. Express **10**, 984 (2002).

[17] P. Jones, F. Palmisano, F. Bonaccorso, P. Gucciardi, G. Calogero, A. Ferrari, and O. Marago, Rotation detection in light-driven nanorotors, ACS Nano **3**, 3077 (2009).

[18] L. Tong, V. D. Miljkovic, P. Johansson, and M. Kall, Plasmon hybridization reveals the interaction between individual colloidal gold nanoparticles confined in an optical potential well, Nano Lett. **11**, 4505 (2010).

[19] M. Padgett and R. Bowman, Tweezers with a twist, Nat. Photon. **5**, 343 (2011).

[20] Y. Arita, M. Mazilu, and K. Dholakia, Laser-induced rotation and cooling of a trapped microgyroscope in vacuum, Nat. Commun. **4**, 2374 (2013).

[21] O. Brzobohatý, A. V. Arzola, M. Šiler, L. Chvátal, P. Jákl, S. Simpson, and P. Zemánek, Complex rotational dynamics of multiple spheroidal particles in a circularly polarized, dual beam trap, Opt. Express **23**, 7273 (2015).

[22] S. Simpson, L. Chvátal, and P. Zemánek, Synchronization of colloidal rotors through angular optical binding, Phys. Rev. A **93**, 023842 (2016).

[23] S. E. S. Spesyvtseva and K. Dholakia, Trapping in a material world, ACS Photon. **3**, 719 (2016).

[24] S. Kuhn, P. Asenbaum, A. Kosloff, M. Sclafani, B. A. Stickler, S. Nimmrichter, K. Hornberger, O. Cheshnovsky, F. Patolsky, and M. Arndt, Cavity-assisted manipulation of freely rotating silicon nanorods in high vacuum, Nano Lett. **15**, 5604 (2015).

[25] N. Kiesel, F. Blaser, U. Delić, D. Grass, R. Kaltenbaek, and M. Aspelmeyer, Cavity cooling of an optically levitated submicron particle, Proc. Nat. Acad. Sci. U.S.A. **110**, 14180 (2013).

[26] P. Asenbaum, S. Kuhn, S. Nimmrichter, U. Sezer, and M. Arndt, Cavity cooling of free silicon nanoparticles in high vacuum, Nat. Commun. **4**, 2743 (2013).

[27] J. Millen, P. Z. G. Fonseca, T. Mavrogordatos, T. Monteiro, and P. F. Barker, Cavity Cooling a Single Charged Levitated Nanosphere, Phys. Rev. Lett. **114**, 123602 (2015).

[28] O. Romero-Isart, M. L. Juan, R. Quidant, and J. I. Cirac, Toward quantum superposition of living organisms, New J. Phys. **12**, 033015 (2010).

[29] D. Chang, K. Ni, O. Painter, and H. Kimble, Ultrahigh-Q mechanical oscillators through optical trapping, New J. Phys. **14**, 045002 (2012).

[30] A. C. Pflanzer, O. Romero-Isart, and J. I. Cirac, Master-equation approach to optomechanics with arbitrary dielectrics, Phys. Rev. A **86**, 013802 (2012).

[31] N. Voshchinnikov and V. Farafonov, Optical properties of spheroidal particles, Astrophys. Space Sci. **204**, 19 (1993).

[32] S. Simpson, Inhomogeneous and anisotropic particles in optical traps: Physical behavior and applications, J. Quant. Spectrosc. Radiat. Transfer **146**, 81 (2014).

[33] L. D. Cohen, R. D. Haracz, A. Cohen, and C. Acquista, Scattering of light from arbitrarily oriented finite cylinders, Appl. Opt. **22**, 742 (1983).

[34] R. Schiffer and K. Thielheim, Light scattering by dielectric needles and disks, J. Appl. Phys. **50**, 2476 (1979).

[35] H. van de Hulst, *Light Scattering by Small Particles* (Dover, New York, 1981).

[36] T. Salzburger and H. Ritsch, Collective transverse cavity cooling of a dense molecular beam, New J. Phys. **11**, 055025 (2009).

[37] J. D. Jackson, *Classical Electrodynamics* (Wiley, New York, 1999).

[38] S. M. Barnett and R. Loudon, On the electromagnetic force on a dielectric medium, J. Phys. B **39**, S671 (2006).

[39] H. Stapelfeldt and T. Seideman, Colloquium, Rev. Mod. Phys. **75**, 543 (2003).

[40] D. Pozar, *Microwave Engineering* (Wiley, New York, 1997).

[41] D. Chang, C. Regal, S. Papp, D. Wilson, J. Ye, O. Painter, H. Kimble, and P. Zoller, Cavity opto-mechanics using an optically levitated nanosphere, Proc. Nat. Acad. Sci. U.S.A. **107**, 1005 (2010).

[42] G. S. Agarwal, *Quantum Optics* (Cambridge University Press, Cambridge, UK, 2013).

[43] A. R. Edmonds, *Angular Momentum in Quantum Mechanics* (Princeton University Press, Princeton, NJ, 1996).

[44] D. M. Brink and G. Satchler, *Angular Momentum* (Oxford Science Publications, Oxford, UK, 2002).

[45] G. S. Ezra, On the statistical mechanics of non-Hamiltonian systems: The generalized Liouville equation, entropy, and time-dependent metrics, J. Math. Chem. **35**, 29 (2004).
[46] G. Hechenblaikner, M. Gangl, P. Horak, and H. Ritsch, Cooling an atom in a weakly driven high-Q cavity, Phys. Rev. A **58**, 3030 (1998).
[47] H. Ritsch, P. Domokos, F. Brennecke, and T. Esslinger, Cold atoms in cavity-generated dynamical optical potentials, Rev. Mod. Phys. **85**, 553 (2013).
[48] S. Habraken, W. Lechner, and P. Zoller, Resonances in dissipative optomechanics with nanoparticles: Sorting, speed rectification, and transverse cooling, Phys. Rev. A **87**, 053808 (2013).
[49] C. H. Metzger and K. Karrai, Cavity cooling of a microlever, Nature (London) **432**, 1002 (2004).
[50] T. Li, S. Kheifets, and M. G. Raizen, Millikelvin cooling of an optically trapped microsphere in vacuum, Nat. Phys. **7**, 527 (2011).
[51] J. Gieseler, B. Deutsch, R. Quidant, and L. Novotny, Subkelvin Parametric Feedback Cooling of a Laser-Trapped Nanoparticle, Phys. Rev. Lett. **109**, 103603 (2012).
[52] J. Vovrosh, M. Rashid, D. Hempston, J. Bateman, and H. Ulbricht, Controlling the motion of a nanoparticle trapped in vacuum, arXiv:1603.02917.
[53] T. Emig, N. Graham, R. L. Jaffe, and M. Kardar, Casimir Forces Between Arbitrary Compact Objects, Phys. Rev. Lett. **99**, 170403 (2007).
[54] M. Bhattacharya and P. Meystre, Using a Laguerre-Gaussian Beam to Trap and Cool the Rotational Motion of a Mirror, Phys. Rev. Lett. **99**, 153603 (2007).
[55] H. Shi and M. Bhattacharya, Optomechanics based on angular momentum exchange between light and matter, J. Phys. B: At. Mol. Opt. Phys. **49**, 153001 (2016).
[56] B. W. Shore, P. Dömötör, E. Sadurní, G. Süssmann, and W. P. Schleich, Scattering of a particle with internal structure from a single slit, New J. Phys. **17**, 013046 (2015).
[57] B. A. Stickler and K. Hornberger, Molecular rotations in matter-wave interferometry, Phys. Rev. A **92**, 023619 (2015).
[58] O. Romero-Isart, A. C. Pflanzer, F. Blaser, R. Kaltenbaek, N. Kiesel, M. Aspelmeyer, and J. I. Cirac, Large Quantum Superpositions and Interference of Massive Nanometer-Sized Objects, Phys. Rev. Lett. **107**, 020405 (2011).
[59] J. Bateman, S. Nimmrichter, K. Hornberger, and H. Ulbricht, Near-field interferometry of a free-falling nanoparticle from a point-like source, Nat. Commun. **5**, 4788 (2014).
[60] P. F. Barker and M. N. Shneider, Cavity cooling of an optically trapped nanoparticle, Phys. Rev. A **81**, 023826 (2010).
[61] S. A. Moses, J. P. Covey, M. T. Miecnikowski, B. Yan, B. Gadway, J. Ye, and D. S. Jin, Creation of a low-entropy quantum gas of polar molecules in an optical lattice, Science **350**, 659 (2015).

4 Rotational optomechanics

In recent years, a growing number of research teams have started to study optomechanical systems with rotational degrees of freedom. In the quantum regime, mechanical rotations exhibit novel features due to their non-linear equations of motion. Quantum effects, e.g. the quantization of angular momentum, are easier to access as a consequence of the anharmonic energy spectrum of the free rotor [188]. Control over all motional degrees of freedom will be of great importance for high-mass matter-wave interferometry experiments with nanoparticles, to eliminate additional decoherence and dephasing channels for non-isotropic objects [99]. Schemes to couple light to rotational degrees of freedom have been proposed, addressing the torsional motion of spiral resonators coupled to optical beams with angular momentum [189], nanorods [133] or nano-windmills [190] trapped in Laguerre-Gaussian cavity modes, and nanoparticles rotating in optical ring potentials [191].

Recently, first experiments with rotating nano-objects have been realised: Birefringent spheres have been confined and set into rotation in an optical dipole trap, observing coupling of their linear and rotational motion [147]. Charged graphene flakes have been trapped in an ion trap and spun with circularly polarised light [192]. Their rotation has been stabilized using radio-frequency electric fields [193]. High mechanical frequencies of the torsional motion of non-spherical nano-diamonds, levitated in an optical dipole trap, have been observed [145]. Alignment of levitated Yb^{3+}:YLF nanocrystals has enabled refrigeration of their internal temperature down to 130 K [194].

In this chapter, I will present our contribution to this line of research. We can stably trap and levitate silicon nanorods for more than 100 days at millibar pressures in a standing light wave optical dipole trap, formed by two counter-propagating focussed laser beams (see Publication 4.1). This allows us to measure all relevant trapping frequencies, control the nanorod motion via the polarisation within the trap, and tune the rotation rate of spinning particles via a dynamic modification of the trapping potential by changing the ellipticity of the field polarisation. The experimental results are in excellent agreement with theoretical predictions from scattering theory, collisions with gas particles, and optical dipole forces. In the same optical setup we can frequency-lock the mean rotation frequency of a levitated rod to an external clock via a periodic modulation of the trapping polarisation (see Publication 4.2). In this way, the particle follows the clock frequency with an accuracy of 1 μHz, resulting in a frequency stability $\Delta f_{\mathrm{rot}}/f_{\mathrm{rot}}$ of almost 10^{12}.

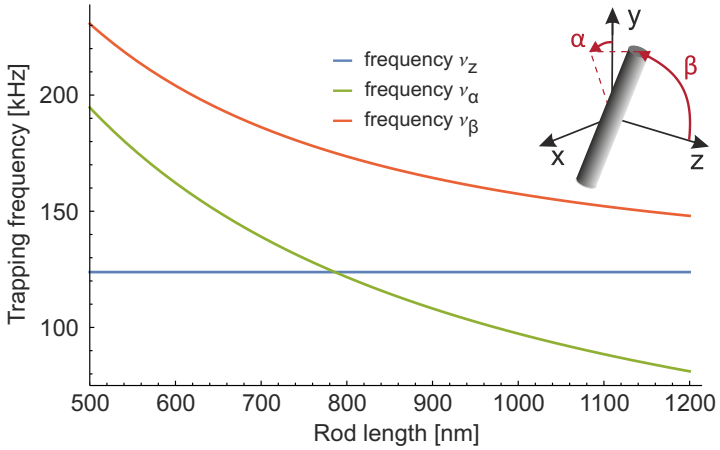

Figure 4.1: Tuning the mechanical trapping frequencies of a rod via its length. We assume a trap power of 1.35 W and a beam waist radius of 27 μm. While the axial trapping frequency is independent of the length, the librational frequencies, as defined in the inset, can be increased by shortening the rod.

These rotating systems show great potential for future quantum experiments. Preparing them in the ground state of their librational motion with parametric feedback [195] or cavity cooling, as discussed in Section 3.3 and Publication 3.5, will allow us to study the free evolution of the particle's wave packet after releasing them by harmonically switching off the trap [196], or observe coupling of the individual degrees of freedom within the trap [197, 198]. Ro-translational cavity cooling experiments will benefit from high mechanical trapping frequencies, which result from the shape enhanced polarizability (see Section 2.3) and the tunability of the trapping frequencies of the librational motion via nanofabrication. Figure 4.1 shows the dependency of the various trapping frequencies on the geometry of the rod. New feedback cooling methods for the rotational degrees of freedom will be developed, which will be based on controlling the polarisation of the trapping field (see Appendix D). Bringing the ro-translational motion of an anisotropic particle to the quantum regime will facilitate a variety of novel experiments, as discussed in Chapter 5.

Apart from quantum experiments, torsional systems have great potential for torque sensing applications. Nanoscale torsional resonators are capable of sensing torques on the order of yoktoNewtonmeter, thereby approaching the standard quantum limit of mechanical torque sensing [199, 200]. At room temperature and millibar vacuum conditions our locked rotor, in principle, achieves a torque sensitivity of sub-zeptoNewtonmeter (see Publication 4.2) and has been patented as local sensor for gas properties, e.g. pressure, flow dynamics, accommodation, and temperature, or radiation pressure and optical potentials of light fields [201]. In addition, this system will allow us to study the friction and diffusion rates in a pressure independent way to facilitate studies of the Einstein relation in the rotational degrees of freedom.

4.1 Reprint: Full rotational control of levitated silicon nanorods

S. Kuhn et al., "Full rotational control of levitated silicon nanorods," Optica 4(3), 356-360 (2017), discusses the optical trapping of silicon nanorods in a standing light wave dipole trap. Their motion is analysed through the spectrum of the light the particles scatter out of the trap. By controlling the polarisation of the trapping field the particles can either be aligned and fully trapped in five degrees of freedom in case of co-linear polarised light, or set to rotation at MHz frequencies in case of circular polarised light with equal handedness. Both types of dynamics are well understood by theory, leading to a good agreement between theoretically predicted trapping frequencies & rotation rates and the experimental data. By dynamical modification of the trap depth, exploiting the polarisation tensor of the non-spherical nanorod in elliptically polarised light, we increase the tuning range of rotation frequencies.

As a leading author I conceived the experiment together with J. Millen and M. Arndt, analysed the data together with J. Millen and B. A. Stickler and wrote the paper together with J. Millen, B. A. Stickler, K. Hornberger and M. Arndt. The theory was developed by B. A. Stickler and K. Hornberger at the University of Duisburg-Essen. The nanorods were fabricated by A. Kosloff and F. Patolsky at Tel Aviv University.

Research Article Vol. 4, No. 3 / March 2017 / Optica 356

optica

Full rotational control of levitated silicon nanorods

Stefan Kuhn,[1,*,†] Alon Kosloff,[2,†] Benjamin A. Stickler,[3] Fernando Patolsky,[2] Klaus Hornberger,[3] Markus Arndt,[1] and James Millen[1]

[1]University of Vienna, Faculty of Physics, VCQ, Boltzmanngasse 5, 1090 Vienna, Austria
[2]School of Chemistry, Tel-Aviv University, Ramat-Aviv 69978, Israel
[3]University of Duisburg-Essen, Lotharstraße 1, 47048 Duisburg, Germany
*Corresponding author: stefan.kuhn@univie.ac.at

Received 13 October 2016; revised 19 December 2016; accepted 4 February 2017 (Doc. ID 278679); published 13 March 2017

Optically levitated nano-objects in vacuum are among the highest quality mechanical oscillators, and thus of great interest for force sensing, cavity quantum optomechanics, and nanothermodynamic studies. These precision applications require exquisite control. Here, we present full control over the rotational and translational dynamics of an optically levitated silicon nanorod. We trap its center-of-mass and align it along the linear polarization of the laser field. The rod can be set into rotation at a predefined frequency by exploiting the radiation pressure exerted by elliptically polarized light. The rotational motion of the rod dynamically modifies the optical potential, which allows tuning of the rotational frequency over hundreds of kilohertz. Through nanofabrication, we can tailor all of the trapping frequencies and the optical torque, achieving reproducible dynamics that are stable over months, and analytically predict the motion with great accuracy. This first demonstration of full ro-translational control of nanoparticles in vacuum opens up the fields of rotational optomechanics, rotational ground state cooling, and the study of rotational thermodynamics in the underdamped regime.

OCIS codes: (020.7010) Laser trapping; (350.4855) Optical tweezers or optical manipulation; (220.4241) Nanostructure fabrication.
https://doi.org/10.1364/OPTICA.4.000356

1. INTRODUCTION

Nanofabrication has advanced all areas of science, technology, and medicine [1], including the field of optomechanics, where the motion of a mechanical oscillator is controlled by light. The quantum ground state of motion has been reached in optomechanical crystal devices [2] and superconducting microwave circuits [3]. Ground-state cooling enables the coherent transduction of signals [4], the production of non-classical states of light and matter [5], and the ultra-sensitive detection of motion [6] and forces [7]. Coherent optomechanical technology is limited by the coupling between the mechanical device and its environment, which leads to decoherence of quantum states, and by a reduction in mechanical quality factor due to clamping forces on the oscillator.

These limitations can be overcome by optically levitating the mechanical system such that it oscillates in a harmonic trapping potential. Optical trapping is applicable from atoms in vacuum [8,9] to complex organisms in liquid [10]. By optically levitating nanoscale objects in vacuum, ultra-high mechanical quality factors ($Q \sim 10^{12}$) are predicted [11], and it may be possible to generate macroscopic quantum superpositions [12]. Such massive quantum systems could test the limits of quantum physics [13,14], looking for the existence of new mechanisms of wavefunction collapse such as spontaneous localization [15] or gravitational effects [16–18]. Such goals require a high degree of control over all of the dynamics of the nanoparticle.

The field of levitated optomechanics is growing rapidly, with progress including feedback [19–21] and cavity cooling [22–25] to the millikelvin level and below, the sensing of forces on the zepto-Newton scale [26], and the study of Brownian motion [27] and equilibration [28] in the underdamped regime. Experiments are often limited by the quality of commercially available nanoparticles. Impurities lead to absorption of the trapping light, causing loss at low pressures [29], and even graphitization of levitated diamond [30]. Recently, rotation has been detected in levitated particles [31–34], displaying far greater rotation rates than experiments in liquid [35–38].

In this work, we trap clean, nanofabricated silicon nanorods and study their center-of-mass and rotational motion. Our particles are of uniform, tailored size and shape, allowing a high degree of repeatability, predictability, and control of the dynamics. We are able to trap the nanorods, trap and control their orientation, and tunably spin them using the radiation pressure exerted by the light field. While rotational control has been achieved in liquid [35–37,39,40], this is the first demonstration of trapping nanorods in vacuum, to the best of our knowledge, and we observe novel features such as shape enhanced light–matter

2334-2536/17/030356-05 Journal © 2017 Optical Society of America

Research Article Vol. 4, No. 3 / March 2017 / Optica 357

interactions and dynamic reshaping of the trapping potential. Such full control opens the way to optomechanical rotational cooling [34,41,42], even to the quantum level [42].

2. EXPERIMENTAL SETUP

A single silicon nanorod is optically trapped in the focus formed by two counterpropagating laser beams of wavelength $\lambda = 1550$ nm; see Fig. 1(a). At this wavelength, silicon exhibits a high relative permittivity, $\epsilon_r = 12$, and negligible absorption, which is supported by the fact that we see no signature of heating due to light absorption (following the method in Ref. [29]). The nanorods are tailored to have a length of $\ell = (725 \pm 15)$ nm and a diameter of $d = (130 \pm 13)$ nm, corresponding to a mass $M = (1.3 \pm 0.3) \times 10^{10}$ amu. They are fabricated onto a silicon chip following the methods described in Ref. [33]. The laser trap is characterized by a beam waist radius $w_0 \approx 27$ μm and the total power $P_{tot} = 1.35$ W, making a large volume trap to enhance the rate of capture. The nanorods are trapped in a clean N_2 environment at a pressure of $p_g = 4$ mbar, after being launched by laser desorption from a silicon wafer; see Refs. [33,43]. Up to 10 nanorods are simultaneously trapped, and we perturb the trapping field until a single nanorod remains. The rods can be stably trapped for months at any pressure above 1 mbar, below which they are lost, as observed in experiments with spherical nanoparticles [22,29].

3. TRAPPING THE NANORODS

The motional state of the nanorod is described by its center-of-mass position (x, y, z) and by its orientation (α, β) [see Fig. 1(b)], where x points counter-parallel to the direction of gravity and

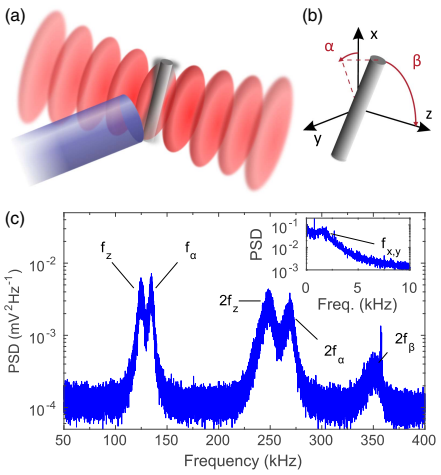

Fig. 1. (a) Nanofabricated silicon nanorods of length $\ell \simeq (725 \pm 15)$ nm and diameter $d \simeq (130 \pm 13)$ nm are optically levitated in a standing laser wave at low pressures. The light they scatter is collected by a multimode optical fiber placed close to the trap waist. (b) The rods have five degrees of freedom that can be controlled: three translational (x, y, z) and two rotational (α, β). (c) By monitoring the scattered light, trapping of all five degrees of freedom can be observed in the PSD when the trap light is linearly polarized. These data were acquired at a pressure of 4 mbar. The appearance of the various harmonics can be explained by slight misalignment of the trap as discussed in Supplement 1.

z along the beam axis. The orientation of the rod is parametrized by α, the angle between the x axis and the projection of the rod onto the x–y plane, and β the angle between the rod's symmetry axis and the beam propagation axis. The motion of the nanorod is measured via the light that the rod scatters out of the trap, which is collected with a 1 mm diameter multimode optical fiber as described in Ref. [33].

The polarization of the two trapping beams determines the properties of the optical trap. In the case of co-linear polarization, the rod aligns with the field polarization and is thus trapped in all its degrees of freedom. The resulting trapping frequencies can be measured in the power spectral density (PSD) of the scattered light signal, as shown in Fig. 1(c). Using a LiNb-polarization controller, we can perform arbitrary wave-plate operations on the polarization of the trapping light [44]. The optical setup [see Fig. 2(a)] is designed such that the rod experiences the same polarization from both arms of the counterpropagating trap. By realizing a half-wave-plate operation on the linearly polarized trapping beam we can align the rod along any direction orthogonal to the trap axis, as has been observed in liquid [36].

The trapping frequencies of a harmonically captured rod can be calculated as [42]

$$f_{x,y} = \frac{1}{2\pi}\sqrt{\frac{8P_{tot}\chi_\parallel}{\pi\varrho c w_0^4}}, \qquad f_z = \frac{1}{2\pi}\sqrt{\frac{4P_{tot}\chi_\parallel k^2}{\pi\varrho c w_0^2}},$$
$$f_\beta = \frac{1}{2\pi}\sqrt{\frac{48P_{tot}\chi_\parallel}{\pi\varrho c w_0^2\ell^2}\left(\frac{\Delta\chi}{\chi_\parallel} + \frac{(k\ell)^2}{12}\right)},$$
$$f_\alpha = \frac{1}{2\pi}\sqrt{\frac{48P_{tot}\Delta\chi}{\pi\varrho c w_0^2\ell^2}}, \tag{1}$$

where $k = 2\pi/\lambda$, $\varrho = 2330$ kg m^{-3} is the density of silicon, $\chi_\parallel = \epsilon_r - 1$ is the susceptibility along the rod's symmetry axis, and $\Delta\chi = (\epsilon_r - 1)^2/(\epsilon_r + 1)$ is the susceptibility anisotropy [45]. At the maximum input power we measure $f_{x,y} = (1.6 \pm 0.2)$ kHz, $f_z = (124 \pm 1)$ kHz, $f_\alpha = (134 \pm 1)$ kHz, and $f_\beta = (175.0 \pm 0.5)$ kHz; see Fig. 1(c). For comparison, a silicon nanosphere of the same volume under the same experimental conditions would have $f_z = 58$ kHz, and a silica sphere would have $f_z = 47$ kHz, illustrating the great potential for silicon nanorods in cavity cooling experiments [42]. We can use the measured frequencies to deduce the trapping waist radius $w_0 = (27 \pm 3)$ μm, which is the only free experimental parameter. The measured frequencies agree well with the theoretical expectations, as shown in Fig. 3(c). The slight (<5%) discrepancy between the measured and predicted value of f_β is attributed to the fact that the rods have finite diameter and the generalized Rayleigh–Gans approximation [42] is not strictly valid.

4. SPINNING THE NANORODS

When the trapping light is circularly polarized, the trapping potential for the α motion vanishes while the standing wave structure along z is retained. The radiation pressure of the laser field exerts a constant torque N_α acting on α. Adapting the theory presented in Ref. [42], the resulting torque is obtained as

$$N_\alpha = \frac{P_{tot}\Delta\chi\ell^2 d^4 k^3}{48 c w_0^2}[\Delta\chi\eta_1(k\ell) + \chi_\perp\eta_2(k\ell)], \tag{2}$$

where the two functions $\eta_{1,2}(k\ell)$ are given by

Research Article Vol. 4, No. 3 / March 2017 / Optica 358

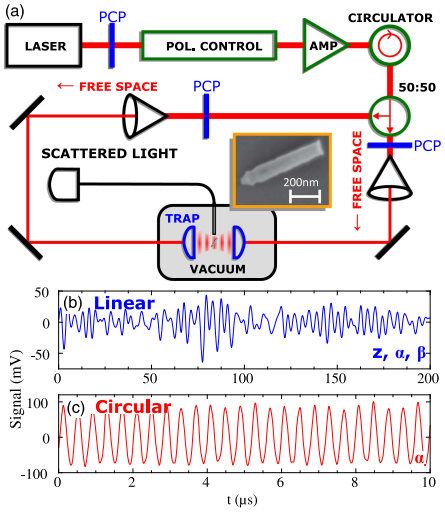

Fig. 2. (a) Experimental setup. Light at $\lambda = 1550$ nm is produced by a fiber laser (Keysight 81663A), and then goes through an electro-optical in-fiber polarization controller (EOSPACE), allowing us to realize arbitrary wave-plate operations. The light is amplified in a fiber amplifier (Hangzhou Huatai Optic HA5435B-1) and split equally to make the two arms of the trap. Stress-induced birefringence in the fibers can be accounted for with polarization controlling paddles (PCPs). The system is completely fiber-based until out-coupled to the aspheric trapping lenses ($f = 20$ mm). The inset shows a scanning electron microscopy micrograph of a rod that was launched and captured on a sample plate. The scattered light signal reveals the nanorod dynamics in case of (b) co-linear polarization, and (c) the strongly driven rotation of the rod for circularly polarized trapping light.

$$\eta_1(k\ell) = \frac{3}{4}\int_{-1}^{1} d\xi(1-\xi^2)\mathrm{sinc}^2\left(\frac{k\ell\xi}{2}\right),$$
$$\eta_2(k\ell) = \frac{3}{8}\int_{-1}^{1} d\xi(1-3\xi^2)\mathrm{sinc}^2\left(\frac{k\ell\xi}{2}\right). \quad (3)$$

For short rods, $k\ell \ll 1$, one has $\eta_1 \simeq 1$, while $\eta_2 \simeq 0$.

Collisions with residual gas molecules lead to damping of the rotational motion. Since the mean free path of the gas molecules exceeds the diameter of the rod (free molecular regime [46]), the rotational damping rate for diffuse reflection of gas molecules of mass m_g takes the form [47]

$$\Gamma = \frac{d\ell p_g}{2M}\sqrt{\frac{2\pi m_g}{k_B T}}\left(\frac{3}{2}+\frac{\pi}{4}\right), \quad (4)$$

where T is the gas temperature.

The maximum steady-state rotation frequency is obtained by balancing the torque Eq. (2) with the damping Eq. (4),

$$f_{\alpha,\max} = \frac{N_\alpha}{2\pi I\Gamma}, \quad (5)$$

with $I = M\ell^2/12$ the rod's moment of inertia. This expression agrees well with the measured value of the rotation frequency $f_{\alpha,\mathrm{rot}}$ as a function of power and pressure, as shown in Figs. 3(d) and 3(e), respectively.

A comparison of the PSD for the co-linear and the circular polarization traps is shown in Fig. 3(c). The peak related to the trapping frequency at f_α vanishes and a pronounced peak at $2f_{\alpha,\mathrm{rot}}$ arises. We are sensitive only to $2f_{\alpha,\mathrm{rot}}$ due to the symmetry of the rod. The rotation of the rod in the circularly polarized field results in a reduced average susceptibility and thus a weaker trapping potential, which shifts the axial trapping frequency to $f_{z,\mathrm{rot}} = 94$ kHz as discussed in Supplement 1. The rapid rotation in α leads to a stabilization in β and hence the

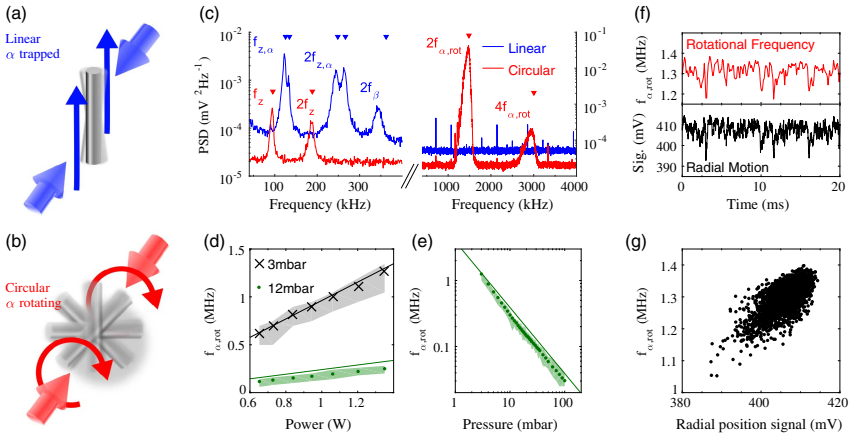

Fig. 3. Comparing the dynamics when the nanorod is (a) trapped in all degrees of freedom by linearly polarized light and (b) driven to rotate in the α direction by circularly polarized light. (c) The PSD for circularly (red) and linearly (blue) polarized light. For circular polarization, the trapping frequency f_α vanishes, and the rotational frequency $f_{\alpha,\mathrm{rot}}$ appears. The peak at f_β vanishes since the motion in β is stabilized when the rod is spinning. Markers indicate predicted trapping frequencies. The rotational frequency scales (d) linearly with power, and (e) decreases with increasing pressure, as predicted by Eq. (5). Markers represent the mean value of $f_{\alpha,\mathrm{rot}}$, the shaded areas represent the full range of $f_{\alpha,\mathrm{rot}}$, and solid lines are the theoretically expected maximal value of $f_{\alpha,\mathrm{rot}}$. The broad frequency distribution of $f_{\alpha,\mathrm{rot}}$ is due to coupling between the motion in α and x, y (radial). (f) Perturbations from the equilibrium position (lower panel) are reflected in instantaneous frequency fluctuations (top panel). (g) The correlation between the radial position and $f_{\alpha,\mathrm{rot}}$.

Research Article Vol. 4, No. 3 / March 2017 / Optica 359

complete suppression of the peak at f_β in Fig. 3(c). A similar effect has also been observed for spinning microspheres [32].

The broad distribution of frequencies about $2f_{\alpha,\mathrm{rot}}$ is due to perturbations temporarily decreasing the rotation rate, which then takes time to spin back up to the maximum value. For example, irregular excursions in the radial x, y directions lead to variations in the instantaneous rotation frequency via variation in the local light intensity, as shown in Fig. 3(f), with the correlation clearly shown in Fig. 3(g). The maximum rotation rate is limited by pressure in this setup, with an ultimate limit presumably set by material properties. In previous work, rotation rates of 50 MHz were observed for free nanorods in ultra high vacuum (UHV) [33].

5. TUNING THE ROTATIONAL FREQUENCY

To study the effect of driven rotation in more detail we use the polarization controller to perform a quarter-wave-plate (QWP) operation on the trapping light and track the motion of the rod at each setting; see Fig. 4. Starting from a linear polarization along x and increasing its ellipticity at first leads to a shift of all trapping frequencies to lower values due to a reduced trap depth, as shown in Fig. 4(a). At a QWP setting of 30°, the radiation pressure induced torque starts driving the rod into rotation over the trapping potential in the direction of α, the frequencies $f_{\alpha,\beta}$ vanish, and f_z drops to a steady value of $f_{z,\mathrm{rot}} = (94 \pm 1)$ kHz, as also seen in Fig. 3(c). Rotating beyond 45°, one may expect the nanorod to become trapped again at 60°; however, the rod is not trapped until 85°. When starting at 90° and decreasing the QWP angle, the rod spins at 60° and is not trapped until 5°, showing a symmetric hysteresis; see Fig 4(b).

This effect is due to the anisotropy of the susceptibility tensor: a trapped rod experiences the full trap depth related to $\chi_\parallel$, whereas the trapping potential for a spinning rod is proportional to the susceptibility averaged over rotations in the 2D plane orthogonal to the beam axis $(\chi_\parallel + \chi_\perp)/2$, which is smaller by a factor of 1.7. Thus, it requires a greater torque to spin a trapped rod than to maintain the rotation of an already spinning rod. The value of $f_{\alpha,\mathrm{rot}}$ varies with the ellipticity of the light, as shown in Fig. 4(b).

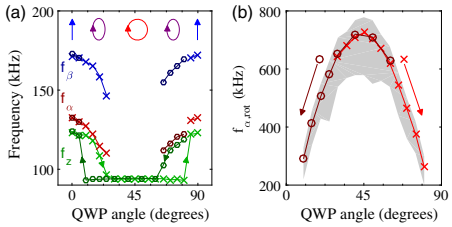

Fig. 4. Effect of performing a QWP operation on the trapping light at 5 mbar, either increasing from 0° (crosses) or decreasing from 90° (circles). At 0° and 90° the trap is linearly polarized along the y axis. At 45° the polarization is circular. (a) Shift of the trapping frequencies for different QWP settings. For small deviations from linear polarization the trapping frequencies decrease due to a lower trapping potential. At 30° from the starting linear polarization, the light is circularly polarized enough to drive $f_{\alpha,\mathrm{rot}}$, at which point $f_{\alpha,\beta}$ vanish, and f_z drops. At 85° from the starting linear polarization, the motion becomes trapped again. (b) Because of this hysteresis the driven rotational frequency $f_{\alpha,\mathrm{rot}}$ can be tuned over several hundred kilohertz via the ellipticity of the trapping field. The markers indicate the mean value of $f_{\alpha,\mathrm{rot}}$, and the shaded region represents the range of measured frequencies.

By exploiting the dynamical modification of the trap depth we can extend the range over which the rotation frequency can be tuned to many hundreds of kilohertz.

6. CONCLUSIONS

In summary, we present a method to capture and levitate nanofabricated silicon nanorods at low pressures, working with telecom wavelengths in a fiber-based setup. We can precisely control the length and diameter of our nanorods, meaning we can tailor rods to attain particular trapping and rotational frequencies. We are able to trap all relevant degrees of freedom, and control the orientation of the rods via the polarization of the trapping beams. By using circularly polarized light we can spin the nanorods at more than 1 MHz, and tune this frequency over hundreds of kilohertz by introducing ellipticity into the field polarization and through a dynamic modification of the trapping potential. When the rod is spinning we notice a stabilization of the tilt angle β and a coupling to the radial motion x, y. The system is very well understood as documented in the excellent agreement between experiment and theory. The high degree of control opens the way to study rotational optomechanics [48–50], orientational decoherence [51,52], rotational underdamped Brownian motion, and stochastic thermodynamics, and synchronization of multiple rotors due to optical binding [53]. This is the first use of silicon in an optical trap in vacuum, and its high susceptibility and low absorption in this frequency band, combined with the shape-enhanced susceptibility of rods, will enable rotational cavity cooling to the quantum level [34,42]. Such deeply trapped, cooled particles may be used as point sources for orientation-dependent interference experiments [54,55].

Funding. Austrian Science Fund (FWF) (DK-CoQuS (W1210-3), P27297); Israel Science Foundation (ISF) (Legacy Program); Horizon 2020 Framework Programme (H2020) (654532).

Acknowledgment. We acknowledge support by S. Puchegger and the faculty center for nanostructure research at the University of Vienna in imaging the nanorods. We thank Frank for his dedication to the project.

†Co-first authors.

See Supplement 1 for supporting content.

REFERENCES

1. B. Bhushan, *Springer Handbook of Nanotechnology* (Springer, 2010).
2. J. Chan, T. P. Mayer Alegre, A. H. Safavi-Naeini, J. T. Hill, A. Krause, S. Gröblacher, M. Aspelmeyer, and O. Painter, "Laser cooling of a nanomechanical oscillator into its quantum ground state," Nature **478**, 89–92 (2011).
3. J. D. Teufel, T. Donner, D. Li, J. W. Harlow, M. S. Allman, K. Cicak, A. J. Sirois, J. D. Whittaker, K. W. Lehnert, and R. W. Simmonds, "Sideband cooling of micromechanical motion to the quantum ground state," Nature **475**, 359–363 (2011).
4. J. Bochmann, A. Vainsencher, D. D. Awschalom, and A. N. Cleland, "Nanomechanical coupling between microwave and optical photons," Nat. Phys. **9**, 712–716 (2013).
5. R. Riedinger, S. Hong, R. A. Norte, J. A. Slater, J. Shang, A. G. Krause, V. Anant, M. Aspelmeyer, and S. Gröblacher, "Non-classical correlations between single photons and phonons from a mechanical oscillator," Nature **530**, 313–316 (2016).

6. O. Arcizet, P. F. Cohadon, T. Briant, M. Pinard, A. Heidmann, J. M. MacKowski, C. Michel, L. Pinard, O. Français, and L. Rousseau, "High-sensitivity optical monitoring of a micromechanical resonator with a quantum-limited optomechanical sensor," Phys. Rev. Lett. **97**, 133601 (2006).
7. A. G. Krause, M. Winger, T. D. Blasius, Q. Lin, and O. Painter, "A high-resolution microchip optomechanical accelerometer," Nat. Photonics **6**, 768–772 (2012).
8. W. D. Phillips, "Nobel Lecture: laser cooling and trapping of neutral atoms," Rev. Mod. Phys. **70**, 721–741 (1998).
9. N. Schlosser, G. Reymond, I. Protsenko, and P. Grangier, "Sub-Poissonian loading of single atoms in a microscopic dipole trap," Nature **411**, 1024–1027 (2001).
10. A. Ashkin and J. M. Dziedzic, "Optical trapping and manipulation of viruses and bacteria," Science **235**, 1517–1520 (1987).
11. D. E. Chang, C. A. Regal, S. B. Papp, D. J. Wilson, J. Ye, O. Painter, H. J. Kimble, and P. Zoller, "Cavity opto-mechanics using an optically levitated nanosphere," Proc. Natl. Acad. Sci. USA **107**, 1005–1010 (2010).
12. O. Romero-Isart, M. Juan, R. Quidant, and J. Cirac, "Toward quantum superposition of living organisms," New J. Phys. **12**, 033015 (2010).
13. M. Arndt and K. Hornberger, "Insight review: testing the limits of quantum mechanical superpositions," Nat. Phys. **10**, 271–277 (2014).
14. J. Bateman, S. Nimmrichter, K. Hornberger, and H. Ulbricht, "Near-field interferometry of a free-falling nanoparticle from a point-like source," Nat. Commun. **5**, 4788 (2014).
15. G. C. Ghirardi, P. Pearle, and A. Rimini, "Markov processes in Hilbert space and continuous spontaneous localization of systems of identical particles," Phys. Rev. A **42**, 78–89 (1990).
16. L. Diósi, "A universal master equation for the gravitational violation of quantum mechanics," Phys. Lett. A **120**, 377–381 (1987).
17. G. C. Ghirardi, R. Grassi, and A. Rimini, "Continuous-spontaneous-reduction model involving gravity," Phys. Rev. A **42**, 1057–1064 (1990).
18. R. Penrose, "On gravity's role in quantum state reduction," Gen. Relativity Gravitation **28**, 581–600 (1996).
19. T. Li, S. Kheifets, and M. G. Raizen, "Millikelvin cooling of an optically trapped microsphere in vacuum," Nat. Phys. **7**, 527–530 (2011).
20. J. Gieseler, B. Deutsch, R. Quidant, and L. Novotny, "Subkelvin parametric feedback cooling of a laser-trapped nanoparticle," Phys. Rev. Lett. **109**, 103603 (2012).
21. J. Vovrosh, M. Rashid, D. Hempston, J. Bateman, and H. Ulbricht, "Controlling the motion of a nanoparticle trapped in vacuum," arXiv:1603.02917 (2016).
22. N. Kiesel, F. Blaser, U. Delic, D. Grass, R. Kaltenbaek, and M. Aspelmeyer, "Cavity cooling of an optically levitated nanoparticle," Proc. Natl. Acad. Sci. USA **110**, 14180–14185 (2013).
23. P. Asenbaum, S. Kuhn, S. Nimmrichter, U. Sezer, and M. Arndt, "Cavity cooling of free silicon nanoparticles in high-vacuum," Nat. Commun. **4**, 2743 (2013).
24. J. Millen, P. Z. G. Fonseca, T. Mavrogordatos, T. S. Monteiro, and P. F. Barker, "Cavity cooling a single charged levitated nanosphere," Phys. Rev. Lett. **114**, 123602 (2015).
25. P. Z. G. Fonseca, E. B. Aranas, J. Millen, T. S. Monteiro, and P. F. Barker, "Nonlinear dynamics and millikelvin cavity-cooling of levitated nanoparticles," Phys. Rev. Lett. **117**, 173602 (2016).
26. G. Ranjit, M. Cunningham, K. Casey, and A. A. Geraci, "Zeptonewton force sensing with nanospheres in an optical lattice," Phys. Rev. A **93**, 053801 (2016).
27. T. Li, S. Kheifets, D. Medellin, and M. G. Raizen, "Measurement of the instantaneous velocity of a Brownian particle," Science **328**, 1673–1675 (2010).
28. J. Gieseler, R. Quidant, C. Dellago, and L. Novotny, "Dynamic relaxation of a levitated nanoparticle from a non-equilibrium steady state," Nat. Nanotech. **9**, 358–364 (2014).
29. J. Millen, T. Deesuwan, P. Barker, and J. Anders, "Nanoscale temperature measurements using non-equilibrium Brownian dynamics of a levitated nanosphere," Nat. Nanotech. **9**, 425–429 (2014).
30. A. T. M. A. Rahman, A. C. Frangeskou, M. S. Kim, S. Bose, G. W. Morley, and P. F. Barker, "Burning and graphitization of optically levitated nanodiamonds in vacuum," Sci. Rep. **6**, 21633 (2016).
31. B. Kane, "Levitated spinning graphene flakes in an electric quadrupole ion trap," Phys. Rev. B **82**, 115441 (2010).
32. Y. Arita, M. Mazilu, and K. Dholakia, "Laser-induced rotation and cooling of a trapped microgyroscope in vacuum," Nat. Commun. **4**, 2374 (2013).
33. S. Kuhn, P. Asenbaum, A. Kosloff, M. Sclafani, B. A. Stickler, S. Nimmrichter, K. Hornberger, O. Cheshnovsky, F. Patolsky, and M. Arndt, "Cavity-assisted manipulation of freely rotating silicon nanorods in high vacuum," Nano Lett. **15**, 5604–5608 (2015).
34. T. M. Hoang, Y. Ma, J. Ahn, J. Bang, F. Robicheaux, Z.-Q. Yin, and T. Li, "Torsional optomechanics of a levitated nonspherical nanoparticle," Phys. Rev. Lett. **117**, 123604 (2016).
35. M. E. J. Friese, T. A. Nieminen, N. R. Heckenberg, and H. Rubinsztein-Dunlop, "Optical alignment and spinning of laser-trapped microscopic particles," Nature **394**, 348–350 (1998).
36. L. Tong, V. D. Miljkovic, and M. Kall, "Alignment, rotation, and spinning of single plasmonic nanoparticles and nanowires using polarization dependent optical forces," Nano Lett. **10**, 268–273 (2010).
37. A. Lehmuskero, R. Ogier, T. Gschneidtner, P. Johansson, and M. Käll, "Ultrafast spinning of gold nanoparticles in water using circularly polarized light," Nano Lett. **13**, 3129–3134 (2013).
38. L. Shao, Z.-J. Yang, D. Andrén, P. Johansson, and M. Käll, "Gold nanorod rotary motors driven by resonant light scattering," ACS Nano **9**, 12542–12551 (2015).
39. F. Borghese, P. Denti, R. Saija, M. Iatì, and O. Maragò, "Radiation torque and force on optically trapped linear nanostructures," Phys. Rev. Lett. **100**, 163903 (2008).
40. P. H. Jones, F. Palmisano, F. Bonaccorso, P. G. Gucciardi, G. Calogero, A. C. Ferrari, and O. M. Marago, "Rotation detection in light-driven nanorotors," ACS Nano **3**, 3077–3084 (2009).
41. M. Bhattacharya and P. Meystre, "Using a Laguerre-Gaussian beam to trap and cool the rotational motion of a mirror," Phys. Rev. Lett. **99**, 153603 (2007).
42. B. A. Stickler, S. Nimmrichter, L. Martinetz, S. Kuhn, M. Arndt, and K. Hornberger, "Rotranslational cavity cooling of dielectric rods and disks," Phys. Rev. A **94**, 033818 (2016).
43. J. Millen, S. Kuhn, F. Patolsky, A. Kosloff, and M. Arndt, "Cooling and manipulation of nanoparticles in high vacuum," Proc. SPIE **9922**, 99220C (2016).
44. A. J. P. Van Haasteren, H. J. Frankena, J. J. G. M. Vandertol, and M. O. van Deventer, "Modeling and characterization of an electrooptic polarization controller on $LiNbO_3$," J. Lightwave Technol. **11**, 1151–1157 (1993).
45. H. van de Hulst, *Light Scattering by Small Particles* (Dover, 1981).
46. C. Cercignani, *Theory and Application of the Boltzmann Equation* (Scottish Academic, 1975).
47. A. D. Eisner and I. Gallily, "On the stochastic nature of the motion of nonspherical aerosol particles: III. The rotational diffusion diadic and applications," J. Colloid Interface Sci. **81**, 214–233 (1981).
48. J. T. Rubin and L. I. Deych, "Optical forces due to spherical microresonators and their manifestation in optically induced orbital motion of nanoparticles," Phys. Rev. A **84**, 023844 (2011).
49. M. Bhattacharya, "Rotational cavity optomechanics," J. Opt. Soc. Am. B **32**, B55 (2015).
50. H. Shi and M. Bhattacharya, "Optomechanics based on angular momentum exchange between light and matter," J. Phys. B **49**, 153001 (2015).
51. B. A. Stickler, B. Papendell, and K. Hornberger, "Spatio-orientational decoherence of nanoparticles," Phys. Rev. A **94**, 033828 (2016).
52. C. Zhong and F. Robicheaux, "Decoherence of rotational degrees of freedom," Phys. Rev. A **94**, 052109 (2016).
53. S. H. Simpson, L. Chvátal, and P. Zemánek, "Synchronization of colloidal rotors through angular optical binding," Phys. Rev. A **93**, 023842 (2016).
54. B. W. Shore, P. Dömötör, E. Sadurní, G. Süssmann, and W. P. Schleich, "Scattering of a particle with internal structure from a single slit," New J. Phys. **17**, 013046 (2015).
55. B. A. Stickler and K. Hornberger, "Molecular rotations in matter-wave interferometry," Phys. Rev. A **92**, 023619 (2015).

Supplementary Material 1

optica

Full rotational control of levitated silicon nanorods: supplementary material

STEFAN KUHN[1,A,*], ALON KOSLOFF[2,A], BENJAMIN A. STICKLER[3], FERNANDO PATOLSKY[2], KLAUS HORNBERGER[3], MARKUS ARNDT[1], AND JAMES MILLEN[1]

[1] University of Vienna, Faculty of Physics, VCQ, Boltzmanngasse 5, 1090 Vienna, Austria
[2] School of Chemistry, Tel-Aviv University, Ramat-Aviv 69978, Israel
[3] University of Duisburg-Essen, Lotharstraße 1, 47048 Duisburg, Germany
[A] Co-First Authors
[*] Corresponding author: stefan.kuhn@univie.ac.at

Published 13 March 2017

This document provides supplementary information to "Full rotational control of levitated silicon nanorods," https://doi.org/10.1364/optica.4.000356. We discuss the experimental methods to individually measure the various motional degrees of freedom of a trapped nanorod and present the theoretical framework for fitting this data. The scaling of the extracted trapping frequencies with the laser power is displayed.

https://doi.org/10.1364/optica.4.000356.s001

1. DISTINGUISHING DIFFERENT TRANSLATIONAL AND ROTATIONAL MOTIONS

All trapping frequencies of the nanorods can be calculated, based on their geometry as measured through scanning electron microscopy. The scattered light signal contains information about all degrees of freedom, with a high signal-to-noise ratio (SNR) [1]. In the manuscript, all data for (x, y, z, α) is extracted from the scattered light detector D4, and the motion in β is extracted from a polarization dependent measurement on the scattered light D5.

We independently check all motional degrees of freedom to confirm our assignation of frequencies, using other detectors. This information is not used in the manuscript. The full optical layout is shown in Fig. S1, and each detector and its uses are outlined in table S1.

Motion in z and α: We expect the trapping frequencies for z and α to be $f_z = 124\,\mathrm{kHz}$ and $f_\alpha = 134\,\mathrm{kHz}$ respectively. In the data we see a double-peak in the Power Spectral Density (PSD) of the scattered light signal D4 around these frequencies, as shown in Fig. S2a). To confirm experimentally which peak is which we implement an additional detection scheme. The nanorod rotates the polarization of the trapping light, depending on the angle it makes to the polarization axis (i.e. by an amount proportional to α).

We monitor the trapping light that has interacted with the nanorod by collecting some of the light coupled back into the fiber outcouplers, splitting it off with a 99:1 fiber beamsplitter and turning its linear polarization by 45°. This light then goes through a fiber polarizing beamsplitter (PBS), and each arm of the PBS is coupled onto a fast fiber-coupled balanced detector D1 (Thorlabs PDB420C). By this method we measure just the rotation in α, as shown in Fig. S2a). This confirms that the higher frequency peak is due to motion in α.

We also monitor the intensity fluctuations of this picked-off light on detector D2, which yields information about the motion in z, as described in Ref. [2]. The quality of this signal is poor, due to the large beam waist of our trap, and could be improved through a difference measurement. It reconfirms that the peak at 124 kHz is due to motion in z.

Motion in x, y: We pick off a small amount of the light that has interacted with the nanorod using a free-space 97:3 beamsplitter. This light is incident on a D-shaped mirror to cut the beam in half, and the resulting two beams are measured on a differencing photodiode D3. This yields the motion in y, as described in Ref. [2]. By performing a half-waveplate operation on the trapping light we can rotate the nanorod to measure x. Due to the large beam waist of our trap, the SNR is poor for this signal.

Motion in β: Using a lens we collect the scattered light emitted in the opposite direction to that collected by the multimode fiber. This light is sent through a polarizing beamsplitter cube, which is rotated by 45° with respect to the x-axis, and monitored with a photodiode D5. This yields information about the motion in β, as shown in Fig. S2b).

Detector	Model	Motional sensitivity
D1	Fiber coupled differencing photodetector, Thorlabs PDB420C	α
D2	Fiber coupled photodetector Bookham PP-10GC58L	x, y, z
D3	Homebuilt differencing photodetector	x or y
D4	Multimode fiber coupled Hamamatsu photodiode G12180-005A with Femto HCA-100M-50K-C amplifier	All degrees of freedom
D5	Free space photodetecotr Thorlabs DET10C	β

Table S1. Detectors used to measure the motion of a levitated silicon nanorod. Only detectors D4 and D5 are used in the manuscript, D1-3 are used for confirming our assignation of motional degrees of freedom.

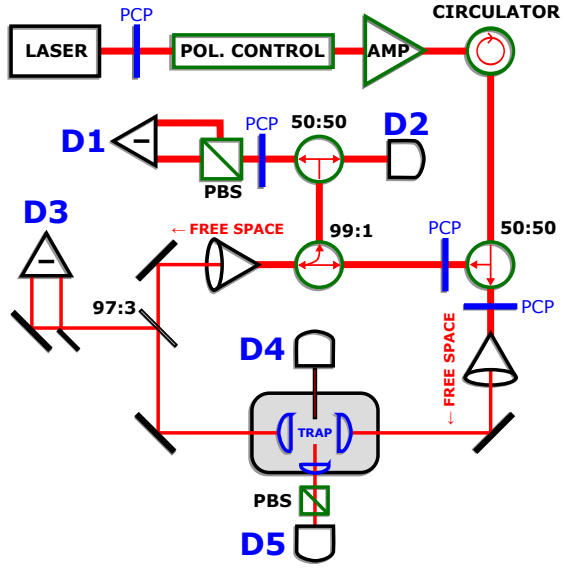

Fig. S1. The full optical layout, including mechanisms for independently measuring different trapping frequencies. A small portion of the free-space light is split on a D-shaped mirror, yielding the radial motion x on detector D3. A portion of the light that is coupled back into the fibers is picked off, and split equally to be sent to two detectors. D2 monitors the motion in z, as described in Ref. [2], and D1 the motion in α. We collect the light which the nanorod scatters using a multimode fiber, and monitor its intensity on detector D4, and use a lens to collect the scattered light to perform a polarization sensitive measurement in the 45° basis on detector D5.

Further notes on detection

The SNR from the scattered light detector D4 is significantly better than that from detectors D1,2,3. Because of this, even though the z and α peaks overlap, fitting the PSD of D4 is the most accurate method for monitoring the dynamics of the nanorod. However, we can always use the other detectors to confirm our findings. The SNR of the scattered light signal is so good because we only collect light that is scattered by the nanorod, with virtually zero background.

We expect the scattered light signal D4 to be only sensitive to the first harmonic of all motions $2f_{x,y,z,\alpha,\beta}$, since it depends on position squared. However, Fig. S2a) shows that we measure the fundamental motions $f_{z,\alpha}$ on D4. This is due to a slight misalignment between the trapping beams, and because the polarization in each arm of the trap is not perfectly identical. We confirm this through calculation, which also confirms that D4 is not sensitive to the fundamental frequency f_β.

The polarization (rather than intensity) sensitive detectors D1,5 are sensitive to the sign of the motion in α, β respectively, and so the PSDs in Fig. S2 show the frequency $f_{\alpha,\beta}$ and not its harmonic.

2. FITTING DATA

To extract trapping frequencies we fit the PSD of the scattered light time series with the function

$$\mathrm{PSD}(\omega) = C_d^2 \frac{2k_B T}{M_d} \frac{\Gamma_d}{(\omega_d^2 - \omega^2)^2 + \omega^2 \Gamma_d^2}, \qquad \textbf{(S1)}$$

where d labels the degrees of freedom (i.e. x, y, z, α, β), Γ_d is the (angular) momentum damping rate, ω_d is the trapping frequency, M_d is the particle's mass or moment of inertia and C_d is the calibration between our measured signal and absolute motional information. The derivation of this PSD is standard, e.g. [2, 3]. When recording the time series of the particle's motion, the PSD can usually be calibrated to extract C and convert from units of $\mathrm{V^2 Hz^{-1}}$ to $\mathrm{m^2 Hz^{-1}}$. However, our signal contains both translational (x, y, z) and rotational (α, β) information, so such a global calibration isn't possible. As an indication of sensitivity, the peak sensitivity for motion in the z direction from the PSD from detector D4 is $3\,\mu\mathrm{m^2/Hz^{-1}}$.

Each degree of freedom can be fit with this expression. Figure S3 shows an example of fitting the PSD. Due to the proximity of the z and α peaks in the scattered light PSD, we fit the data with a sum of two of the functions defined in Eq. S1 to extract the parameters for both the z and α motions.

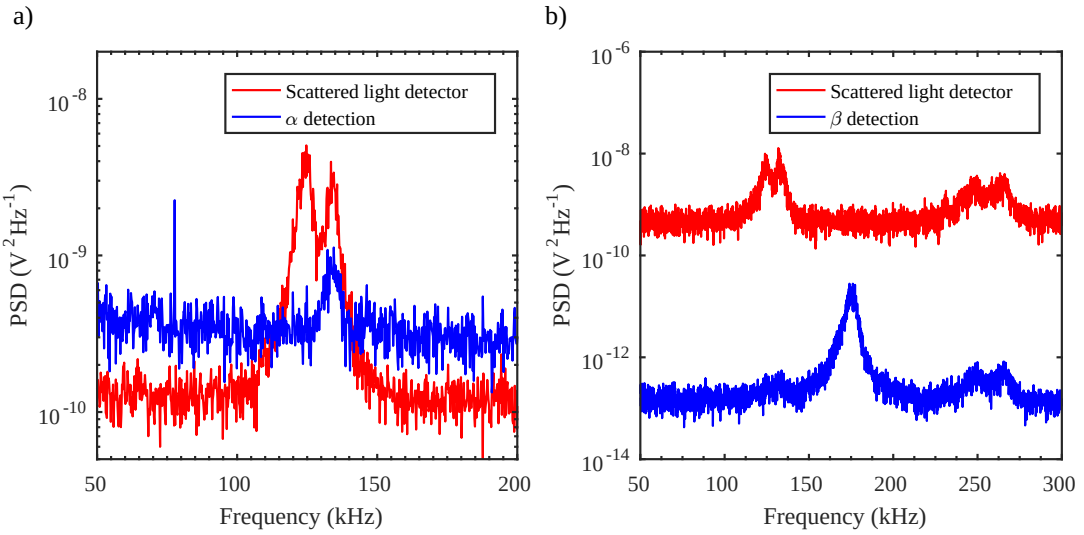

Fig. S2. a) A comparison of the PSD of the signal from the scattered light detector D4 (red), which is sensitive to motion in all directions, and the polarization sensitive detector D1 (blue), which is only sensitive to α. This confirms that the higher frequency peak corresponds to the α motion, which agrees with our calculations. b) A comparison of the PSD from the scattered light detectors D4 (red) and D5 (blue, polarization sensitive). D5 is sensitive to the frequency f_β, which isn't visible on detector D4.

3. TRAPPING FREQUENCY POWER SCALING

We expect all trapping frequencies to scale with the square root of power, see Eq. (1) of the manuscript. Figure S4 shows the measured trapping frequencies as a function of power in comparison to the theoretical expectation. The only unknown experimental parameter is the laser waist w_0, which we extract from the ratio of f_z to f_x. The ratio of f_z to f_α confirms the length of our nanorod, which agrees with scanning electron microcope images. We observe excellent agreement between theory and $f_{\alpha,z}$, and also for the axial frequency when the rod is rotating $f_{z,\mathrm{rot}}$. The discrepancy (< 5 %) between theory and experiment for f_β is attributed to the fact that the rods have finite diameter ($d = 130$ nm) and, the generalized Rayleigh-Gans approximation [4] is not strictly valid.

4. REDUCTION OF TRAPPING POTENTIAL WHEN THE PARTICLE IS ROTATING

Due to the rotation of the rod in the plane orthogonal to the trap axis, only the averaged susceptibility $(\chi_\parallel + \chi_\perp)/2$ enters the trapping potential of the translational motion in z-direction. This means that in Eq. (1) of the manuscript, $\chi_\parallel$ has to be replaced by $(\chi_\parallel + \chi_\perp)/2$. This agrees well with the measured reduction of the trapping frequency, see Fig. S4.

5. EXTRACTING INFORMATION FROM THE ROTATIONAL MOTION

When the trapping light is circularly polarized the nanorod rotates in the plane orthogonal to the trap axis (α direction) with the frequency $f_{\alpha,\mathrm{rot}}$. As shown in the paper, $f_{\alpha,\mathrm{rot}}$ has a broad distribution. To analyze this motion we extract the instantaneous frequency, using time bins 100 times longer than the mean rotational period. In the paper we present the mean value of $f_{\alpha,\mathrm{rot}}$ and display shaded regions around the data points representing the minimum and maximum values of $f_{\alpha,\mathrm{rot}}$. The theoretical analysis predicts the maximum rotation frequency $f_{\alpha,\mathrm{max}}$, which is determined by the balance between the torque exerted by the light field and the rotational friction due to collisions with gas molecules.

REFERENCES

1. S. Kuhn, P. Asenbaum, A. Kosloff, M. Sclafani, B. A. Stickler, S. Nimmrichter, K. Hornberger, O. Cheshnovsky, F. Patolsky, and M. Arndt, "Cavity-Assisted Manipulation of Freely Rotating Silicon Nanorods in High Vacuum." Nano Lett. **15**, 5604–5608 (2015).
2. Gieseler, J., Deutsch, B., Quidant, R. and Novotny, L., "Subkelvin Parametric Feedback Cooling of a Laser-Trapped Nanoparticle." Phys. Rev. Lett. **109**, 103603 (2012).
3. Millen, J., Deesuwan, T., Barker, P. F. and Anders, J., "Nanoscale temperature measurements using non-equilibrium Brownian dynamics of a levitated nanosphere." Nature Nano. **9**, 425 (2014).
4. Stickler, B. A., Nimmrichter, S., Martinetz, L., Kuhn, S., Arndt, M. and Hornberger, K., "Rotranslational Cavity Cooling of Dielectric Rods and Disks." Phys. Rev. A **94**, 033818 (2016).

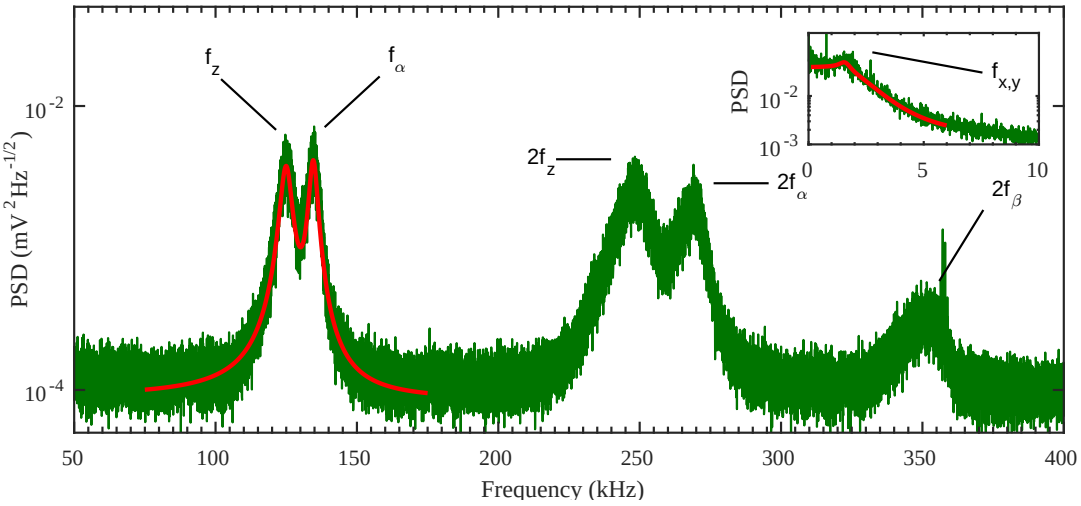

Fig. S3. The PSD of the scattered light signal showing all motional degrees of freedom. Solid red lines are fits to the data using Eq. S1.

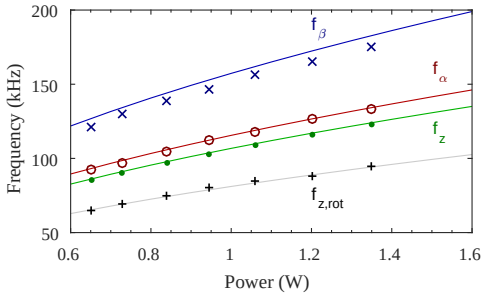

Fig. S4. Variation in the trapping frequencies with total trap power, markers are data, solid lines are the theoretical predictions. The frequency $f_{z,\mathrm{rot}}$ is the trap frequency in the z direction when the nanorod is rotating in the α direction. Experimental uncertainties are smaller than the data markers.

4.2 Reprint: Optically driven ultra-stable nanomechanical rotor

S. Kuhn et al., "Optically driven ultra-stable nanomechanical rotor," Nature Communications, 8:1670 (2017), presents the frequency locking of the mean rotation rate of a nanorod to an external drive. By switching the polarisation of the trapping field between linear and circular the rod can be prepared to undergo rotations with a stability of its mean rotation frequency $f_\mathrm{r}/\Delta f_\mathrm{r}$ of up to 7.7×10^{11}. This stability is set by the frequency stability of the drive. The coupling of the nanorod to the environment is only reflected in a phase difference between the external drive and the rotational motion of the rod. Utilizing a lock-in amplifier, this phase is used to locally measure the gas pressure.

As the leading author I conceived and designed the experiment together with J. Millen and M. Arndt, performed all measurements together with J. Millen, analysed the data together with B. A. Stickler and J. Millen and wrote the paper together with B. A. Stickler, K. Hornberger, M. Arndt and J. Millen. The theory on the chaotic dynamics of the nanorod and its stable limit cycles was developed by B. A. Stickler and K. Hornberger at the University of Duisburg-Essen. The nanorod was fabricated by A. Kosloff and F. Patolsky at Tel Aviv University.

This work is also subject to a filed patent application [201].

nature COMMUNICATIONS

ARTICLE

DOI: 10.1038/s41467-017-01902-9 OPEN

Optically driven ultra-stable nanomechanical rotor

Stefan Kuhn[1], Benjamin A. Stickler[2], Alon Kosloff[3], Fernando Patolsky[3], Klaus Hornberger[2], Markus Arndt[1] & James Millen[1]

Nanomechanical devices have attracted the interest of a growing interdisciplinary research community, since they can be used as highly sensitive transducers for various physical quantities. Exquisite control over these systems facilitates experiments on the foundations of physics. Here, we demonstrate that an optically trapped silicon nanorod, set into rotation at MHz frequencies, can be locked to an external clock, transducing the properties of the time standard to the rod's motion with a remarkable frequency stability $f_r/\Delta f_r$ of 7.7×10^{11}. While the dynamics of this periodically driven rotor generally can be chaotic, we derive and verify that stable limit cycles exist over a surprisingly wide parameter range. This robustness should enable, in principle, measurements of external torques with sensitivities better than 0.25 zNm, even at room temperature. We show that in a dilute gas, real-time phase measurements on the locked nanorod transduce pressure values with a sensitivity of 0.3%.

[1] University of Vienna, Faculty of Physics, VCQ, Boltzmanngasse 5, 1090 Vienna, Austria. [2] University of Duisburg-Essen, Lotharstraße 1, 47048 Duisburg, Germany. [3] School of Chemistry, Tel-Aviv University, Ramat-Aviv 69978, Israel. Correspondence and requests for materials should be addressed to S.K. (email: stefan.kuhn@univie.ac.at)

Frequency is the most precisely measured quantity in physics, and stable oscillators have found a plethora of applications in metrology. While pendulum clocks exploited the stability of mechanical motion to keep track of time, state-of-the-art atomic clocks rely on well-defined internal resonances of atoms, achieving a precision of a few parts in 10^{18} (ref. [1]). To exploit the stability of clocks for physical applications, it is essential to develop "gearboxes" that can be synchronized to a good time standard, translating atomic definiteness into other domains of physics. Phase-locked quartz oscillators[2] and frequency combs are examples of such transducers, imprinting clock stability onto a mechanical system or light field respectively, with high accuracy[3].

Nano- and micromechanical systems are of great technological interest, due to their low mass and extreme sensitivity to external forces[4–6], torques[7, 8], acceleration[9], displacement[10, 11], charge[12], and added mass[13, 14]. Many of these systems are themselves realizations of harmonic oscillators, with frequency stabilities reaching $f/\Delta f = 10^8$ (refs. [15, 16]), which can be further improved through mechanical engineering[17], injection locking[18, 19], electronic feedback[20], or parametric driving[21]. The contact-free mechanical motion of particles suspended by external fields in vacuum[22–29] can reach a frequency stability that is only limited by laser power fluctuations and collisional damping by residual gas particles[30].

In this work, we transduce clock stability into the rotation of an optically trapped silicon nanorod in vacuum. By periodically driving the rotation with circularly polarized light, we create a nanomechanical rotor whose rotation frequency f_r, and frequency noise, is determined by the periodic drive alone. This driven rotor is sensitive to non-conservative forces, and the operating frequency can be tuned by almost 10^{12} times its linewidth. Through our method, the frequency stability is independent of material stress, laser noise, and collisional damping. The driven nanorotor operates at room temperature, and across a wide pressure range from low vacuum to medium vacuum, achieving a pressure resolution of three parts-per-thousand, and in principle allowing a torque sensitivity below the zepto-Nm level.

Results

Frequency locking. We levitate a nanofabricated silicon nanorod in the standing light wave formed by two counterpropagating laser beams, and track its motion by monitoring the scattered light, see Fig. 1a and "Methods". When the laser is linearly polarized, the nanorod is harmonically trapped in an antinode of the standing wave and aligned with the field polarization. When the laser is circularly polarized, the scattered light exerts a torque[29, 31, 32] and propels the nanorod in the plane orthogonal to the beam axis, while its center-of-mass remains trapped[29]. The maximum rotation frequency of the rod is determined by its size, the pressure, and the laser intensity[29]. Collisions with gas particles, and center-of-mass excursions into regions of different light intensity, give rise to a broad distribution of rotational frequencies[29], as shown by the blue curve in Fig. 1c.

However, if the rod is driven by periodically switching the laser polarization between linear and circular, the rod can frequency lock to this modulation, leading to a sharp peak in the power spectral density (PSD) of the scattered light (Fig. 1b). The locked rotation peak is eleven orders of magnitude narrower than in the unlocked case (Fig. 1c). The rotation frequency can be continuously tuned over a range of 10^{12} linewidths whilst locked to the periodic drive, retaining its high frequency stability.

In order to characterize the frequency-locked rotation, we drive the nanorod with frequency $f_d = 1.11$ MHz, at a gas pressure $p_g =$ 4 mbar and total laser power $P = 1.35$ W. We record its motion

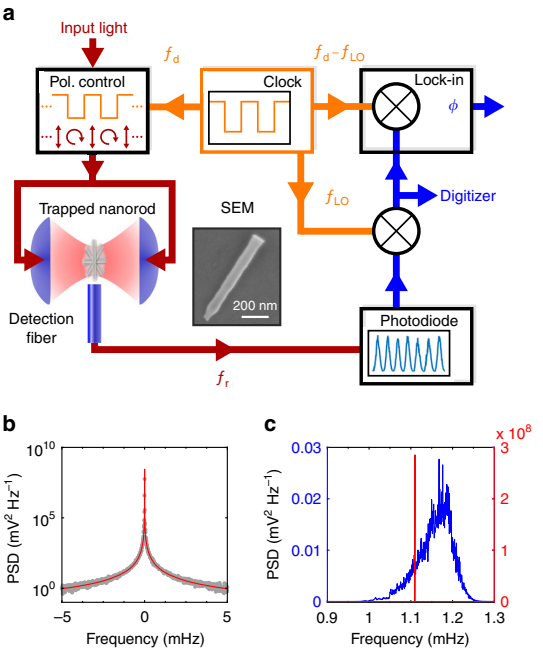

Fig. 1 Frequency locking. **a** A silicon nanorod is optically trapped in a standing wave formed by counterpropagating focussed laser beams at $\lambda =$ 1550 nm, see "Methods" section. The polarization of the light is controlled using a fiber-EOM driven by a signal generator. We detect the motion of the nanorod via the scattered light collected in a multimode optical fiber. The signal is mixed down with a local oscillator f_{LO} to record the spectrum and the phase of the rotation with respect to the drive frequency f_d. Both frequencies f_d and f_{LO} are synced to a common clock. **b** Power spectral density (gray points) of the frequency-locked rotation at 1.11 MHz, taken over 4 continuous days, fit with a Lorentzian (red curve). The upper bound on the FWHM is 1.3 μHz. **c** Comparison of driven rotation when frequency-locked ("locked rotation", red, right axis) and un-locked ("threshold rotation", blue, left axis)

continuously for four days (see "Methods" section). The PSD of the locked rotation is shown in Fig. 1b. We record an extremely narrow feature, which yields a Lorentzian FWHM below 1.3 μHz within one standard deviation. In this way, we achieve rotational stability with a phase noise −80 dBc Hz^{-1} below the signal at only 3 mHz from the carrier frequency (Fig. 2).

Stable limit cycles. To explain this ultra-stable rotation, we model the dynamics of the rod's orientation α with respect to the polarization axis[29]. Denoting by Γ the damping rate due to gas collisions (a function of gas pressure p_g), by N the torque exerted by the circularly polarized standing wave (a function of laser power P) and by V the maximum potential energy of the rod in a linearly polarized standing wave, the equation of motion is

$$\ddot{\alpha} = -\Gamma\dot{\alpha} + \frac{N}{I}h(t) - \frac{V}{I}\sin(2\alpha)[1 - h(t)], \qquad (1)$$

where $I = M\ell^2/12$ is the moment of inertia and $h(t)$ represents the periodic driving, with $h(t) = 1$ for circular polarization at $t \in [0, 1/2f_d)$ and $h(t) = 0$ for linear polarization at $t \in [1/2f_d, 1/f_d)$; expressions for Γ, N, and V are given in "Methods" section.

NATURE COMMUNICATIONS | DOI: 10.1038/s41467-017-01902-9 ARTICLE

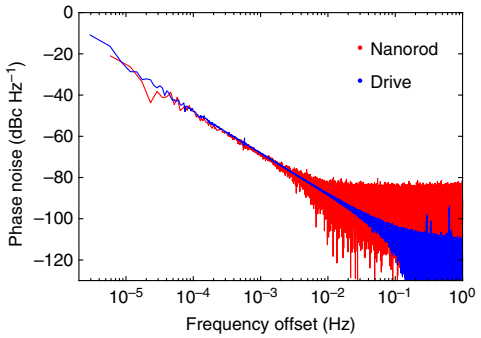

Fig. 2 Characterizing the locked rotation. The phase noise of the rotor (red) and drive (blue) is calculated from two individual four day measurements at a drive frequency of $f_d = 1.11$ MHz (see "Methods" section)

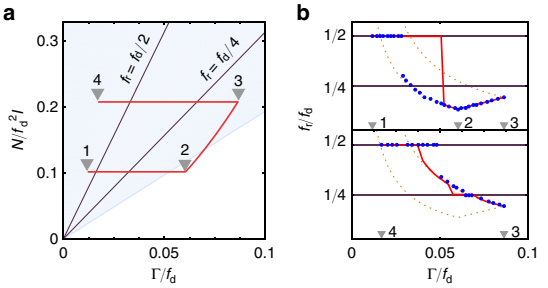

Fig. 3 Driven rotor. **a** Reduced parameter space for the periodically driven nanorod. Different regions can exhibit different limit cycles, as determined by the initial conditions. Within the blue shaded region f_r:$f_d = 1$:2–locking can occur, while it can not be realized in the white region. Along the labeled solid lines the frequency of threshold rotation coincides with 1:2– or 1:4–locking. To explore the various limit cycles we select a path in parameter space (solid red line) which we follow experimentally by adiabatically varying p_g and f_d. **b** Experimentally measured rotation frequencies f_r along the path in parameter space (blue points), and simulation (solid red line). The three different limit cycles observed are: threshold rotation (orange dotted lines), 1:2– and 1:4–locking (horizontal solid lines)

In the limit of long driving times $t \gg 1/f_d$ the nanorod rotates with constant mean rotation frequency $f_r = \langle\dot{\alpha}\rangle/2\pi$, and its motion approaches one of two qualitatively distinct types of limit cycles. In the first type, threshold rotation, $f_r = N/(4\pi I\Gamma)$ is determined by the balance between Γ and the time averaged radiation torque $N/2$. Threshold rotation exhibits a broad frequency distribution, as shown by the blue curve in Fig. 1c, due to its dependence on P and p_g[29]. It should be noted, that the behavior of threshold rotation is almost identical to illuminating the nanorotor continuously with circularly polarized light, which propels the rod at a maximum rotation frequency $f_r = N/(2\pi I\Gamma)$.

In the second type of limit cycle, the aforementioned locked rotation, f_r locks to a rational fraction of the driving frequency. Experimentally, we observe f_r:$f_d = 1$:2– and f_r:$f_d = 1$:4–locking, where the rod performs one rotation in two or four driving periods, respectively. The rotational frequency f_r now does not depend on environmental parameters such as p_g or P, but only on the frequency stability of the drive. Locked rotation is shown in Fig. 1b and the red curve in Fig. 1c.

The realized limit cycle is determined by the initial dynamics of the nanorod, and by experimental parameters such as p_g, P, f_d, and the rod dimensions. For a given nanorod the ratio between torque and potential is fixed, and thus Eq. (1) depends only on the dimensionless damping rate Γ/f_d and dimensionless torque $N/f_d^2 I$. In Fig. 3a we show this reduced parameter space. The blue shaded area indicates the region where 1:2–locking is possible. The labeled solid lines indicate where threshold and locked rotations have the same frequency, and locking occurs independent of the initial conditions.

Rotational dynamics. To explore the dynamics of the driven nanorotor, we experimentally vary p_g and f_d, thereby following a path through parameter space (red line in Fig. 3a). The observed f_r are shown as blue points in Fig. 3b, the top panel showing the path 1–2–3, and the lower panels 3–4. This plot shows that for certain parameters both types of limit cycles can be observed, depending on the initial conditions. When starting from 1, the rotation 1:2–locks to the drive (horizontal solid line). When increasing p_g along 1–2, the rod jumps out of lock, and exhibits threshold rotation. When decreasing f_d along 2–3, the rod remains at threshold rotation, following the theoretically expected frequencies with excellent agreement (orange dotted lines). Decreasing p_g along 3–4, the rod first follows the threshold rotation frequency until it crosses the horizontal line, where it briefly enters 1:4–locked rotation, returns to threshold rotation and eventually jumps into 1:2–locked rotation. The solid red lines in Fig. 3b are the theoretically predicted f_r for an adiabatic path through parameter space, with the discrepancy due to imperfect adiabatic control in the experiment.

Applications. For 1:2–locked rotation, the phase lag ϕ between the drive and the rotation is

$$\phi = \arccos\left[\frac{\pi}{2V}\left(N - 2\pi f_d I\Gamma\right)\right]; \qquad (2)$$

it depends upon gas pressure p_g through Γ and on laser power P through V and N. The requirement that this phase is real defines the shaded region in Fig. 3a. The phase ϕ is sensitive to non-conservative forces, such as light or gas scattering.

A lock-in amplifier is used to monitor ϕ (see "Methods" section), yielding real-time readout of phase variations. For a constant laser power P, measuring the phase amounts to local sensing of the gas pressure p_g, as shown in Fig. 4b. We achieve a relative pressure sensitivity of 0.3%, which is currently limited only by the intensity noise of the fiber amplifier. This sensitivity may still be improved by five to six orders of magnitude by stabilizing the power[33]. This shows the great potential of our system as a pressure sensor. The fine spatial resolution provided by the micrometer-sized rotor could allow, for instance, mapping of velocity fields and turbulences in rarefied gas flows or atomic beams.

The driven nanorod is sensitive to externally applied torques through Eq. (1). In analogy to the pressure sensing application, the phase between the drive and the driven rotation of the locked rotor provides a real-time readout with a bandwidth of 100 kHz set by the lock-in amplifier. From Eq. (2), the torque sensitivity can be estimated as 2.4×10^{-22} Nm for our current experimental parameters, which at room temperature would be the highest value achieved in state of the art systems[8], and which could also be significantly improved by laser power stabilization. This sensitivity can be reached for any non-conservative force, that varies on a timescale longer than $1/f_d$. The bandwidth and sensitivity of this sensor for arbitrary torques warrants further investigation.

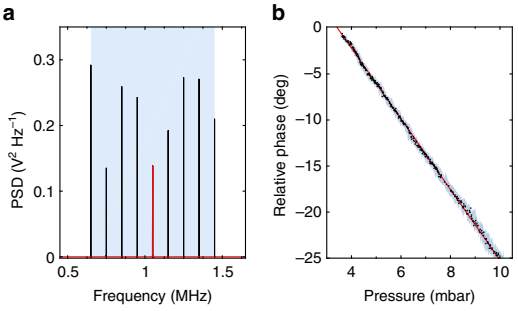

Fig. 4 Sensing applications. **a** At 4 mbar, the locking frequency f_d can be continuously tuned by over 800 kHz, which corresponds to almost 10^{12} linewidths. The peaks in the PSD differ in amplitude since for short recording times they are not fully resolved. **b** In this parameter region the phase lag (black dots) between the rotor and the drive depends linearly on pressure (fitted red line) and thus can be used for precise pressure sensing. The pressure values are given by the reading of a commercial pressure Gauge (Pfeiffer Vacuum PCR 280), and the shaded region is the error margin as defined by the manufacturer-given resolution and repeatability of the Gauge

Discussion

In conclusion, we have presented a technique for locking the rotation of a levitated nanomechanical rotor to a stable frequency reference, leading to a high mechanical frequency stability which can be used for instantaneous, highly sensitive local measurements of pressure or torque. One great advantage of the locked nanorotor over nanomechanical resonators is the absence of an intrinsic resonance frequency. By varying f_d we can tune the rotation frequency over almost 10^{12} linewidths while retaining its stability, as shown in Fig. 4a, circumventing the low bandwidth that naturally comes with highly sensitive resonant detectors. Measuring a phase lag rather than a frequency shift allows us to monitor force variations in real time, bypassing the inherent growth in measurement time that comes with decreasing linewidth in a resonant sensor.

Our system is sensitive to non-conservative forces, such as those due to photon absorption or emission, shear forces in gas flows, radiation pressures in light fields, optical potentials, mass and size variations of the rod due to gas accommodation, and local pressure and temperature variations in the gas. Employing higher optical powers, larger duty cycles of the drive, or lower gas pressures will increase the sensing range by a factor of more than ten, while retaining the exquisite sensitivity. The stability of the locked nanorotor may be further increased by driving it with a more stable clock. By reaching ultra high vacuum, this technique may also be suited to prepare quantum coherent rotational dynamics[34], for which the high frequency stability may be exploited.

Methods

Nanorod trapping. A silicon nanorod of length $\ell = (725 \pm 15)$ nm and diameter $d = (130 \pm 13)$ nm (with mass $M = 2.2 \times 10^{-17}$ kg) is trapped at a pressure of $p_g = 4$ mbar, using light of total power $P = 1.35$ W with RMS power fluctuations of 0.3%. Our method of producing and trapping the nanorods is described in refs. [29, 35]. The motion is monitored by placing a 1 mm core multimode fiber less than 100 µm from the trapped nanorod, which collects the light that the nanoparticle scatters, yielding information about all translational and rotational degrees of freedom.

Rotation analysis. In order to record a time series as long as 4 days we mix down the scattered light with a local oscillator at frequency f_{LO} such that the rotational motion signal of the rod is shifted to a frequency of 190 Hz (Fig. 1a) and digitized with a sampling rate of 2 kS s^{-1}. This signal can then be used to calculate the phase noise $S_\phi(f) = 10\log_{10}[\mathrm{PSD}(f)/\mathrm{PSD}(f_d)]$ in units of dBc Hz^{-1}. The drive signal is recorded and analyzed in the same way.

To extract the relative phase ϕ of the nanorod rotation with respect to the drive we use a Stanford Research Systems lock-in amplifier (SR830) which performs a homodyne measurement on the mixed-down 190 Hz scattering signal. For this purpose both the modulation frequency f_d and the local oscillator f_{LO} are synced to a common clock.

Rotational dynamics. The rotational motion depends crucially on the damping rate Γ, the radiation torque N, and the laser potential V, through Eq. (1). All three quantities can be evaluated microscopically as detailed in refs. [29, 36]. Specifically, the rotational damping rate due to diffuse reflection of gas atoms with mass m_g, evaluated in the free molecular regime, is $\Gamma = d\ell p_g\sqrt{2\pi m_g}(6+\pi)/8M\sqrt{k_B T}$, where T denotes the gas temperature. The optical torque exerted by a circularly polarized standing wave can be evaluated by approximating the internal polarization field according to the generalized Rayleigh–Gans approximation[36] as $N = P\Delta\chi\ell^2 d^4 k^3[\Delta\chi\eta_1(k\ell) + \chi_\perp\eta_2(k\ell)]/48cw_0^2$, where $k = 2\pi/\lambda$ is the wavenumber, $\Delta\chi = \chi_\parallel - \chi_\perp$ depends on the two independent components of the susceptibility tensor and $\eta_1(k\ell) = 0.872$ and $\eta_2(k\ell) = 0.113$[29]. In a similar fashion, one obtains for the laser potential $V = Pd^2\ell\Delta\chi/2cw_0^2$.

The phase lag (2) is obtained by averaging the equation of motion (1) over one driving period $1/f_d$ and exploiting that the motion is 1:2-locked, $\langle\dot\alpha\rangle = \pi f_d$ while $\langle\ddot\alpha\rangle = 0$ and, consequently, $\alpha(t) = \alpha_0 + \pi f_d t$. The phase difference between the polarization change from circular to linear and the maximum scattering signal observed when the rod is oriented orthogonal to the detector ($\alpha(t) = \pi$) is $\phi = \pi - 2\alpha_0$ leading to Eq. (2).

Data availability. All relevant data are available from the corresponding author upon request.

Received: 17 January 2017 Accepted: 25 October 2017
Published online: 21 November 2017

References

1. Ludlow, A. D., Boyd, M. M., Ye, J., Peik, E. & Schmidt, P. O. Optical atomic clocks. *Rev. Mod. Phys.* **87**, 637–701 (2015).
2. Vig, J. R. *Quartz crystal oscillators and resonators*. Technical Report No. SLCET-TR-88-1 (Army Research Laboratory, Fort Monmouth, NJ, USA 1999).
3. Udem, T., Holzwarth, R. & Hänsch, T. W. Optical frequency metrology. *Nature* **416**, 233–237 (2002).
4. Mamin, H. J. & Rugar, D. Sub-attonewton force detection at millikelvin temperatures. *Appl. Phys. Lett.* **79**, 3358–3360 (2001).
5. Gavartin, E., Verlot, P. & Kippenberg, T. J. A hybrid on-chip optomechanical transducer for ultrasensitive force measurements. *Nat. Nanotechnol.* **7**, 509–514 (2012).
6. Ranjit, G., Atherton, D. P., Stutz, J. H., Cunningham, M. & Geraci, A. A. Attonewton force detection using microspheres in a dual-beam optical trap in high vacuum. *Phys. Rev. A* **91**, 051805 (2015).
7. Kim, P. H. et al. Nanoscale torsional optomechanics. *Appl. Phys. Lett.* **102**, 053102 (2013).
8. Kim, P. H., Hauer, B. D., Doolin, C., Souris, F. & Davis, J. P. Approaching the standard quantum limit of mechanical torque sensing. *Nat. Commun.* **7**, 13165 (2016).
9. Krause, A. G., Winger, M., Blasius, T. D., Lin, Q. & Painter, O. A high-resolution microchip optomechanical accelerometer. *Nat. Photonics* **6**, 768–772 (2012).
10. Teufel, J. D., Donner, T., Castellanos-Beltran, M. A., Harlow, J. W. & Lehnert, K. W. Nanomechanical motion measured with an imprecision below that at the standard quantum limit. *Nat. Nanotechnol.* **4**, 820–823 (2009).
11. Wilson, D. J. et al. Measurement-based control of a mechanical oscillator at its thermal decoherence rate. *Nature* **524**, 325–329 (2015).
12. Cleland, A. & Roukes, M. A nanometre-scale mechanical electrometer. *Nature* **392**, 160–162 (1998).
13. Chaste, J. et al. A nanomechanical mass sensor with yoctogram resolution. *Nat. Nanotechnol.* **7**, 301–304 (2012).
14. Liu, F., Alaie, S., Leseman, Z. C. & Hossein-Zadeh, M. Sub-pg mass sensing and measurement with an optomechanical oscillator. *Opt. Express* **21**, 19555–19567 (2013).
15. Norte, R. A., Moura, J. P. & Gröblacher, S. Mechanical resonators for quantum optomechanics experiments at room temperature. *Phys. Rev. Lett.* **116**, 147202 (2016).
16. Tsaturyan, Y., Barg, A., Polzik, E. S. & Schliesser, A. Ultra-coherent nanomechanical resonators via soft clamping and dissipation dilution. *Nat. Nanotechnol.* **12**, 776–783 (2017).

17. Ghaffari, S. et al. Quantum limit of quality factor in silicon micro and nano mechanical resonators. *Sci. Rep.* **3**, 3244 (2014).
18. Hossein-Zadeh, M. & Vahala, K. J. Observation of injection locking in an optomechanical RF oscillator. *Appl. Phys. Lett.* **93**, 191115 (2008).
19. Coppock, J. E., Nagornykh, P., Murphy, J. P. J. & Kane, B. E. Phase locking of the rotation of a graphene nanoplatelet to an RF electric field in a quadrupole ion trap. In *Proc. SPIE 9922, Optical Trapping and Optical Micromanipulation XIII* 99220E (2016).
20. Feng, X. L., White, C. J., Hajimiri, A. & Roukes, M. L. A self-sustaining ultrahigh-frequency nanoelectromechanical oscillator. *Nat. Nanotechnol.* **3**, 342–346 (2008).
21. Villanueva, L. G. et al. A nanoscale parametric feedback oscillator. *Nano Lett.* **11**, 5054–5059 (2011).
22. Cirio, M., Brennen, G. K. & Twamley, J. Quantum magnetomechanics: ultrahigh-q-levitated mechanical oscillators. *Phys. Rev. Lett.* **109**, 147206 (2012).
23. Gieseler, J., Deutsch, B., Quidant, R. & Novotny, L. Subkelvin parametric feedback cooling of a laser-trapped nanoparticle. *Phys. Rev. Lett.* **109**, 103603 (2012).
24. Yin, Z.-Q., Geraci, A. A. & Li, T. Optomechanics of levitated dielectric particles. *Int. J. Mod. Phys. B* **27**, 1330018 (2013).
25. Kiesel, N. et al. Cavity cooling of an optically levitated submicron particle. *Proc. Natl Acad. Sci. USA* **110**, 14180–14185 (2013).
26. Neukirch, L. P. & Vamivakas, A. N. Nano-optomechanics with optically levitated nanoparticles. *Contemp. Phys.* **56**, 48–62 (2014).
27. Millen, J., Fonseca, P. Z. G., Mavrogordatos, T., Monteiro, T. S. & Barker, P. F. Cavity cooling a single charged levitated nanosphere. *Phys. Rev. Lett.* **114**, 123602 (2015).
28. Hoang, T. M. et al. Torsional optomechanics of a levitated nonspherical nanoparticle. *Phys. Rev. Lett.* **117**, 123604 (2016).
29. Kuhn, S. et al. Full rotational control of levitated silicon nanorods. *Optica* **4**, 356–360 (2017).
30. Chang, D. E. et al. Cavity opto-mechanics using an optically levitated nanosphere. *Proc. Natl Acad. Sci. USA* **107**, 1005–1010 (2010).
31. Tong, L., Miljković, V. D. & Käll, M. Alignment, rotation, and spinning of single plasmonic nanoparticles and nanowires using polarization dependent optical forces. *Nano Lett.* **10**, 268–273 (2009).
32. Arita, Y., Mazilu, M. & Dholakia, K. Laser-induced rotation and cooling of a trapped microgyroscope in vacuum. *Nat. Commun.* **4**, 2374 (2013).
33. Kwee, P., Willke, B. & Danzmann, K. New concepts and results in laser power stabilization. *Appl. Phys. B* **102**, 515–522 (2011).
34. Shi, H. & Bhattacharya, M. Optomechanics based on angular momentum exchange between light and matter. *J. Phys. B: At. Mol. Opt. Phys.* **49**, 153001 (2016).
35. Kuhn, S. et al. Cavity-assisted manipulation of freely rotating silicon nanorods in high vacuum. *Nano Lett.* **15**, 5604–5608 (2015).
36. Stickler, B. A. et al. Ro-translational cavity cooling of dielectric rods and disks. *Phys. Rev. A* **94**, 033818 (2016).

Acknowledgements

We are grateful for financial support by the Austrian Science Fund (FWF) in the projects P27297 and DK-CoQuS (W1210). We acknowledge support by S. Puchegger and the faculty center for nanostructure research at the University of Vienna in imaging the nanorods. J.M. acknowledges funding from the European Unions Horizon 2020 research and innovation program under the Marie Skłodowska-Curie grant agreement no. 654532. F.P. acknowledges the Legacy Program (Israel Science Foundation) for its support.

Author contributions

S.K., M.A. and J.M. conceived of and designed the experiment. S.K. and J.M. performed all experiments. S.K., B.A.S. and J.M. analyzed the data. A.K. and F.P. fabricated the nanorods. B.A.S. and K.H. developed all theoretical models. S.K., B.A.S., K.H., M.A. and J.M. contributed to the writing of the manuscript.

Additional information

Competing interests: Aspects of this work are subject to a filed patent application.

5 Conclusion and Outlook

In this cumulative thesis I have explored novel experimental techniques to facilitate future high-mass matter-wave interferometry experiments with silicon nanoparticles. These techniques include laser-induced volatilisation methods in high-vacuum, the detection and strong coupling of nanoparticles in silicon based open-access microcavities, a theoretical study on cavity cooling of the ro-translational motion of nanoparticles, and experiments involving the rotational degrees of freedom of silicon nanorods, freely propagating in high vacuum or levitated in an optical dipole trap. They have been presented in five publications. In addition, I have discussed the feasibility of nanoparticle interferometry with masses up to 10^7 atomic mass units by adapting the scheme proposed in Reference [73] and estimated the influence of a variety of potential decoherence sources and the implications for testing the CSL model. All of these aspects will be of great importance to facilitate high-mass matter-wave interferometry with nanoparticles for which cooling of all motional degrees of freedom will be necessary to prevent decoherence and dephasing [99].

In the future, both interferometry and nanoparticle cooling experiments will benefit from advanced nanoparticle sources, based on frozen cryogenic matrices [185], which are currently being developed. There, the basic idea relies on depositing single nanoparticles on top of a frozen matrix, e.g. Argon at $T < 80\,\mathrm{K}$ [185]. The deposition of the particles can be performed with LIAD, which has been demonstrated to work for nanoparticles down to 30 nm in diameter, as shown in Section 2.1. In the next step, we will heat the particles with a focussed laser beam which melts them out of the matrix and guides them into the desired region within the experiment. The particles will, therefore, not only exhibit internal temperatures below room temperature, but also their thermal center of mass velocities will be on the order of 0.1 m/s. This will facilitate two-mode cooling to below 50 mK in dedicated microcavities, as discussed in Sections 3.1.2 and 3.2, and thereby enable matter-wave interferometry with 10^7 amu particles, as proposed in Chapter 1.

To cool particles as small as 12 nm in radius or 10^7 amu in mass, microcavities with smoother surfaces and better controlled mirror shapes have to be developed and implemented. Currently, a second generation of parabolically shaped, strongly curved micromirrors is being coated to reach cavity finesses of up to 200,000. This will enable nanoparticle cooling of masses below 10^8 amu. A third generation of micromirror chips will be targeted at radii of curvature around 20 μm, cavity lengths around 30 μm, and

finesses of more than 200,000 to enable cooling of particles below 10^7 amu and facilitate matter-wave interferometry, as proposed in Chapter 1.

To advance rotational optomechanics experiments, a new setup is currently being implemented, in which nanorods will be ro-translationally cooled via feedback and cavity cooling techniques in a crossed tweezer-cavity setup. In a first step, parametric feedback methods will allow us to cool and stabilize the motion of the rods in order to reach high vacuum while keeping them trapped. This will include parametric feedback onto the power and the polarisation of the trapping field to address both the COM and the librational motion of the rod. In a second stage, a high finesse cavity will cool the ro-translational motion towards the quantum regime. While the harmonically trapped librational motion is still linear and comparable to conventional levitated optomechanical systems, by harmonically ramping down the optical potential, the particle can be released and the non-linear motion of the free rotor will allow us to observe novel quantum features, such as the quantization of angular momentum and revivals of the wavefunction. Tailoring the dimensions of the rods via nanofabrication to achieve high, well separated mechanical trapping frequencies will be of great benefit for cooling. Future microcavities may even enable us to interact with the rotational degrees of freedom of a tobacco mosaic virus (300 nm length, 16 nm diameter) or carbon nanotubes, for which UHV compatible volatilisation methods still need to be developed.

Advancing the control over the ro-translational motion will facilitate measurements of angular momentum diffusion [196] and heating rates due to collisions with gas molecules or photon scattering [202]. In this way, the CSL model (see Section 1.2.2), could be tested in the ro-translation degrees of freedom [203]. Coupling a cooled, anisotropic particle to Laguerre-Gauss beams with orbital angular momentum could allow us to transfer multiple $\hbar$ of angular momentum per photon, and enable experiments to prepare and probe superpositions of angular momentum states while keeping scattering low [133, 190, 204]. The alignment and stabilisation of non-spherical particles containing internal quantum systems, e.g. silicon or nitrogen vacancy centers in nano-diamonds, will be crucial for future spin-resonance and magnetometry experiments [145, 205].

Ro-translationally cold, elongated particles may enable high-mass matter-wave interferometry experiments beyond 10^7 amu, where the anisotropy will facilitate strong coherent beam-splitting mechanisms and orientation dependent interference effects [186, 187]. An array of collectively cooled nanorods may also be exploited to realize a levitated grating for matter-wave interferometry with atoms or molecules. By monitoring their momentum transfer to the nanorods one may be able to realize experiments motivated by the Bohr-Einstein debates.

Appendices

A Material properties and interferometer parameters

Figure A.1 shows the index of refraction and extinction coefficient for bulk silicon as a function of wavelength.

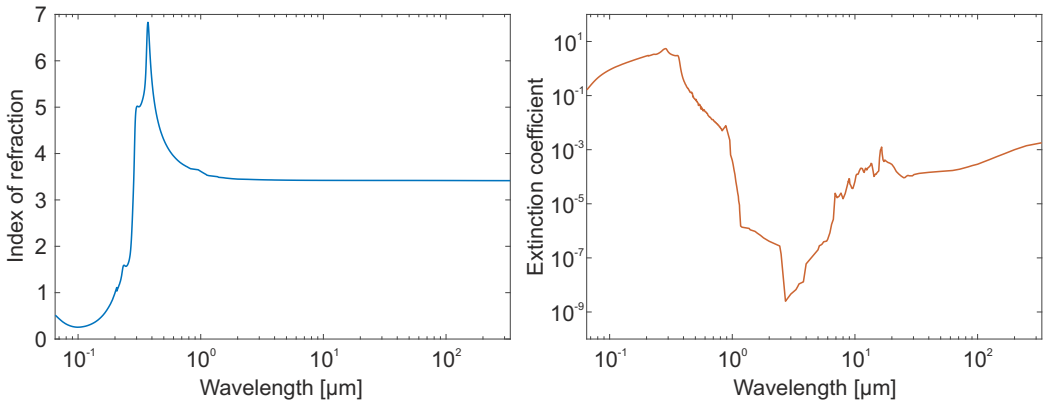

Figure A.1: Index of refraction and extinction coefficient for bulk silicon. All values taken from Reference [206]. Missing data-points were obtained by linear interpolation. This data serves to calculate decoherence rates due to the absorption and emission of thermal photons or scattering (see Section 1.3.3).

Table A.1 lists the coefficients n and k of the dielectric function $\varepsilon(\omega) = (n + ik)^2$, the polarizability α, and the material parameter β (see section 1.3.2).

Wavelength	157 nm	213 nm	266 nm	355 nm	1550 nm
n	0.478	1.119	1.831	5.65	3.478
k	2.0	3.025	4.426	3.02	$< 1 \cdot 10^{-6}$
Polarizability α/R^3	$4\pi\varepsilon_0 \cdot 1.78$	$4\pi\varepsilon_0 \cdot 1.22$	$4\pi\varepsilon_0 \cdot 1.09$	$4\pi\varepsilon_0 \cdot 0.958$	$4\pi\varepsilon_0 \cdot 0.787$
β Parameter	0.474	0.207	$9.57 \cdot 10^{-2}$	$6.00 \cdot 10^{-2}$	$\sim 1 \cdot 10^{-7}$

Table A.1: Optical properties of silicon at $\lambda_{\text{grating}} = 157\,\text{nm}$, 213 nm, 266 nm, and 355 nm and the cavity wavelength 1550 nm. All values are taken from Reference [206].

Table A.2 lists the optimised interferometer parameters for a phase grating at grating wavelengths of 157 nm, 213 nm, 266 nm, and 355 nm, or a phase + ionization grating for 157 nm and 213 nm, as discussed in Section 1.3.2.

Wavelength λ_{grating}	157 nm	213 nm	266 nm	355 nm
$\mathbf{m = 1 \times 10^6}$ amu				
t_{T} [ms]	15.6	28.7	44.8	79.7
t_1 [ms]	31.2	57.4	89.5	159.4
L_1 [cm]	0.48	1.62	3.93	12.5
t_2 [ms] (phase/ion)	26.0 / 26.0	41.3 / 44.5	72.8	128.7
L_2 [cm] (phase/ion)	1.13 / 1.13	3.16 / 3.48	9.00	28.3
t_{tot} [ms] (phase/ion)	57.2 / 57.2	98.7 / 101.9	162.3	288.1
L_{tot} [cm] (phase/ion)	1.61 / 1.60	4.78 / 5.09	12.9	40.7
Optimal pulse energy $E_{\text{G}}[\mu\text{J}]$ (phase/ion)	120.3 / 115.5	183.2 / 173.8	247.3	282.6
$\mathbf{m = 1 \times 10^7}$ amu				
t_{T} [ms]	156	287	447.6	797.2
t_1 [ms]	312	574	895.2	1594.4
L_1 [cm]	47.7	161.6	393.1	1246.9
t_2 [ms] (phase/ion)	260.3 / 260.0	413.1 / 444.8	728.2	1287.0
L_2 [cm] (phase/ion)	112.9 / 112.7	316.3 / 347.5	899.6	2825.6
t_{tot} [ms] (phase/ion)	572.1 / 571.9	987.1 / 1018.7	1623.4	2881.4
L_{tot} [cm] (phase/ion)	160.6 / 160.4	477.9 / 509.1	1292.6	4072.5
Optimal pulse energy $E_{\text{G}}[\mu\text{J}]$ (phase/ion)	12.0 / 11.5	18.3 / 17.4	24.7	28.3
n_0 at optimal E_{G} and $a_{\text{G}} = \pi \times 50^2\,\text{mm}^2$ (phase/ion)	3.57 / 3.42	1.62 / 1.54	0.91	0.57
Periodicity of the interference pattern D [nm] (phase/ion)	144 / 144	183 / 189	241	321

Table A.2: Optimized interferometer parameters for nanoparticle masses of 1×10^6 amu and 1×10^7 amu, at various grating wavelengths (assuming an absorptive phase grating). For $\lambda_{\text{grating}} = 157\,\text{nm}$ and 213 nm the different parameters for both cases of an absorptive phase grating or a phase + ionizing grating are listed.

B Velocity Distributions of nanoparticles in free flight

B.1 Silica nanoparticles

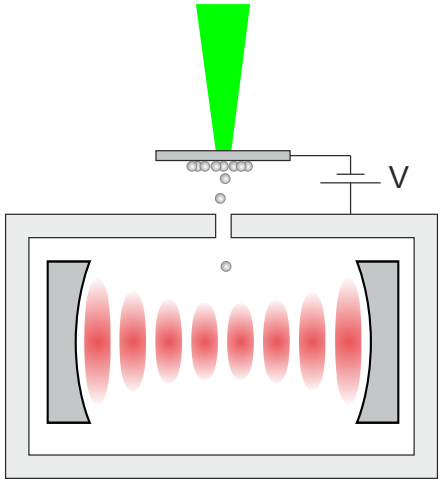

Figure B.1: Detecting free nanoparticles through scattering. Particles are launched into UHV ($< 10^{-8}$ mbar) as described in section 2.1. They need to pass a cylindrical aperture of 4 mm length and 500 μm diameter before they enter the field of an externally pumped high-finesse optical cavity. When the particles couple to the cavity mode they scatter a portion of the light into free space. Time resolved detection of this light reveals information of the particle's position and velocities (see Section 2.2), and in case of nanorods also their angular velocity (see Publication 2.4). An electric field between the sample substrate and the block containing the cavity can be applied to manipulate charged particles.

Electric fields

Particles launched via LIAD are known to carry a wide distribution of charges, ranging from neutral to ±300 elementary charges [110]. We employ electric fields to test whether charged particles can be pre-slowed before entering the cavity to increase the interaction time between the particles and the optical field and enhance the cavity cooling performance. A potential difference V is applied between the block housing

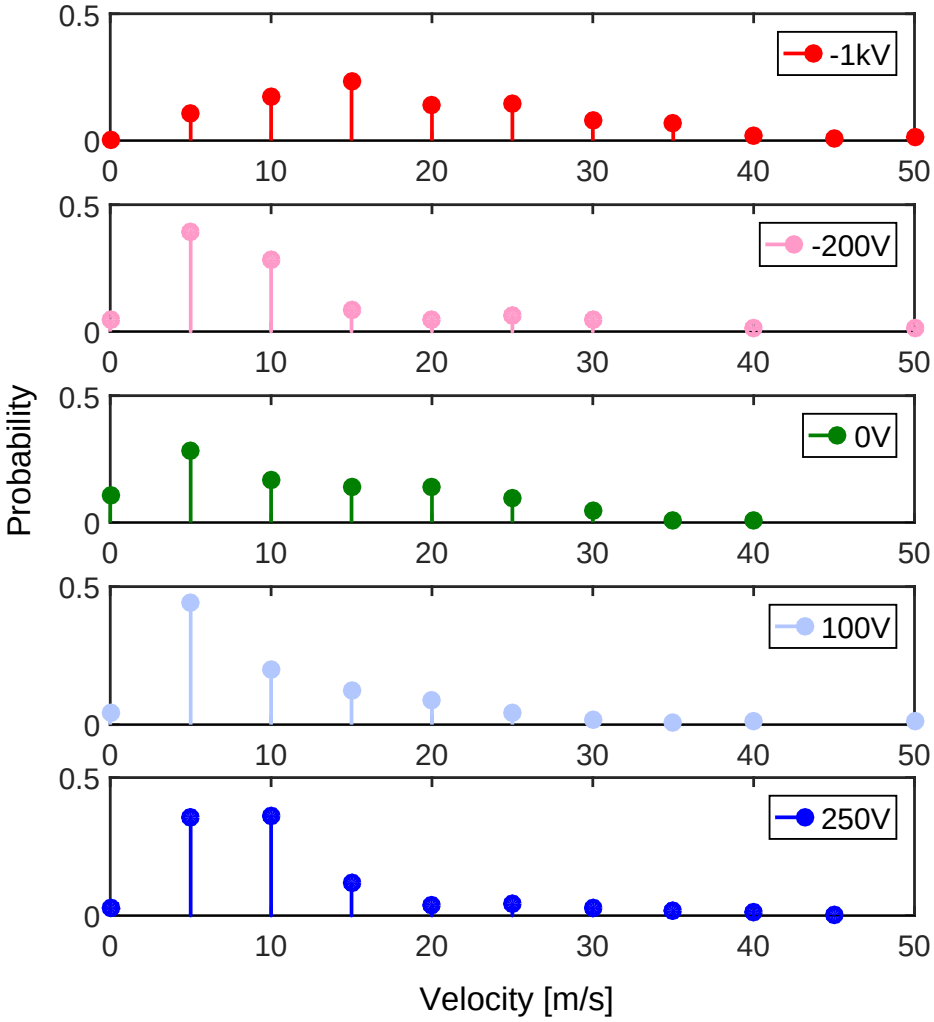

Figure B.2: Influence of an electric field on the velocity distribution of 300 nm diameter silica spheres. Particles with forward velocities $v_x > 20\,\mathrm{m/s}$ can be filtered out by applying small voltages with either polarity. High negative potential differences accelerate the particles and shift their mean velocity to approximately 15 m/s. At high positive voltages the cavity becomes unstable whenever a laser pulse impinges the sample surface. This might be explained by laser pulses ejecting electrons from the sample surface which are accelerated onto the cavity block.

the cavity and the sample surface, as shown in Figure B.1. Figure B.2 shows the velocity distribution of 300 nm diameter silica spheres launched from a 200 μm thick aluminium substrate, measured in the cavity for potential differences of -1000 V, -200 V, 0 V, +100 V and +250 V. While particles with high forward velocities can be filtered out at -200 V, +100 V and +250 V, at higher potential differences the particles get accelerated. The abundance of particles at velocities $v_x < 1\,\mathrm{m/s}$, however, is highest if both the sample and the cavity block are connected to common ground. In addition, we observe that for a high positive potential difference $V > 500\,\mathrm{V}$ the cavity gets extremely unstable when the pulse laser hits the sample surface, which could be attributed to electrons that are ejected from the sample material and accelerated onto the cavity block.

At 0 V potential difference, it turns out that particle clusters are frequently deposited onto the cavity mirrors at the position of the optical mode. This contamination results in a substantial drop of the cavity finesse due to scattering losses. Since the cylindrical aperture (0.5 mm diameter, 4 mm length) of the cavity block (see Fig. B.1) geometrically prohibits the particles from reaching the central mirror spot, we conclude that those clusters of particles carry charges and are attracted to the charged dielectric surfaces of the cavity mirrors. To reduce the probability of such events for LIAD, we apply a potential difference of -200 V.

Sample substrates

We deposit silica nanospheres on various substrate materials with different thicknesses to test the influence of the binding potential between the particles and the supporting substrate on the velocity of the launched particles. For this purpose we have tested a 500 μm silicon wafer, 200 μm & 600 μm aluminium, and 12, 5 μm titanium foil. Figure B.3 shows the velocity distribution of 300 nm silica particles launched from these surfaces. The slowest forward velocities and highest particle yield can be achieved with 200 μm thick aluminium substrates.

B.2 Nanodiced silicon particles

Nanofabricated silicon particles [103] are patterned and deposited on various sample surfaces, as described in Section 2.2.2. We measure their velocity distribution after LIAD by the same means as for silica particles. Figure B.4 shows the results for two different sample materials and potential differences. While this method allows to launch single silicon particles from well-defined initial positions, the velocity distribution shows that a softer launching mechanism is necessary to achieve velocities required for both cooling and interferometry experiments, raising the need for cryogenic sources (see Chapter 5).

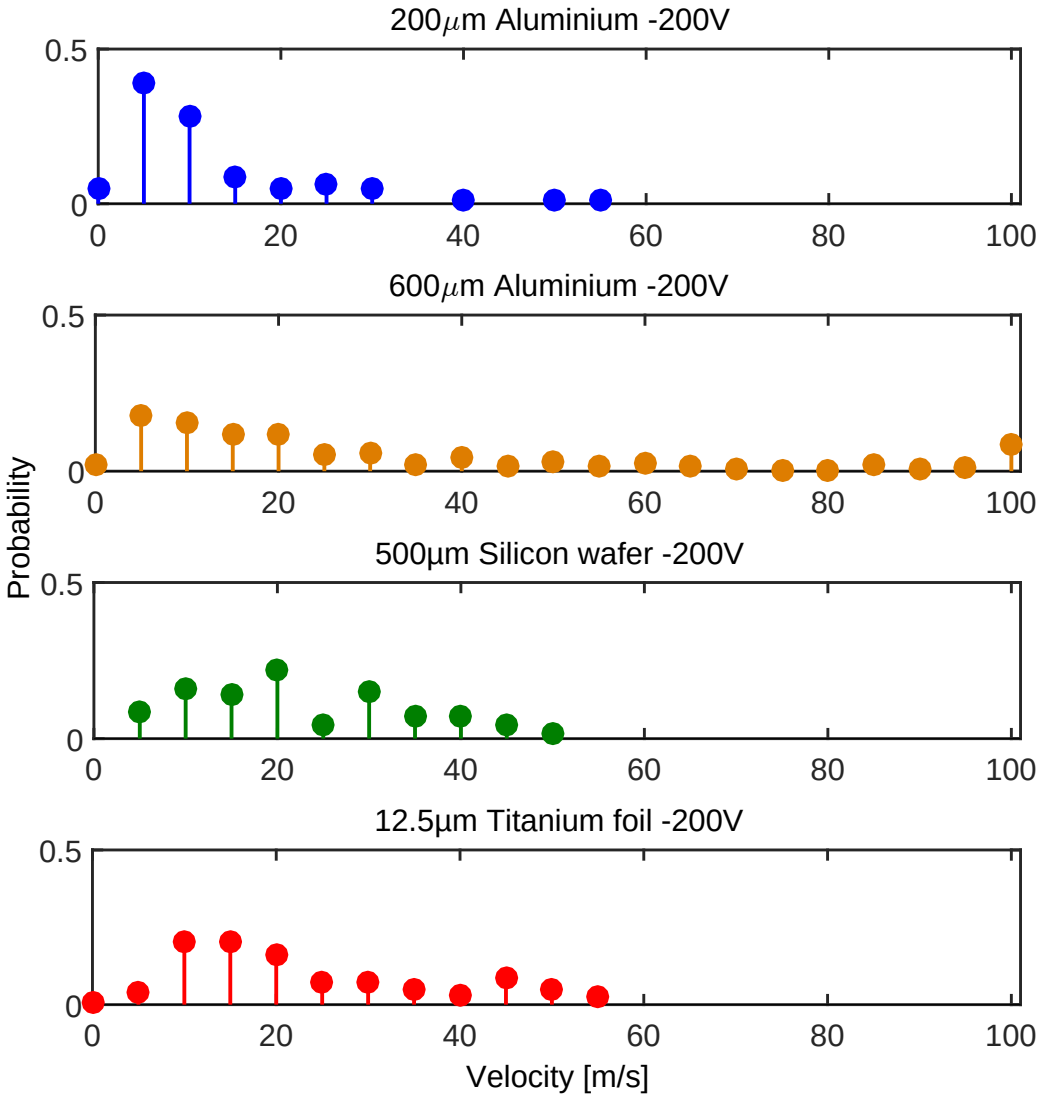

Figure B.3: Velocity distribution of silica nanoparticles launched via LIAD from 200 μm aluminium (blue), 600 μm aluminium (orange), 500 μm silicon wafer (green) and 12.5 μm titanium foil (red). All measurements were carried out with a potential difference of -200 V between cavity block and source. The slowest particle velocities are achieved with 200 μm aluminium.

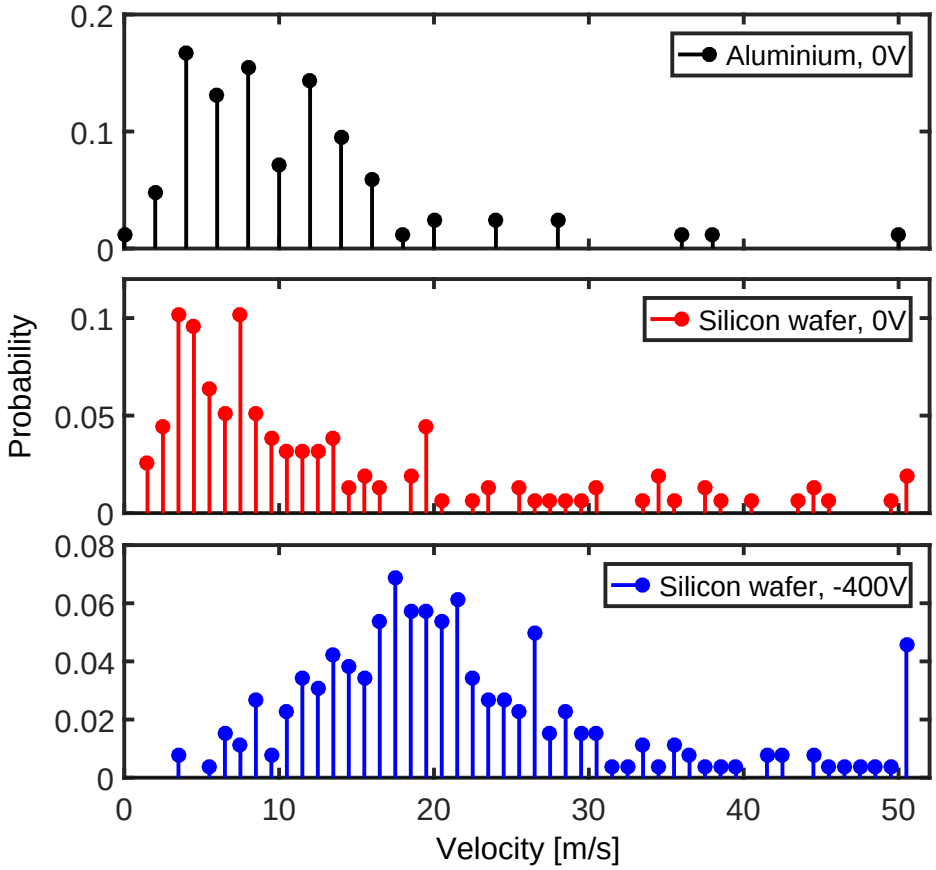

Figure B.4: Velocity distribution for nanodiced silicon particles. Launching from a 200 μm aluminium substrate (black, top) and a 360 μm silicon wafer (red, middle) at 0 V potential difference give similar results. A clear shift of the velocity distribution at a potential difference of -400 V between the cavity block and the source (blue, bottom) indicates that a large fraction of the silicon particles is charged.

C Nanorod parameters

Table C.1 lists the dimensions, mass and moment of inertia for all nanorod samples that have been used.

Properties \ Sample	S1	S2	S3	S4	S5
Rod Length [nm]	961 ± 37	1131 ± 35	686 ± 12	780 ± 14	795 ± 17
Rod Diameter [nm]	71 ± 20	101 ± 12	89 ± 12	135 ± 11	108 ± 16
Kerf Diameter [nm]	-	65 ± 9	40 ± 5	35 ± 8	41 ± 10
Mass [10^9 amu]	5.34 ± 3.02	12.7 ± 3.0	5.99 ± 1.62	15.7 ± 2.6	10.2 ± 3.0
Moment of Inertia [10^{-31} kg m^2]	6.82 ± 3.92	22.5 ± 5.7	3.90 ± 1.07	13.2 ± 2.3	8.94 ± 2.71

Table C.1: Properties of the nanorod samples.

Table C.2 lists the mean rotation rate, forward velocity and motional energies for the rod samples listed in Table C.1.

Properties \ Sample	S1	S2	S3	S4	S5
Number of Rods	112	63	121	61	85
$\langle f_{rot} \rangle$ [10^6 MHz]	18.7 ± 0.1	5.55 ± 0.1	5.77 ± 0.1	2.38 ± 0.1	4.20 ± 0.1
$\langle v_x \rangle$ [m/s]	98.6 ± 3.5	92.6 ± 5.6	54.0 ± 0.2	32.8 ± 0.1	36.5 ± 0.2
$\langle E_{rot} \rangle$ [10^3 eV]	41.8 ± 24.0	11.8 ± 3.0	2.47 ± 0.68	1.41 ± 0.25	3.04 ± 0.92
$\langle E_x \rangle$ [10^4 eV]	32.7 ± 18.5	71.0 ± 16.8	10.9 ± 2.9	11.7 ± 1.9	8.37 ± 2.46

Table C.2: Mean forward velocities, rotation rates and motional energies for all nanorod samples listed in Table C.1. We determine the kinetic and rotational energy $E_{\mathrm{kin}} = mv_x^2/2$ and $E_{\mathrm{rot}} = I(2\pi f_{\mathrm{rot}})^2/2$ from the measured forward velocity v_{x} and rotational frequency f_{rot}. All values represent an average over all rods observed for the individual samples.

D Polarisation calibration

In order to trap silicon nanorods under controllable conditions, it is crucial to carefully align the polarisation within the trap. As described in Publications 4.1 and 4.2, our standing light wave optical trap is formed by two counter-propagating beams. Except for the free-space region around the trap, most parts of the experiment are fiber-based. This includes an electro-optical lithium niobate polarisation controller (EOSPACE), which is employed to set arbitrary polarisation states. To ensure that the polarisation in both beams is identical and a standing light wave is formed, the birefringence in the two arms of the fiber-setup needs to be compensated by polarisation control paddels. In addition, the polarisation controller must be calibrated to set arbitrary polarisation states within the trap. It is, in principle, capable of performing eight arbitrary wave-plate operations, which can be controlled individually by three voltages per stage. For our purposes, a single wave-plate operation is sufficient and we have hard-wired all eight stages together. This also reduces the range of voltages that need to be applied to cover the full Bloch sphere and leaves us with three control voltages V_A, V_B, and V_C, from which V_B is connected to common ground.

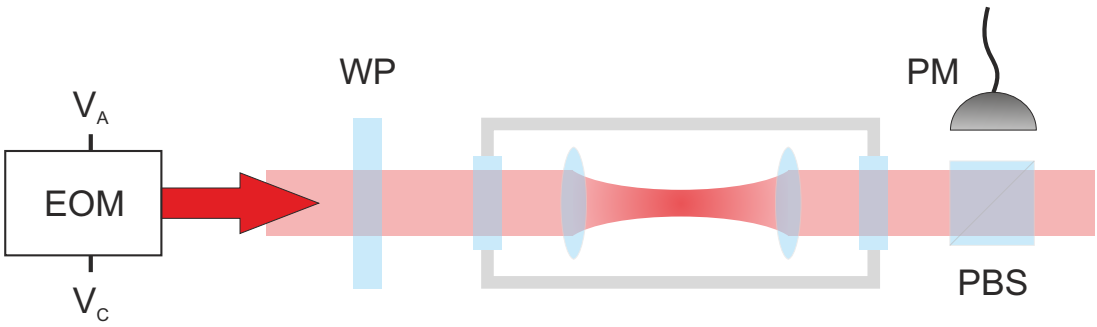

Figure D.1: Optical setup for calibrating the polarisation within the trap. A half-wave or quarter-wave-plate (HWP/QWP) is positioned within a motorized rotation stage before the trap while the counter-propagating beam is blocked. Behind the trap a polarising beam splitter (PBS) and a power meter (PM) are placed to measure the power of the beam reflected by the PBS. The lithium-niobate electro-optical polarisation modulator (EOSPACE) is controlled by the voltages V_A and V_C. The full optical setup can be found in Publication 4.1.

To set the polarisation control paddels and calibrate V_A & V_C, a setup as sketched in Figure D.1 is utilized. It consists of a motorized rotation stage (Thorlabs PRM1Z8)

in which we can controllably rotate a half-wave (HWP) or quarter-wave-plate (QWP). Behind the trap, a polarising beam splitter (PBS) is inserted and a power meter (Thorlabs S122C) measures the beam power in the up-reflected port. In the first step, we set V_A and V_C to zero and minimize the reflection from the PBS for the first beam B1 using the polarisation control paddels in B1 while the counter-propagating beam B2 is blocked and no wave-plate is inserted. In this way we ensure a vertical polarisation of B1 when no control voltages are applied. In the next step, we insert a half-wave-plate, such that initially the reflected intensity on the PBS remains minimal. By step-wise rotation of the HWP, the values for V_A and V_C can be determined at which the wave-plate operation can be counter-acted by the polarisation controller by keeping the reflected power on the PBS at a minimum. This process is automatized in a LabView routine (see Figure D.2). The same measurement is then carried out for a QWP.

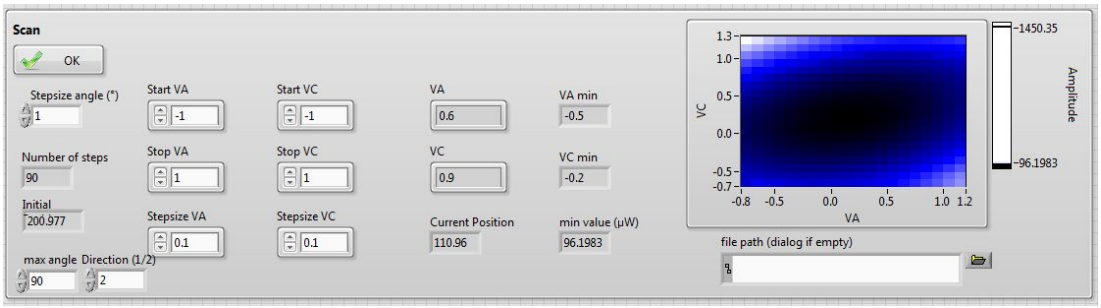

Figure D.2: LabView interface for calibrating the polarisation within the trap. The waveplate in Figure D.1 is rotated with a motorized rotation stage (Thorlabs PRM1Z8) and the control voltages of the polarisation controller V_A and V_C are scanned step-wise around the optimal setting for the previous angle of the waveplate while monitoring the power in the reflected port of the beamsplitter.

Once the polarisation controller is calibrated for B1, we have to make sure that the polarisation in B2 behaves in the same way. For this purpose, we flip around the calibration setup such that B2 first passes through the wave-plate, then the trap and the PBS while B1 is blocked. Before inserting a wave-plate, again we minimize the reflected power on the PBS via the paddels in B2 for $V_\mathrm{A} = V_\mathrm{C} = 0\,\mathrm{V}$ to obtain vertical polarisation in B2. Now we insert a QWP at an initial angle that keeps the reflection on the PBS at a minimum. Starting from this position, we rotate the QWP by 45 °, but instead of scanning the parameters V_A and V_C, we set them to the corresponding value, which has been obtained for B1. Now, we can set a subset of the polarisation paddels of B2 to minimize the reflected power on the PBS. The QWP is turned back to zero and the remaining paddels of B2 are used to minimize the reflected power again. This procedure is repeated until the reflected power for both QWP settings is at a minimum. The outcome converges quickest by optimising the two paddels which correspond to quarter-wave-plate operations (1 fiber loop) for linear polarisation (QWP at the initial

position) and the third paddel (2 loops) for circular polarisation (QWP at 45 °). Once the reflected power is minimized for both settings, the polarisation in both arms is equal and can be set by the polarisation modulator. The quality of the polarisation calibration can be tested by performing a parameter scan for the second arm as well, and a small miss-match can be compensated by averaging over the optimal settings for B1 and B2. It typically depends on the input polarisation into the polarisation controller. Figure D.3 shows typical values for V_A and V_C after calibration.

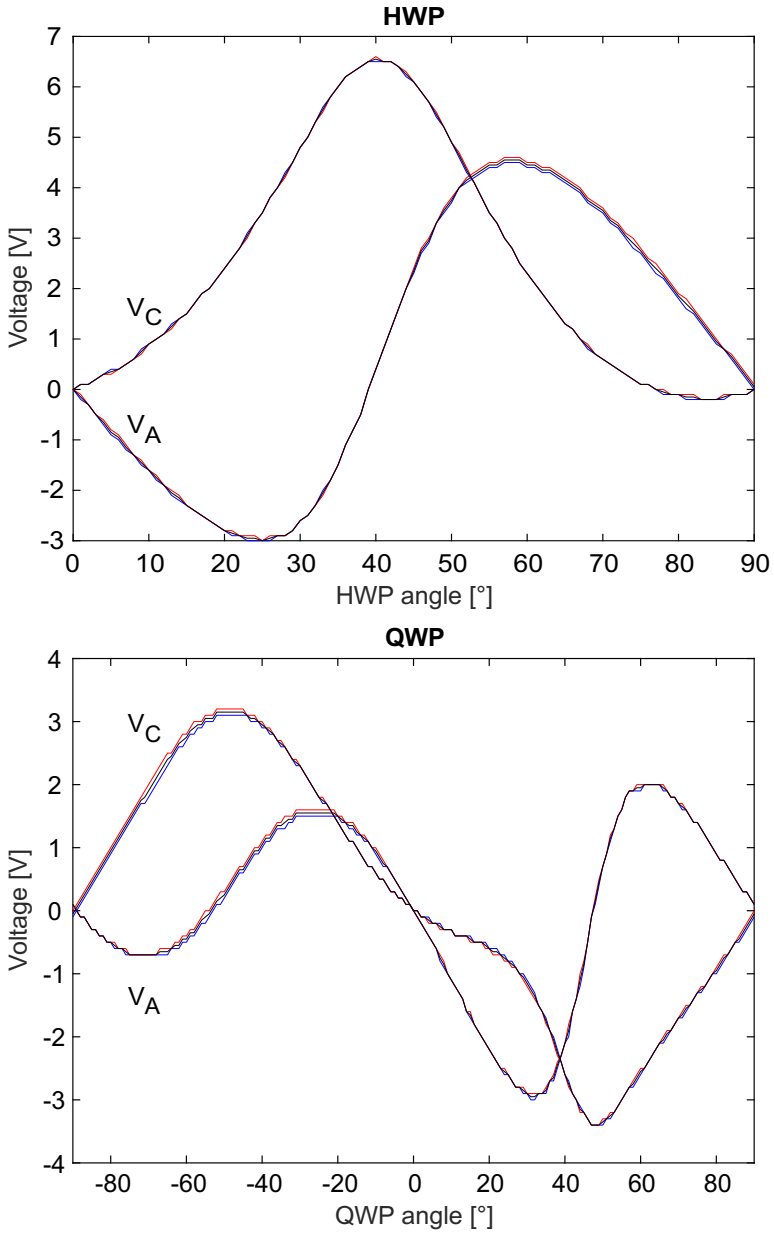

Figure D.3: Typical control voltages for HWP and QWP operations for B1 (blue) and B2 (red). The black curve shows an average value.

Bibliography

1. De Broglie, L. Ondes et Quanta. *Comptes Rendus Acad. Sci.* **117,** 507–510 (1923).
2. Tonomura, A. Applications of Electron Holography. *Rev. Mod. Phys.* **59,** 639–669 (1987).
3. Batelaan, H. Colloquium: Illuminating the Kapitza-Dirac effect with electron matter optics. *Rev. Mod. Phys.* **79,** 929–941 (2007).
4. Hasselbach, F. Progress in electron- and ion-interferometry. *Rep. Prog. Phys.* **73,** 016101 (2010).
5. Rauch, H. & Werner, A. *Neutron Interferometry: Lessons in Experimental Quantum Mechanics* (Oxford Univ. Press, 2000).
6. Berman, P. R. *Atom Interferometry* (Acad. Press, New York, 1997).
7. Cronin, A. D., Schmiedmayer, J. & Pritchard, D. E. Optics and interferometry with atoms and molecules. *Rev. Mod. Phys.* **81,** 1051–1129 (2009).
8. Tino, G. & Kasevich, M. Atom interferometry. *Proceedings of the International School of Physics" Enrico Fermi", Course CLXXXVIII, Varenna* (2013).
9. Schöllkopf, W. & Toennies, J. P. Nondestructive Mass Selection of Small Van der Waals Clusters. *Science* **266,** 1345–1348 (1994).
10. Brühl, R., Guardiola, R., Kalinin, A., Kornilov, O., Navarro, J., Savas, T. & Toennies, J. P. Diffraction of Neutral Helium Clusters: Evidence for 'Magic Numbers'. *Phys. Rev. Lett.* **92,** 185301 (2004).
11. Chapman, M. S., Ekstrom, C. R., Hammond, T. D., Rubenstein, R. A., Schmiedmayer, J., Wehinger, S. & Pritchard, D. E. Optics and Interferometry with Na2 Molecules. *Phys. Rev. Lett.* **74,** 4783–4786 (1995).
12. Bordé, C. J., Avrillier, S., Van Lerberghe, A., Salomon, C., Bassi, D. & Scoles, G. Observation of optical ramsey fringes in the 10 μm spectral region using a supersonic beam of SF6. *Le Journal de Physique Colloques* **42,** C8-15-C8-19 (1981).
13. Bordé, C., Courtier, N., Burck, F. D., Goncharov, A. & Gorlicki, M. Molecular Interferometry Experiments. *Phys. Lett. A* **188,** 187–197 (1994).

14. Lisdat, C., Frank, M., Knöckel, H., Almazor, M.-L. & Tiemann, E. Realization of a Ramsey-Borde Matter Wave Interferometer on the K2 Molecule. *Eur. Phys. J. D* **12,** 235–240 (2000).

15. Reisinger, T., Patel, A., Reingruber, H., Fladischer, K., Ernst, W., Bracco, G., Smith, H. & Holst, B. Poisson's spot with molecules. *Phys. Rev. A* **79,** 53823 (2009).

16. Zhao, B. S., Meijer, G. & Schoellkopf, W. Quantum Reflection of He(2) Several Nanometers Above a Grating Surface. *Science* **331,** 892–894 (2011).

17. Kovachy, T., Asenbaum, P., Overstreet, C., Donnelly, C. A., Dickerson, S. M., Sugarbaker, A., Hogan, J. M. & Kasevich, M. A. Quantum superposition at the half-metre scale. *Nature* **528,** 530–533 (2015).

18. Dimopoulos, S., Graham, P., Hogan, J. & Kasevich, M. Testing General Relativity with Atom Interferometry. *Phys. Rev. Lett.* **98,** 1–4 (2007).

19. Asenbaum, P., Overstreet, C., Kovachy, T., Brown, D. D., Hogan, J. M. & Kasevich, M. A. Phase Shift in an Atom Interferometer due to Spacetime Curvature across its Wave Function. *Phys. Rev. Lett.* **118,** 183602 (2017).

20. Hornberger, K., Gerlich, S., Haslinger, P., Nimmrichter, S. & Arndt, M. Colloquium: Quantum interference of clusters and molecules. *Rev. Mod. Phys.* **84,** 157–173 (2012).

21. Juffmann, T., Ulbricht, H. & Arndt, M. Experimental methods of molecular matter-wave optics. *Reports on progress in physics* **76,** 086402 (2013).

22. Arndt, M., Nairz, O., Vos-Andreae, J., Keller, C., van der Zouw, G. & Zeilinger, A. Wave-particle duality of C60 molecules. *Nature* **401,** 680–682 (1999).

23. Brezger, B., Hackermüller, L., Uttenthaler, S., Petschinka, J., Arndt, M. & Zeilinger, A. Matter-Wave Interferometer for Large Molecules. *Phys. Rev. Lett.* **88,** 100404 (2002).

24. Hackermüller, L., Uttenthaler, S., Hornberger, K., Reiger, E., Brezger, B., Zeilinger, A. & Arndt, M. Wave nature of biomolecules and fluorofullerenes. *Phys. Rev. Lett.* **91,** 90408 (2003).

25. Haslinger, P., Dörre, N., Geyer, P., Rodewald, J., Nimmrichter, S. & Arndt, M. A universal matter-wave interferometer with optical ionization gratings in the time domain. *Nature Phys.* **9,** 144–148 (2013).

26. Dörre, N., Rodewald, J., Geyer, P., von Issendorff, B., Haslinger, P. & Arndt, M. Photofragmentation Beam Splitters for Matter-Wave Interferometry. *Phys. Rev. Lett.* **113,** 233001 (2014).

27. Gerlich, S., Eibenberger, S., Tomandl, M., Nimmrichter, S., Hornberger, K., Fagan, P., Tüxen, J., Mayor, M. & Arndt, M. Quantum interference of large organic molecules. *Nat. Commun.* **2,** 263 (2011).

28. Eibenberger, S., Gerlich, S., Arndt, M., Mayor, M. & Tüxen, J. Matter-wave interference with particles selected from a molecular library with masses exceeding 10 000 amu. *Phys. Chem. Chem. Phys.* (2013).

29. Juffmann, T., Nimmrichter, S., Arndt, M., Gleiter, H. & Hornberger, K. New Prospects for de Broglie Interferometry. *Foundations of Physics* **42,** 98–110 (2012).

30. Juffmann, T. *Surface based detection schemes for molecular matter-wave interferometry* Dissertation (2012).

31. Sclafani, M., Juffmann, T., Knobloch, C. & Arndt, M. Quantum coherent propagation of complex molecules through the frustule of the alga Amphipleura Pellucida. *New J. Phys.* (2013).

32. Brand, C., Sclafani, M., Knobloch, C., Lilach, Y., Juffmann, T., Kotakoski, J., Mangler, C., Winter, A., Turchanin, A., Meyer, J., Cheshnovsky, O. & Arndt, M. An atomically thin matter-wave beamsplitter. *Nature Nanotechnology* **10,** 845–848 (2015).

33. Brezger, B., Arndt, M. & Zeilinger, A. Concepts for near-field interferometers with large molecules. *Journal of Optics B-Quantum and Semiclassical Optics* **5,** S82–S89 (2003).

34. Gerlich, S., Hackermüller, L., Hornberger, K., Stibor, A., Ulbricht, H., Gring, M., Goldfarb, F., Savas, T., Müri, M., Mayor, M. & Arndt, M. A Kapitza-Dirac-Talbot-Lau interferometer for highly polarizable molecules. *Nature Physics* **3,** 711–715 (2007).

35. Gerlich, S. *Interferometry and Metrology with Macromolecules* Thesis (2011).

36. Eibenberger, S. *Quantum interference experiments with complex organic molecules* Thesis (2015).

37. Nimmrichter, S., Hornberger, K., Haslinger, P. & Arndt, M. Testing spontaneous localization theories with matter-wave interferometry. *Phys. Rev. A* **83,** 043621 (2011).

38. Haslinger, P. *A universal matter-wave interferometer with optical gratings* Thesis (2013).

39. Dörre, N. *Time-domain matter-wave interferometry with clusters and large molecules* Dissertation (2015).

40. Rodewald, J. *Experiments with a pulsed Talbot Lau matter-wave interferometer* Dissertation (2017).

41. Geyer, P., Sezer, U., Rodewald, J., Mairhofer, L., Dörre, N., Haslinger, P., Eibenberger, S., Brand, C. & Arndt, M. Perspectives for quantum interference with biomolecules and biomolecular clusters. *Physica Scripta* **91,** 063007 (2016).

42. Brand, C., Eibenberger, S., Sezer, U. & Arndt, M. Matter-wave physics with nanoparticles and biomolecules. arXiv: 1703.02129 (2017).

43. Mairhofer, L., Eibenberger, S., Cotter, J. P., Romirer, M., Shayeghi, A. & Arndt, M. Quantum-Assisted Metrology of Neutral Vitamins in the Gas Phase. *Angewandte Chemie International Edition* **56,** 10947–10951 (2017).

44. Nimmrichter, S. & Hornberger, K. Macroscopicity of Mechanical Quantum Superposition States. *Phys. Rev. Lett.* **110,** 160403 (2013).

45. Arndt, M. & Hornberger, K. Insight review: Testing the limits of quantum mechanical superpositions. *Nature Phys.* **10,** 271–277 (2014).

46. Dowling, J. P. & Milburn, G. J. Quantum technology: the second quantum revolution. *Philos Transact A Math Phys Eng Sci* **361,** 1655–74 (2003).

47. Zeilinger, A. Experiment and the foundations of quantum physics. *Rev. Mod. Phys.* **71,** S288–S297 (1999).

48. Will, C. M. The Confrontation between General Relativity and Experiment. *Living Reviews in Relativity* **17,** 4 (June 2014).

49. Whitaker, A. & Einstein, B. *the Quantum Dilemma: From Quantum Theory to Quantum Information* 2006.

50. Joos, E., Zeh, H. D., Kiefer, C., Giulini, D., Kupsch, J. & Stamatescu, I.-O. *Decoherence and the appearance of a classical world in quantum theory* 2nd (Springer, Berlin, 2003).

51. Zurek, W. H. Decoherence, Einselection, and the Quantum Origins of the Classical. *Rev. Mod. Phys.* **75,** 715–775 (2003).

52. Schlosshauer, M. Decoherence, the measurement problem, and interpretations of quantum mechanics. *Rev. Mod. Phys.* **76,** 1267–1305 (2004).

53. Schrödinger, E. Die gegenwärtige Situation in der Quantenmechanik. *Naturwissenschaften* **23,** 844–849 (1935).

54. Everett Hugh, I. "Relative State" Formulation of Quantum Mechanics. *Rev. Mod. Phys.* **29,** 454–462 (1957).

55. Bohr, N. The Quantum Postulate and the Recent Development of Atomic Theory1. *Nature* **121,** 580–590 (1928).

56. Wheeler, J. A. & Zurek, W. H. *Quantum theory and measurement* (Princeton University Press, 2014).

57. Bassi, A., Lochan, K., Satin, S., Singh, T. P. & Ulbricht, H. Models of wave-function collapse, underlying theories, and experimental tests. *Rev. Mod. Phys.* **85,** 471–527 (2013).

58. Leggett, A. J. Probing Quantum Mechanics Towards the Everyday World: Where do we Stand? *Physica Scripta* **2002,** 69 (2002).

59. Carlesso, M., Bassi, A., Falferi, P. & Vinante, A. Experimental bounds on collapse models from gravitational wave detectors. *Phys. Rev. D* **94,** 124036 (2016).

60. Ghirardi, G. C., Rimini, A. & Weber, T. Unified dynamics for microscopic and macroscopic systems. *Phys. Rev. D* **34,** 470–491 (1986).

61. Pearle, P. Combining Stochastic Dynamical State-Vector Reduction with Spontaneous Localization. *Phys. Rev. A* **39,** 2277–2289 (1989).

62. Ghirardi, G. C., Pearle, P. & Rimini, A. Markov Processes in Hilbert Space and Continuous Spontaneous Localization of Systems of Identical Particles. *Phys. Rev. A* **42,** 78–89 (1990).

63. Adler, S. L. & Bassi, A. Collapse models with non-white noises. *Journal of Physics A: Mathematical and Theoretical* **40,** 15083 (2007).

64. Adler, S. & Bassi, A. Collapse models with non-white noises: II. Particle-density coupled noises. *J. Phys. A.* **41,** 395308 (2008).

65. Bassi, A., Ippoliti, E. & Vacchini, B. On the energy increase in space-collapse models. *J. Phys. A.* **38,** 8017 (2005).

66. Vinante, A., Bahrami, M., Bassi, A., Usenko, O., Wijts, G. & Oosterkamp, T. H. Upper Bounds on Spontaneous Wave-Function Collapse Models Using Millikelvin-Cooled Nanocantilevers. *Phys. Rev. Lett.* **116,** 090402 (2016).

67. Curceanu, C., Bartalucci, S., Bassi, A., Bertolucci, S., Berucci, C., Bragadireanu, A. M., Cargnelli, M., Clozza, A., Paolis, L. D., Matteo, S. D., Donadi, S., d'Uffizi, A., Egger, J.-P., Guaraldo, C., Iliescu, M., Laubenstein, M., Marton, J., Milotti, E., Pichler, A., Pietreanu, D., Piscicchia, K., Ponta, T., Sbardella, E., Scordo, A., Shi, H., Sirghi, D. L., Sirghi, F., Sperandio, L., Doce, O. V. & Zmeskal, J. X rays on quantum mechanics: Pauli Exclusion Principle and collapse models at test. *Journal of Physics: Conference Series* **631,** 012068 (2015).

68. Nimmrichter, S. *Macroscopic Matter-wave Interferometry* Thesis (2013).

69. Toroš, M., Gasbarri, G. & Bassi, A. Colored and dissipative continuous spontaneous localization model and bounds from matter-wave interferometry. *Physics Letters A* **381,** 3921–3927 (2017).

70. Karolyhazy, F. Gravitation and quantum mechanics of macroscopic objects. *Il Nuovo Cimento A* **42,** 390–402 (1966).

71. Diósi, L. A universal master equation for the gravitational violation of quantum mechanics. *Phys. Lett. A* **120,** 377–381 (1987).

72. Penrose, R. On gravity's role in quantum state reduction. *Gen. Rel. Grav.* **28,** 581–600 (1996).

73. Bateman, J., Nimmrichter, S., Hornberger, K. & Ulbricht, H. Near-field interferometry of a free-falling nanoparticle from a point-like source. *Nat. Commun.* **5,** 4788 (2014).

74. Kaltenbaek, R., Aspelmeyer, M., Barker, P. F., Bassi, A., Bateman, J., Bongs, K., Bose, S., Braxmaier, C., Brukner, Č., Christophe, B., Chwalla, M., Cohadon, P.-F., Cruise, A. M., Curceanu, C., Dholakia, K., Diósi, L., Döringshoff, K., Ertmer, W., Gieseler, J., Gürlebeck, N., Hechenblaikner, G., Heidmann, A., Hermann, S., Hossenfelder, S., Johann, U., Kiesel, N., Kim, M., Lämmerzahl, C., Lambrecht, A., Mazilu, M., Milburn, G. J., Müller, H., Novotny, L., Paternostro, M., Peters, A., Pikovski, I., Pilan Zanoni, A., Rasel, E. M., Reynaud, S., Riedel, C. J., Rodrigues, M., Rondin, L., Roura, A., Schleich, W. P., Schmiedmayer, J., Schuldt, T., Schwab, K. C., Tajmar, M., Tino, G. M., Ulbricht, H., Ursin, R. & Vedral, V. Macroscopic Quantum Resonators (MAQRO): 2015 update. *EPJ Quantum Technology* **3,** 5 (Dec. 2016).

75. Romero-Isart, O., Pflanzer, A. C., Juan, M. L., Quidant, R., Kiesel, N., Aspelmeyer, M. & Cirac, J. I. Optically levitating dielectrics in the quantum regime: Theory and protocols. *Phys. Rev. A* **83** (2011).

76. Romero-Isart, O. Quantum superposition of massive objects and collapse models. *Phys. Rev. A* **84,** 052121 (2011).

77. Romero-Isart, O., Pflanzer, A. C., Blaser, F., Kaltenbaek, R., Kiesel, N., Aspelmeyer, M. & Cirac, J. I. Large Quantum Superpositions and Interference of Massive Nanometer-Sized Objects. *Phys. Rev. Lett.* **107,** 020405 (2011).

78. Romero-Isart, O. Coherent inflation for large quantum superpositions of levitated microspheres. *New J. Phys.* (2017).

79. Pino, H., Prat-Camps, J., Sinha, K., Venkatesh, B. P. & Romero-Isart, O. On-Chip Quantum Interference of a Superconducting Microsphere. *Quantum Science and Technology* (2017).

80. Nimmrichter, S., Haslinger, P., Hornberger, K. & Arndt, M. Concept of an ionizing time-domain matter-wave interferometer. *New. J. Phys.* **13,** 075002 (2011).

81. Talbot, H. F. Facts Relating to Optical Science. *Philos. Mag.* **9,** 401–407 (1836).

82. Hsieh, C.-L., Spindler, S., Ehrig, J. & Sandoghdar, V. Tracking Single Particles on Supported Lipid Membranes: Multimobility Diffusion and Nanoscopic Confinement. *The Journal of Physical Chemistry B* **118,** 1545–1554 (2014).

83. Lin, Y.-H., Chang, W.-L. & Hsieh, C.-L. Shot-noise limited localization of single 20 nm gold particles with nanometer spatial precision within microseconds. *Optics Express* **22,** 9159 (2014).

84. Lide, D. R. *CRC Handbook of Chemistry and Physics, 88th edition* (CRC Press, New York, 2008).

85. Wendt, S., Ozensoy, E., Wei, T., Frerichs, M., Cai, Y., Chen, M. S. & Goodman, D. W. Electronic and vibrational properties of ultrathin SiO_2 films grown on Mo(112). *Phys. Rev. B* **72,** 115409 (2005).

86. Giordano, L., Cinquini, F. & Pacchioni, G. Tuning the surface metal work function by deposition of ultrathin oxide films: Density functional calculations. *Phys. Rev. B* **73,** 045414 (2006).

87. Mestres, P., Berthelot, J., Spasenović, M., Gieseler, J., Novotny, L. & Quidant, R. Cooling and manipulation of a levitated nanoparticle with an optical fiber trap. *Appl. Phys. Lett.* **107,** 151102 (2015).

88. Habraken, S. J. M., Lechner, W. & Zoller, P. Resonances in dissipative optomechanics with nanoparticles: Sorting, speed rectification, and transverse cooling. *Phys. Rev. A* **87** (2013).

89. Asenbaum, P. *Cavity cooling of silicon nanoparticles in high-vacuum* Dissertation (2014).

90. Hornberger, K., Uttenthaler, S., Brezger, B., Hackermüller, L., Arndt, M. & Zeilinger, A. Collisional decoherence observed in matter wave Interferometry. *Phys. Rev. Lett.* **90,** 160401 (2003).

91. Hackermüller, L., Hornberger, K., Brezger, B., Zeilinger, A. & Arndt, M. Decoherence of matter waves by thermal emission of radiation. *Nature* **427,** 711–714 (2004).

92. Hornberger, K., Sipe, J. E. & Arndt, M. Theory of Decoherence in a Matter Mave Talbot-Lau Interferometer. *Phys. Rev. A* **70,** 53608 (2004).

93. Gabrielse, G., Fei, X., Orozco, L. A., Tjoelker, R. L., Haas, J., Kalinowsky, H., Trainor, T. A. & Kells, W. Thousandfold Improvement in the Measured Antiproton Mass. *Phys. Rev. Lett.* **65,** 1317 (1990).

94. Gabrielse, G. in (eds Bederson, B. & Walther, H.) *Advances In Atomic, Molecular, and Optical Physics* Supplement C, 1–39 (Academic Press, 2001).

95. Benvenuti, C. & Chiggiato, P. Pumping characteristics of the St707 nonevaporable getter (Zr 70 V 24.6-Fe 5.4). *Journal of Vacuum Science & Technology A: Vacuum, Surfaces, and Films* **14,** 3278–3282 (1996).

96. Vacchini, B. On the precise connection between the GRW master equation and master equations for the description of decoherence. *Journal of Physics A: Mathematical and Theoretical* **40,** 2463 (2007).

97. Marshall, W., Simon, C., Penrose, R. & Bouwmeester, D. Towards Quantum Superpositions of a Mirror. *Phys. Rev. Lett.* **91,** 130401 (2003).

98. Riedel, C. J. & Yavin, I. Decoherence as a way to measure extremely soft collisions with dark matter. *Phys. Rev. D* **96,** 023007 (2017).

99. Knobloch, C., Stickler, B. A., Brand, C., Sclafani, M., Lilach, Y., Juffmann, T., Cheshnovsky, O., Hornberger, K. & Arndt, M. On the role of the electric dipole moment in the diffraction of biomolecules at nanomechanical gratings. *Fortschritte der Physik* **65,** 1600025–n/a (2017).

100. Lan, S.-Y., Kuan, P.-C., Estey, B., Haslinger, P. & Müller, H. Influence of the Coriolis Force in Atom Interferometry. *Phys. Rev. Lett.* **108,** 090402 (2012).

101. Cotter, J. P., Eibenberger, S., Mairhofer, L., Cheng, X., Asenbaum, P., Arndt, M., Walter, K., Nimmrichter, S. & Hornberger, K. Coherence in the presence of absorption and heating in a molecule interferometer. *Nature Communications* **6,** 7336 (2015).

102. Grass, D., Fesel, J., Hofer, S. G., Kiesel, N. & Aspelmeyer, M. Optical trapping and control of nanoparticles inside evacuated hollow core photonic crystal fibers. *Appl. Phys. Lett.* **108** (2016).

103. Kosloff, A., Heifler, O., Granot, E. & Patolsky, F. Nanodicing Single Crystalline Silicon Nanowire Arrays. *Nano Letters* **16,** 6960–6966 (2016).

104. Kuhn, S., Asenbaum, P., Kosloff, A., Sclafani, M., Stickler, B. A., Nimmrichter, S., Hornberger, K., Cheshnovsky, O., Patolsky, F. & Arndt, M. Cavity-Assisted Manipulation of Freely Rotating Silicon Nanorods in High Vacuum. *Nano Lett.* **15,** 5604–5608 (2015).

105. Zinovev, A., Veryovkin, I. & Pellin, M. in *Acoustic Waves - From Microdevices to Helioseismology,* (ed Beghi, M. G.) (InTech China, 2011).

106. Posthumus, M. A., Kistemaker, P. G., Meuzelaar, H. L. C. & de Brauw, M. C. T. N. Laser desorption-mass spectrometry of polar nonvolatile bio-organic molecules. *Anal. Chem.* **50,** 985–991 (1978).

107. Lindner, B. & Seydel, U. Laser Desorption Mass Spectrometry of Nonvolatlles under Shock Wave Conditions. *Society,* 895–899 (1985).

108. Golovlev, V. V., Allman, S. L., Garrett, W. R., Taranenko, N. I. & Chen, C. H. Laser-induced acoustic desorption. *Int. J. Mass Spectr. Ion Proc.* **169-170,** 69–78 (1997).

109. Pérez, J., Ramírez-Arizmendi, L. E., Petzold, C. J., Guler, L. P., Nelson, E. D. & Kenttämaa, H. I. Laser-induced acoustic desorption/chemical ionization in Fourier-transform ion cyclotron resonance mass spectrometry. *International Journal of Mass Spectrometry* **198,** 173–188 (2000).

110. Peng, W.-P., Yang, Y.-C., Kang, M.-W., Tzeng, Y.-K., Nie, Z., Chang, H.-C., Chang, W. & Chen, C.-H. Laser-Induced Acoustic Desorption Mass Spectrometry of Single Bioparticles. *Angewandte Chemie* **118,** 1451–1454 (2006).

111. Asenbaum, P., Kuhn, S., Nimmrichter, S., Sezer, U. & Arndt, M. Cavity cooling of free silicon nanoparticles in high-vacuum. *Nat. Commun.* **4,** 2743 (2013).

112. Stickler, B. A., Nimmrichter, S., Martinetz, L., Kuhn, S., Arndt, M. & Hornberger, K. Rotranslational cavity cooling of dielectric rods and disks. *Physical Review A* **94,** 033818 (2016).

113. Kuhn, S., Kosloff, A., Stickler, B. A., Patolsky, F., Hornberger, K., Arndt, M. & Millen, J. Full rotational control of levitated silicon nanorods. *Optica* **4,** 356 (2017).

114. Kuhn, S., Stickler, B. A., Kosloff, A., Patolsky, F., Hornberger, K., Arndt, M. & Millen, J. Optically driven ultra-stable nanomechanical rotor. *Nat. Commun.* **8,** 1670 (2017).

115. Pflanzer, A. C., Romero-Isart, O. & Cirac, J. I. Master-equation approach to optomechanics with arbitrary dielectrics. *Phys. Rev. A* **86** (2012).

116. Kuhn, S. *Molecular Droplets Coupled to Intense Cavity Fields* Masterarbeit (2013).

117. Bhushan, B. *Springer Handbook of Nanotechnology* (ed Bhushan, B.) (Springer Berlin Heidelberg, Berlin, Heidelberg, 2010).

118. Schiffer, R. & Thielheim, K. Light scattering by dielectric needles and disks. *Journal of Applied Physics* **50,** 2476–2483 (1979).

119. Monteiro, T. S., Millen, J., Pender, G. A. T., Marquardt, F., Chang, D. & Barker, P. F. Dynamics of levitated nanospheres: Towards the strong coupling regime. *New Journal of Physics* **15** (2013).

120. Mossotti, O. F. *Mem. di mathem. e fisica in Modena* 24 11 (1850).

121. Clausius, R. *Die mechanische wärmetheorie* (Vieweg, 1887).

122. Hulst, H. & Van De Hulst, H. *Light scattering by small particles* (Dover, 1957).

123. Stickler, B. A. Private Communication.

124. Li, T., Kheifets, S. & Raizen, M. G. Millikelvin cooling of an optically trapped microsphere in vacuum. *Nature Phys.* **7,** 527–530 (2011).

125. Gieseler, J., Deutsch, B., Quidant, R. & Novotny, L. Subkelvin Parametric Feedback Cooling of a Laser-Trapped Nanoparticle. *Phys. Rev. Lett.* **109,** 103603 (2012).

126. Kiesel, N., Blaser, F., Delic, U., Grass, D., Kaltenbaek, R. & Aspelmeyer, M. Cavity cooling of an optically levitated nanoparticle. *Proc. Natl. Acad. Sci. USA* **110,** 14180–14185 (2013).

127. Millen, J., Fonseca, P. Z. G., Mavrogordatos, T., Monteiro, T. S. & Barker, P. F. Cavity cooling a single charged levitated nanosphere. *Phys. Rev. Lett.* **114,** 1–5 (2015).

128. Fonseca, P. Z. G., Aranas, E. B., Millen, J., Monteiro, T. S. & Barker, P. F. Nonlinear Dynamics and Strong Cavity Cooling of Levitated Nanoparticles. *Phys. Rev. Lett.* **117,** 173602 (2016).

129. Vovrosh, J., Rashid, M., Hempston, D., Bateman, J., Paternostro, M. & Ulbricht, H. Parametric feedback cooling of levitated optomechanics in a parabolic mirror trap. *J. Opt. Soc. Am. B* **34,** 1421–1428 (2017).

130. Frimmer, M., Gieseler, J. & Novotny, L. Cooling Mechanical Oscillators by Coherent Control. *Phys. Rev. Lett.* **117,** 163601 (2016).

131. Jain, V., Gieseler, J., Moritz, C., Dellago, C., Quidant, R. & Novotny, L. Direct Measurement of Photon Recoil from a Levitated Nanoparticle. *Phys. Rev. Lett.* **116,** 243601 (2016).

132. Barker, P. F. Doppler Cooling a Microsphere. *Phys. Rev. Lett.* **105** (2010).

133. Romero-Isart, O., Juan, M., Quidant, R. & Cirac, J. Toward quantum superposition of living organisms. *New J. Phys.* **12,** 033015 (2010).

134. Chang, D. E., Regal, C. A., Papp, S. B., Wilson, D. J., Ye, J., Painter, O., Kimble, H. J. & Zoller, P. Cavity opto-mechanics using an optically levitated nanosphere. *Proc. Nat. Acad. Sc.* **107,** 1005–1010 (2010).

135. Moore, D. C., Rider, A. D. & Gratta, G. Search for Millicharged Particles Using Optically Levitated Microspheres. *Phys. Rev. Lett.* **113,** 251801 (2014).

136. Ranjit, G., Montoya, C. & Geraci, A. A. Cold atoms as a coolant for levitated optomechanical systems. *Phys. Rev. A* **91** (2015).

137. Ranjit, G., Cunningham, M., Casey, K. & Geraci, A. A. Zeptonewton force sensing with nanospheres in an optical lattice. *Phys. Rev. A* **93,** 053801 (2016).

138. Hempston, D., Vovrosh, J., Toroš, M., Winstone, G., Rashid, M. & Ulbricht, H. Force sensing with an optically levitated charged nanoparticle. *Appl. Phys. Lett.* **111,** 133111 (2017).

139. Li, T., Kheifets, S., Medellin, D. & Raizen, M. G. Measurement of the instantaneous velocity of a Brownian particle. *Science* **328,** 1673–5 (2010).

140. Gieseler, J., Novotny, L. & Quidant, R. Thermal nonlinearities in a nanomechanical oscillator. *Nature Physics* **9,** 806–810 (2013).

141. Gieseler, J., Quidant, R., Dellago, C. & Novotny, L. Dynamic relaxation of a levitated nanoparticle from a non-equilibrium steady state. *Nature Nanotech.* **9,** 358–64 (Mar. 2014).

142. Gieseler, J., Novotny, L., Moritz, C. & Dellago, C. Non-equilibrium steady state of a driven levitated particle with feedback cooling. *New J. Phys.* **17,** 045011 (2015).

143. Ricci, F., Rica, R. A., Spasenović, M., Gieseler, J., Rondin, L., Novotny, L. & Quidant, R. Optically levitated nanoparticle as a model system for stochastic bistable dynamics. *Nat. Commun.* **8,** 15141 (2017).

144. Neukirch, L. P., Gieseler, J., Quidant, R., Novotny, L. & Vamivakas, A. N. Observation of nitrogen vacancy photoluminescence from an optically levitated nanodiamond. *Opt. Lett.* **38,** 2976–2979 (2013).

145. Hoang, T. M., Ma, Y., Ahn, J., Bang, J., Robicheaux, F., Yin, Z.-Q. & Li, T. Torsional Optomechanics of a Levitated Nonspherical Nanoparticle. *Phys. Rev. Lett.* **117,** 123604 (2016).

146. Arvanitaki, A. & Geraci, A. A. Detecting High-Frequency Gravitational Waves with Optically Levitated Sensors. *Phys. Rev. Lett.* **110,** 071105 (2013).

147. Arita, Y., Mazilu, M. & Dholakia, K. Laser-induced rotation and cooling of a trapped microgyroscope in vacuum. *Nat. Commun.* **4** (2013).

148. Ashkin, A. & Dziedzic, J. M. Feedback stabilization of optically levitated particles. *Appl. Phys. Lett.* **30,** 202–204 (1977).

149. Gieseler, J. *Dynamics of optically levitated nanoparticles in high vacuum* Thesis (2014).

150. Villanueva, L. G., Karabalin, R. B., Matheny, M. H., Kenig, E., Cross, M. C. & Roukes, M. L. A Nanoscale Parametric Feedback Oscillator. *Nano Letters* **11,** 5054–5059 (2011).

151. Jain, V., Tebbenjohanns, F. & Novotny, L. *Microkelvin Control of an Optically Levitated Nanoparticle* in *Frontiers in Optics 2016* (OSA, Washington, D.C., 2016), FF5B.2.

152. Jain, V. *Levitated optomechanics at the photon recoil limit* Thesis (2017).

153. Hänsch, T. W. & Schawlow, A. L. Cooling of Gases by Laser Radiation. *Opt. Commun.* **13,** 68 (1975).

154. Wineland, D. & Dehmelt, H. Proposed $10^1 4 <$ Laser Fluorescence Spectroscopy on Tl^+ Mono-Ion Oscillator III (Side Band Cooling). *Bull. Am. Phys. Soc.* **Ser. II, 20,** 637 (1975).

155. Dalibard, J. & Cohen-Tannoudji, C. Laser cooling below the Doppler limit by polarization gradients: simple theoretical-models. *J. Opt. Soc. Am. B* **6,** 2023 (1989).

156. Aspect, A., Arimondo, E., Kaiser, R., Vansteenkiste, N. & Cohen–Tannoudji, C. Laser Cooling Below the One-Photon Recoil Energy by Velocity-Selective Coherent Population Trapping. *Phys. Rev. Lett.* **61,** 826–829 (1988).

157. Kasevich, M. & Chu, S. Laser Cooling Below a Photon Recoil with Three-Level Atoms. *Phys. Rev. Lett.* **69,** 1741–1744 (1992).

158. Philips, W. D. Laser Cooling and Trapping of Neutral Atoms. *Rev. Mod. Phys.* **70,** 721–741 (1998).

159. Shuman, E. S., Barry, J. F. & DeMille, D. Laser cooling of a diatomic molecule. *Nature* **467,** 820–3 (2010).

160. Carr, L. D., DeMille, D., Krems, R. V. & Ye, J. *New J. Phys.* **11,** 055049 (2009).

161. Lemeshko, M., Krems, R. V., Doyle, J. M. & Kais, S. Manipulation of molecules with electromagnetic fields. *Molecular Physics* **111,** 1648–1682 (2013).

162. Kozyryev, I., Baum, L., Matsuda, K., Augenbraun, B. L., Anderegg, L., Sedlack, A. P. & Doyle, J. M. Sisyphus Laser Cooling of a Polyatomic Molecule. *Phys. Rev. Lett.* **118,** 173201 (2017).

163. Horak, P., Hechenblaikner, G., Gheri, K. M., Stecher, H. & Ritsch, H. Cavity-Induced Atom Cooling in the Strong Coupling Regime. *Phys. Rev. Lett.* **79,** 4974–4977 (1997).

164. Vuletic, V. & Chu, S. Laser Cooling of Atoms, Ions, or Molecules by Coherent Scattering. *Phys. Rev. Lett.* **84,** 3787–3790 (2000).

165. Nimmrichter, S., Hammerer, K., Asenbaum, P., Ritsch, H. & Arndt, M. Master equation for the motion of a polarizable particle in a multimode cavity. *New J Phys.* **12,** 083003 (2010).

166. Salzburger, T. & Ritsch, H. Collective transverse cavity cooling of a dense molecular beam. *New J. Phys.* **11,** 055025 (2009).

167. Asenbaum, P. *Towards Cavity Cooling of a Molecular Beam* Diplomarbeit (2009).

168. Chan, H. W., Black, A. T. & Vuletic, V. Observation of Collective-Emission-Induced Cooling of Atoms in an Optical Cavity. *Phys. Rev. Lett.* **90,** 063003–1 (2003).

169. Maunz, P., Puppe, T., Schuster, I., Syassen, N., Pinkse, P. W. H. & Rempe, G. Cavity Cooling of a Single Atom. *Nature* **428,** 50–52 (2004).

170. Leibrandt, D., Labaziewicz, J., Vuletic, V. & Chuang, I. Cavity sideband cooling of a single trapped ion. *Phys. Rev. Lett.* **103,** 103001 (2009).

171. Hosseini, M., Duan, Y., Beck, K. M., Chen, Y.-T. & Vuleti ć, V. Cavity Cooling of Many Atoms. *Phys. Rev. Lett.* **118,** 183601 (2017).

172. Schulze, R. J., Genes, C. & Ritsch, H. Optomechanical approach to cooling of small polarizable particles in a strongly pumped ring cavity. *Phys. Rev. A* **81,** 063820 (2010).

173. Pender, G. A. T., Barker, P. F., Marquardt, F., Millen, J. & Monteiro, T. S. Optomechanical cooling of levitated spheres with doubly resonant fields. *Phys. Rev. A* **85,** 021802 (2012).

174. Hunger, D., Deutsch, C., Barbour, R. J., Warburton, R. J. & Reichel, J. Laser micro-fabrication of concave, low-roughness features in silica. *AIP Advances* **2,** 012119 (2012).

175. Brandstätter, B., McClung, A., Schüppert, K., Casabone, B., Friebe, K., Stute, A., Schmidt, P. O., Deutsch, C., Reichel, J., Blatt, R. & Northup, T. E. Integrated fiber-mirror ion trap for strong ion-cavity coupling. *Review of Scientific Instruments* **84,** 123104 (2013).

176. Ott, K., Garcia, S., Kohlhaas, R., Schüppert, K., Rosenbusch, P., Long, R. & Reichel, J. Millimeter-long fiber Fabry-Perot cavities. *Opt. Express* **24,** 9839–9853 (2016).

177. Albrecht, R., Bommer, A., Deutsch, C., Reichel, J. & Becher, C. Coupling of a Single Nitrogen-Vacancy Center in Diamond to a Fiber-Based Microcavity. *Phys. Rev. Lett.* **110,** 243602 (2013).

178. Albrecht, R., Bommer, A., Pauly, C., Mücklich, F., Schell, A. W., Engel, P., Schröder, T., Benson, O., Reichel, J. & Becher, C. Narrow-band single photon emission at room temperature based on a single nitrogen-vacancy center coupled to an all-fiber-cavity. *Appl. Phys. Lett.* **105,** 073113 (2014).

179. Steiner, M., Meyer, H. M., Deutsch, C., Reichel, J. & Köhl, M. Single Ion Coupled to an Optical Fiber Cavity. *Phys. Rev. Lett.* **110,** 043003 (2013).

180. Kashkanova, A. D., Shkarin, A. B., Brown, C. D., Flowers-Jacobs, N. E., Childress, L., Hoch, S. W., Hohmann, L., Ott, K., Reichel, J. & Harris, J. G. E. Optomechanics in superfluid helium coupled to a fiber-based cavity. *Journal of Optics* **19,** 034001 (2017).

181. Potts, C. A., Melnyk, A., Ramp, H., Bitarafan, M. H., Vick, D., LeBlanc, L. J., Davis, J. P. & DeCorby, R. G. Tunable open-access microcavities for on-chip cavity quantum electrodynamics. *Appl. Phys. Lett.* **108,** 041103 (2016).

182. Biedermann, G. W., Benito, F. M., Fortier, K. M., Stick, D. L., Loyd, T. K., Schwindt, P. D. D., Nakakura, C. Y., Jarecki, R. L. & Blain, M. G. Ultrasmooth microfabricated mirrors for quantum information. *Appl. Phys. Lett.* **97,** 181110 (2010).

183. Derntl, C., Schneider, M., Schalko, J., Bittner, A., Schmiedmayer, J., Schmid, U. & Trupke, M. Arrays of open, independently tunable microcavities. *Optics Express* **22,** 22111 (2014).

184. Wachter, G. *et al.* High-Q silicon microcavities with open access and lithographic alignment. *In preparation* (2018).

185. Wieser, F.-F. *Towards optical cooling of silicon nanoparticles in a microcavity* Masterthesis (2017).

186. Shore, B. W., Dömötör, P., Sadurní, E., Süssmann, G. & Schleich, W. P. Scattering of a particle with internal structure from a single slit. *New J. Phys.* **17,** 013046 (2015).

187. Stickler, B. A. & Hornberger, K. Molecular rotations in matter-wave interferometry. *Phys. Rev. A* **92,** 023619 (2015).

188. Shi, H. & Bhattacharya, M. Optomechanics based on angular momentum exchange between light and matter. *J. Phys. B* **49,** 1–18 (2016).

189. Bhattacharya, M. & Meystre, P. Using a Laguerre-Gaussian Beam to Trap and Cool the Rotational Motion of a Mirror. *Phys. Rev. Lett.* **99** (2007).

190. Shi, H. & Bhattacharya, M. Coupling a small torsional oscillator to large optical angular momentum. *J. Mod. Opt.* **60,** 382–386 (2013).

191. Bhattacharya, M. Rotational cavity optomechanics. *J. Opt. Soc. Am. B* **32,** B55 (2015).

192. Kane, B. Levitated spinning graphene flakes in an electric quadrupole ion trap. *Phys. Rev. B* **82,** 115441 (2010).

193. Coppock, J. E., Nagornykh, P., Murphy, J. P. & Kane, B. E. *Phase locking of the rotation of a graphene nanoplatelet to an RF electric field in a quadrupole ion trap* in *SPIE Nanoscience+ Engineering* (2016), 99220E–99220E.

194. Rahman, A. T. M. A. & Barker, P. F. Laser refrigeration, alignment and rotation of levitated Yb3+:YLF nanocrystals. *Nature Photonics* **11,** 634–638 (2017).

195. Zhong, C. & Robicheaux, F. Shot-noise-dominant regime for ellipsoidal nanoparticles in a linearly polarized beam. *Phys. Rev. A* **95,** 053421 (2017).

196. Papendell, B., Stickler, B. A. & Hornberger, K. Quantum angular momentum diffusion of rigid bodies. *New Journal of Physics* **19,** 122001 (2017).

197. Ralph, J. F., Jacobs, K. & Coleman, J. Coupling rotational and translational motion via a continuous measurement in an optomechanical sphere. *Phys. Rev. A* **94,** 032108 (2016).

198. Liu, S., Li, T. & Yin, Z.-q. Coupling librational and translational motion of a levitated nanoparticle in an optical cavity. *J. Opt. Soc. Am. B* **34,** C8–C13 (2017).

199. Kim, P. H., Doolin, C., Hauer, B. D., MacDonald, A. J. R., Freeman, M. R., Barclay, P. E. & Davis, J. P. Nanoscale torsional optomechanics. *Appl. Phys. Lett.* **102,** 053102 (2013).

200. Kim, P. H., Hauer, B. D., Doolin, C., Souris, F. & Davis, J. P. Approaching the standard quantum limit of mechanical torque sensing. *Nat. Commun.* **7,** 13165 (2016).

201. *Noise protected, tunable, levitated pressure & force sensor* EU patent application 17157211.8-1557.

202. Stickler, B. A., Papendell, B. & Hornberger, K. Spatio-orientational decoherence of nanoparticles. *Phys. Rev. A* **94,** 033828 (2016).

203. Schrinski, B., Stickler, B. A. & Hornberger, K. Collapse-induced orientational localization of rigid rotors. *J. Opt. Soc. Am. B* **34,** C1–C7 (2017).

204. Mair, A., Vaziri, A., Weihs, G. & Zeilinger, A. Entanglement of the Orbital Angular Momentum States of Photons. *Nature* **412,** 313–316 (2001).

205. Ma, Y., Hoang, T. M., Gong, M., Li, T. & Yin, Z.-q. Proposal for quantum many-body simulation and torsional matter-wave interferometry with a levitated nanodiamond. *Phys. Rev. A* **96,** 023827 (2017).

206. Palik, E. D. *Handbook of Optical Constants of Solids* (Academic Press, Boston, 1998).

Acknowledgements

First and foremost I want to thank my family for their endless love and support, for always being there for me, and for making it possible to follow my interests.
I want to thank my supervisor, Markus Arndt, for guiding me through my entire scientific life - from my first steps in building a simple graphite oven for my Bachelor's thesis to finalizing this dissertation. His open door, never-ending curiosity and continued trust have always been incredibly supportive. Now, I truly know the meaning and the nature of the word "Doktorvater".
My gratitude also goes to two of my high school teachers, Wolfgang Wiesenöcker and Manfred Kerschbaumer, for sparking my interest in science.
A big thanks to all past and present members of Team Cavity, sometimes also referred to as Team Awesome. Especially I want to highlight Peter Asenbaum and James Millen. Thank you, Peter for convincing me to join the Quantum Nanophysics group and handing me over the toolset for working with cavities, vacuum systems, electronics and much more. James, I am grateful that you have joined the team and have brought along your expertise in optical tweezers, your British charm and your continuous support. I enjoyed my time in the lab a lot with both of you!
I want to thank all my collaborators: Stefan Nimmrichter, Benjamin Stickler and Klaus Hornberger for all their tremendous theory work; Alon Kosloff, Ori Cheshnovsky and Fernando Patolsky for fabricating all those tiny particles for us; Stephan Puchegger and the Nanocenter for searching and imaging them in the SEM; and Georg Wachter and Michael Trupke for building microcavities with us. Also a big thanks to all members of the Quantum Nanophysics group in the past and presence - it was always great fun and very inspiring to work around all of you.
Thank you, James and Benjamin for proofreading my thesis.
Huge thanks to all my friends for keeping me sane, on the football and basketball court, in the band rehearsal room, or by sharing delicious food with me. You were always there, even if I wasn't.
Finally I want to thank the two doctoral programs CoQuS and VDS for connecting me with so many interesting students from the faculty of physics and the quantum family in Vienna. But most importantly for bringing Manon into my life, who has made the last year of my PhD studies very special and who has supported me patiently during the process of writing this dissertation.